Order Number 8926384

Climatic controls on evaporation in Hawaii

Nullet, Dennis McClain, Ph.D.

University of Hawaii, 1989

U·M·I
300 N. Zeeb Rd.
Ann Arbor, MI 48106

CLIMATIC CONTROLS ON EVAPORATION IN HAWAII

A DISSERTATION SUBMITTED TO THE GRADUATE DIVISION OF THE UNIVERSITY OF HAWAII IN PARTIAL FULFILLMENT OF THE REQUIREMENTS FOR THE DEGREE OF

DOCTOR OF PHILOSOPHY

IN GEOGRAPHY

MAY 1989

By

Dennis McClain Nullet

Dissertation Committee:

Thomas W. Giambelluca, Chairman
Thomas A. Schroeder
Forrest R. Pitts
Lyndon L. Wester
Everett A. Wingert

ACKNOWLEDGMENTS

I owe thanks to many people for making this study possible and for helping me to develop the ability and desire to study scientific problems. I would especially like to thank Paul Ekern who showed me that science is a thing to enjoy in itself rather than a means to an end. Thanks to Tom Giambelluca for allowing me to feed carnivorously on his hard earned projects and to Ev Wingert for believing that schools are for students. Thanks to the late John Street, the consummate geographer in my opinion, who learned by going and doing. Thanks to my other committee members: Tom Schroeder, Woody Pitts, and Lyndon Wester. Finally, I express my gratitude to the Hawaiian Islands for existing.

ABSTRACT

The primary aims of this dissertation are to identify and explain variation in potential evaporation at different elevations and different exposures on tropical high islands, to provide reference data for modeling evaporation, and to suggest how an evaporation model appropriate for tropical high islands might be developed.

New evaporation measurements on Haleakala, Maui, existing data from climate stations on Haleakala (Mauinet), pan evaporation data, and rawinsonde data are analyzed to study the effects of radiation, advection, and high elevation on the evaporation rate.

The most important contribution of this study is in quantifying the importance of advection in controlling the evaporation rate on tropical high islands. Sensible heat advection from the surrounding ocean moderates the evaporation rate at coastal sites. This effect ranged, on average, from 0.85 mm/day enhancement in November to 0.71 mm/day suppression in June. Heat advection from land sources increases the evaporation rate by as much as 2.8 mm/day in central Maui. Large-scale subsidence over the Hawaiian Islands region accounts for an additional source of advection

enhancing evaporation above approximately above 1200 m on the mountain. Preliminary results indicate that this effect increases with elevation in conjunction with the night evaporation rate.

Cloud patterns over the mountain slopes and optical air mass determine the solar radiation receipt (the primary source of energy for evaporation) pattern which ranged from 85% to 51% of clear-day radiation in summer and 80% to 63% in winter. Insolation declined with elevation over the study site, except above 1200 meters in winter where it increased with elevation.

Results of the study indicate that climatic-average potential evaporation can be modeled using the Priestley-Taylor equation modified by advection approximations. Temperature and vapor pressure on the mountain can be estimated using rawinsonde data. Net radiation can be mapped from global radiation using a clear-day radiation baseline reduced to the open-ocean global radiation value, 80%, and further reduced based on a cloud index derived using a wind flow model. Ocean advection can be accounted for at the lower elevations by simply adding a monthly modifier based on results presented in the study. Land advection can be related to soil moisture, estimated using a water balance. The

influence of the evaporation enhancement at high elevations would probably have to be determined empirically, and related to season and elevation.

TABLE OF CONTENTS

LIST OF TABLES

LIST OF ILLUSTRATIONS

I. STUDY SCOPE AND BACKGROUND

". . . the most desperate art of the desperate science of meteorology."

G. J. Symons, 1867

Introduction

Today, evaporation remains the most elusive climatic element and the determination of its rate is indeed a "desperate art." The extreme heterogeneity of natural systems at all scales accounts for the difficulty in determining the simple flux of water vapor from the surface. The evaporation rate depends on a complex relation between the ability of the surface to deliver water to the atmospheric boundary layer, and the ability of the atmosphere to transport water away from the surface. The many variables involved in these processes can be roughly lumped into edaphic, biophysical, and atmospheric categories. Various disciplines have each developed methods to estimate evaporation. That is, soil scientists, biophysicists, and climatologists each tend to study the phenomenon

from the foundations of their own fields.

Many applications for estimates of the evaporation rate exists. In water resources research, regional evaporation estimates are used to model the soil water balance in an attempt to define the quantity of recharge filtering past the plant root zone into the aquifer. Typically, evaporation is the largest component of the water balance, and poor estimates can lead to poor decision making when planning groundwater development. Evaporation estimates have many applications in agriculture. For example, they allow planners to estimate irrigation requirements in agricultural development. For rainfed agriculture, evaporation estimates are useful in determining the suitability of specific crops in an area and the expected growing season. Other scientific applications include the use of evaporation demand in ecological studies concerned with water stress. Evaporation estimates have been employed in water balance calculations to classify world climates. In industry, evaporation demand estimates are useful for designing cooling towers and tailings ponds.

Environmental Controls on the Evaporation Rate

Soil properties help determine the rate at which water can move through the soil matrix to plant roots (and ultimately to leaf stomata) and to the soil surface where evaporation into the atmosphere can occur. The flow rate is governed by Darcy's Law, a rate relation that depends primarily on the distribution of soil particle sizes and soil-moisture tension. The water holding capacity of the soil is also important. The presence of organic matter can greatly increase the soil water capacity as can silt, such as in clay soils. Although clay soils may hold a great deal of water, the rate at which it flows through the matrix is limited by the very high matric potential.

Biophysical factors, i.e. the role of plants, are perhaps the most complex in an evaporating system. Plants extract soil water via their roots and deliver it to the atmosphere through leaf stomata. The extreme diversity in plant physiology and morphology combine to provide infinite permutations in a plant's mechanical ability to deliver water to the air. The depth and density of roots, and the suction potential they develop, control the access by plants to soil water.

The physiology of plants determines how water is transmitted through the stems and even when water is required. For example, pineapple open their stomata only at night. The morphology above ground influences atmospheric mixing in the canopy and the distribution of solar radiation.

Atmospheric controls on evaporation would appear to be the most tractable. In general, extreme heterogeneity does not exist on the scale found in soils and vegetation. Rather, smooth gradients, both vertical and horizontal, are the norm. The ability of the atmosphere to remove water from the surface depends on the energy it can provide for the purpose and the rapidity with which water vapor can be transported away from plants, soils, and open water. Atmospheric controls on evaporation are the subject of this dissertation.

Scope of the Study

The actual evaporation rate from land depends on a complex interplay among the soils, vegetation, and atmosphere. The most common practical method for determining actual evaporation is first to estimate the atmospheric demand, sometimes called potential

evaporation (PE), and use this value as a baseline in a water balance procedure that incorporates soil and vegetation properties. This study is concerned only with estimating atmospheric demand and, as such, considers only atmospheric phenomena. Surface characteristics are discussed only with regard to their influence on the overlaying air. Specifically, pan evaporation will be considered the reference for atmospheric demand as many pan evaporation stations are maintained in Hawaii and these data have traditionally been used as a baseline for PE estimates.

The primary aim of the study is to identify and explain variation in evaporation at different elevations and different exposures on tropical high islands. Tropical high islands are considered distinct from tropical mountains on continental land masses because of the powerful influence on the surrounding ocean on island climate. To accomplish the goal stated above, the study attempts to identify and explain differences between observed and modeled evaporation at various elevations and exposures and to identify and explain the distribution of climatic elements that influence the evaporation rate, particularly solar radiation. Secondary goals of the study are to determine the

applicability of various models for use on tropical high islands, to suggest appropriate modifications of existing models, and to provide reference data for future modeling attempts. The study depends primarily on data collected on the northwest flank of Haleakala, Maui.

Organization of the Study

The study begins with background information (review of literature, evaporation theory and models, and a description of the study site and instrumentation) and a presentation of data collected during field work on Haleakala. These data are then compared with evaporation estimates by several models. Concordance and discrepancies in the comparison are interpreted by reference to the underlying physical processes. Finally, methods of modeling the salient climatic variables and processes that control island evaporation will be suggested based on the study findings. The flow of the study is best described in the following chapter by chapter introduction.

Chapter II discusses the basic background physics and models relevant to the study. Next, Chapter III introduces the study site (Haleakala, Maui), its

climate, and the data and instrumentation to be used. Chapter IV then presents the results of field work at the study site in the winter of 1987-1988 and summer of 1988. Measured and modeled evaporation are compared. The results lead to a discussion of the climatic processes involved in evaporation control on the mountain, radiative energy, advected energy, and special considerations at high elevations, in Chapters V through VII. In Chapter VIII, the results of these investigations are used to suggest methods of modeling evaporation and its climatic controls. The study is then summarized and conclusions drawn in Chapter IX.

Evaporation in Mountainous Terrain

Relatively few mesoscale evaporation studies in mountainous terrain have been reported. Several researchers found a decrease in pan evaporation with elevation above 4000' in the Western United States (Blaney, 1958; Longacre and Blaney, 1962; Horton, 1934). In each of these studies, the evaporation rate remained fairly constant above 8000'. Blaney (1958) suggested that temperature, rather than elevation, had the greatest effect on the evaporation rate. He attributed the slight increase in evaporation at the top of Mt.

Whitney (14502') to high wind speeds. At different locations, studies have shown both increases and decreases in evaporation with elevation below 4000 feet (Horton, 1934; Longacre and Blaney, 1962; Blaney, 1958). Horton (1934) showed that the change in the evaporation rate with elevation depended on different combinations of wind, temperature, and humidity, and that an increase or decrease was possible. He also discounted the effect of decreasing atmospheric pressure as a mechanism to explain the change in evaporation rate.

In Utah, Peck and Pfankuch (1963) found a relation between pan evaporation and combined wind speed and elevation. Increased evaporation on south slopes was associated with southerly winds aloft. The authors note that southerly winds aloft are often associated with a more unstable air mass. Golding (1978) found that adiabatically heated downslope winds (chinook winds) increased evaporation in Alberta. In one of the few high elevation transpiration studies, LeDrew (1975) measured 1.9 mm/day transpiration from tundra at 3500 meters including night transpiration attributed to positive heat advection, the horizontal transport of sensible heat. Studies at high elevations involving evaporation and sublimation from snow are reviewed by Barry (1981).

For tropical mountains, Scarf (1976), in peninsular Malaysia, estimated evaporation by deriving a relationship with elevation. Different relations were derived for the dry central highlands and the more humid northeastern mountains. In Kenya (Brown and Cocheme, 1973) and Papua New Guinea (Keig et al., 1979) pan evaporation was poorly correlated with elevation, though there was a tendency for evaporation to decrease with elevation. Chang (1985) compiled data from 21 tropical highland stations around the world. He found that vapor pressure deficit explained 65% of the variance in measured evaporation. Chang suggested that aerodynamic effects (i.e. the vapor pressure gradient near the surface) were more important than energy considerations in determining evaporation in tropical highlands.

In a simulation of transpiration from north and south facing irrigated slopes in Israel, Segal et al. (1985) combined simplified numerical models of the atmosphere, soil moisture, and vegetation. Ultimately, their model determined transpiration as a function of "stomatal conductance" and "environmental factors" which affected the stomatal aperture. It is unclear how the magnitude of the effect of these factors was determined.

Their results indicated that transpiration followed insolation closely with maxima on southern exposures (for Northern hemisphere sites) whose slope approximated Israel's latitude.

Many ecological studies have documented that, in mid-latitudes, xerophytic vegetation and short grasses are often found on equator-facing slopes while pole-facing slopes are covered with trees and taller grasses (Armesto and Martinez, 1978; Cottle, 1932). The dry pole-facing slope vegetation has generally been attributed to lower soil moisture resulting from higher evaporation induced by higher insolation receipt (Bennett et al., 1976). Accordingly, insolation variations resulting from slope and aspect have been utilized to map evaporation on slopes (Rouse, 1970; Rouse and Wilson, 1969; Schulze, 1975)

Some applications, such as estimating the water balance for an entire watershed, require a regional scale estimate of evaporation. To extrapolate point measurements of evaporation to large areas of complex topography is an uncertain technique at best and introduces a great deal of uncertainty into the regional evaporation estimate. In an attempt to overcome this limitation of ground based measurements, Kustas and

Brutsaert (1987) have attempted to estimate regional scale evaporation by studying the flux of water vapor though the mixed and inversion layers of the lower troposphere using rawinsonde profiles. They found the mean mixed layer specific humidity gradient to be well correlated with the flux of water vapor through the inversion layer. Although the inversion water vapor flux was poorly correlated with ground based evaporation measurements, the authors suggest that better resolution in the atmospheric profiles may yield reasonable surface flux estimates and thus eliminate the need for most surface evaporation measurements.

Evaporation Studies in Hawaii

Evaporation research and data collection in Hawaii has concentrated on applications in local agriculture and on hydrological questions concerning recharge to basal fresh water lens systems. A summary of the major findings relevant to the current study is given below. Further discussion can be found in Ekern and Chang (1985), Giambelluca (1983), and Jones (1980).

In a two year study of evaporation in the lee of Oahu's Koolau mountains, Ekern (1983) found that Priestley and Taylor's (1972) method provided good

estimates of evaporation for a wet ridge, but underestimated evaporation in a valley (see Figure 1). On the wet ridge, sunlight provided the major energy source for evaporation. The exception was the lowest site, Mililani, where heating by advection was indicated. Here, pan evaporation increased from 67% of the energy in measured insolation in winter to 75% in summer.

Measured evaporation at four sites in Manoa valley exceeded Priestley-Taylor estimates by up to 40%. In addition, evaporation at Huelani station in the valley exceeded that on an adjacent exposed ridge site by 11%. Measurements indicated that the high evaporation rates were due in part to longwave radiation trapped by the valley walls. Adiabatic warming due to subsidence from the crest and positive heat advection from nearby urban areas were also suggested.

Intercorrelation between Huelani and Mauka evaporation in Manoa valley was 0.96 for 1981 monthly totals and 0.73 in January and 0.39 in July for daily totals. However, the correlation between Huelani and Kipapa Ridge Site No. 6 (within the cloud deck) was only 0.02.

Maps of pan evaporation by Ekern and Chang (1985),

compiled primarily from pan evaporation measurements in lowland agricultural areas, clearly illustrate the effect of topography on evaporation. Evaporation ranged from 20 mm/day under the windward orographic cloud to over 100 mm/day at dry lee sites. In general, evaporation decreased with elevation. This decline was attributed to a decrease in temperature, and increases in humidity and cloudiness. Evaporimeter transects on Hawaii indicated that above the inversion, however, evaporation increases again to sea level values. Extremely low humidity was suggested as a reason for this increase. Compared to other climatic elements, pan evaporation showed a generally low coefficient of variation, averaging 30% for daily values, 15% for monthly values, and 7% for annual values.

Ekern (1983) and Ekern and Chang (1985) suggested physical mechanisms controlling evaporation in the Hawaiian Islands: channelled wind flow and high insolation increased evaporation in the central Maui isthmus; mixing on the promontories of Oahu kept pan evaporation near open ocean values despite lower insolation in these areas; positive heat advection increased evaporation in dry lee areas; mixing of air near 5000 feet increased evaporation on Kauai, Maui, and

Hawaii; local circulations, land-sea breeze and drainage winds, on Hawaii increased cloudiness and decreased evaporation.

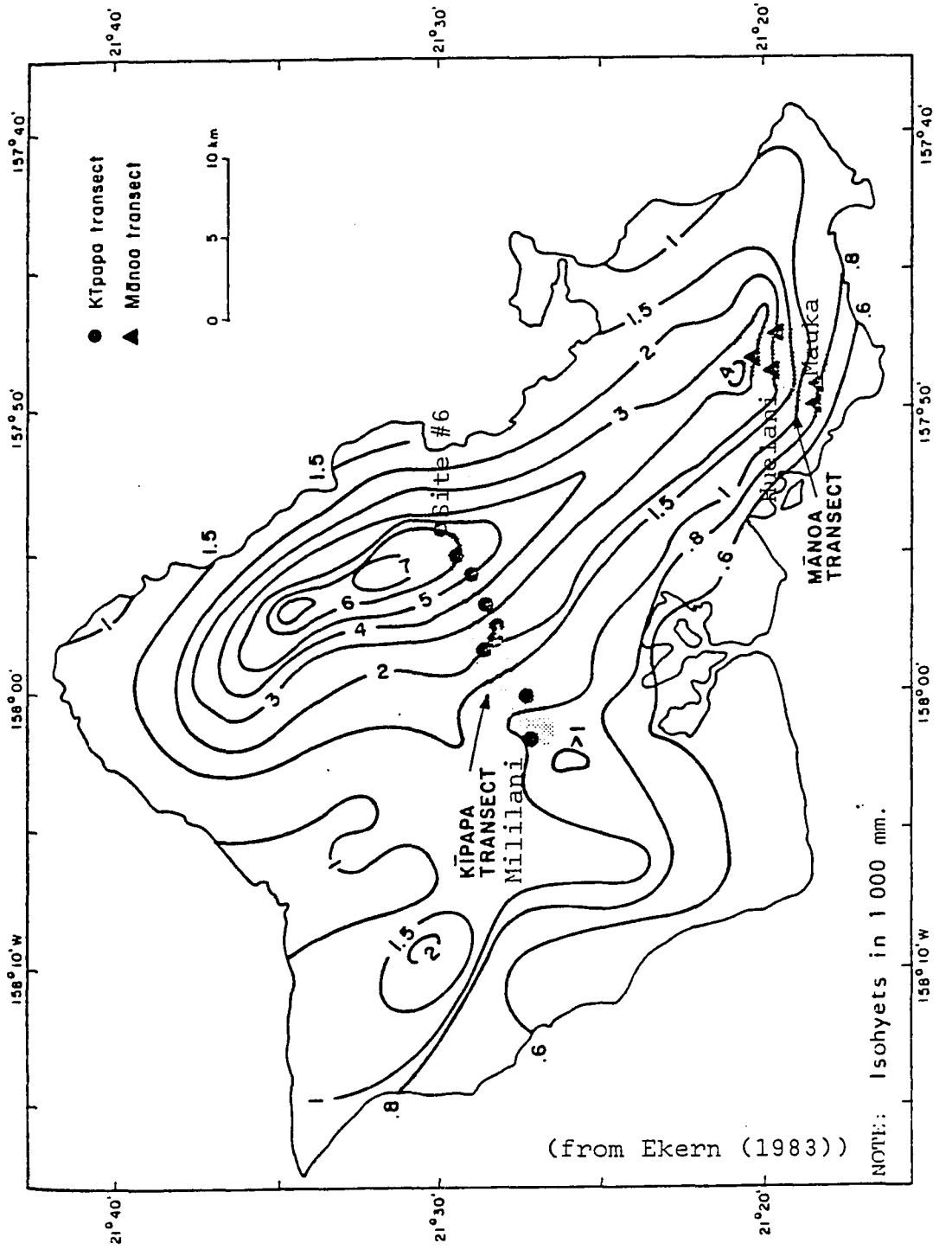

Figure 1. Ekern (1983) evaporation study sites

II. PHYSICAL BASIS AND MODELS

This chapter presents a review of the physics and models relevant to the study of evaporation. Current understanding of the physical processes involved in evaporation can be illustrated by examining current approaches to modeling the evaporation phenomenon. These modeling approaches will be discussed in some depth in this chapter. Then, a short review of solar radiation and advection, the two principal sources of energy for evaporation, is given.

Basic Physics of Evaporation

In water, molecular velocities follow a distribution first proposed for gases by Clerk Maxwell in the nineteenth century. Temperature is a measure of the average velocity, and hence kinetic energy, of the water molecules. In the case of an open water surface, the fastest moving molecules are able to escape through the water surface, their momentum overcoming intermolecular attraction at the surface, the surface tension. The departure of molecules with high kinetic energy lowers the average kinetic energy of the water body and thus

lowers the water temperature. The magnitude of this kinetic energy transfer is called the latent heat of vaporization, λ, which is a property of the liquid. While molecules escape from the liquid, others return from the overlaying air. When the net flux of water molecules is away from the surface, the process is called evaporation. When the net flux is toward the surface, it is called condensation. The partial pressure of the air due to the presence of water molecules is called the vapor pressure of the air. The maximum vapor pressure in air that is possible is called the saturation vapor pressure (ignoring for the moment supersaturation) and depends on the ambient temperature.

Before going further, it will be useful to describe the theoretical limits on the evaporation rate. First, consider evaporation as an effusion process. That is, assume that no gradient exists and that evaporation is simply the molecular flux from the water surface. In this case, diffusion is not relevant, and the evaporation rate depends solely on the mean molecular velocity and vapor density. Evaporation is calculated from the kinetic theory of gases by determining the collision frequency of water vapor molecules with a water surface and knowing that at saturation the number

of water molecules leaving the surface equals the number of vapor molecules being absorbed by the surface from the air. Alty (1935) appears to have been the first to study this problem for the case of water evaporation. For water evaporating into a near vacuum, he wrote,

$$E = 43.75(10^{-6})(e_{s*} - e_a)f(M/T_s)^{0.5} \qquad (2.1)$$

where E is evaporation in g cm^{-2} s^{-1} (s is seconds), where M is the molecular weight (18), e_{s*} is the liquid vapor pressure and e_a is the actual vapor pressure of the air (dynes cm^{-2}), f is the fraction of molecules absorbed on collision with the water surface, and T_s is the temperature of the evaporating surface. At 20°C (293°K), f is about 0.032 (Alty, 1935; Delaney et al., 1964), so the maximum evaporation rate possible, assuming $e_a = 0$, is

$$E = 43.75(10^{-6})(23373 - 0)*0.032*(18/293)^{.5}$$
$$= 0.00811 \text{ g cm}^{-2} \text{ s}^{-1}$$
$$= 0.0811 \text{ mm s}^{-1}$$
$$= 7000 \text{ mm day}^{-1}$$

This value is equivalent to the rate at which molecules leave a water surface at 20°C. That it is not observed in nature reflects only the high return rate of water molecules from the atmosphere. Considering that observed evaporation rates are three orders of magnitude

less than this, the dramatic inhibiting effect of gradients on mass transfer in nature becomes apparent.

As a check on this calculation, the equation can also be written (Collie, 1982):

$$E = nc/4 = fA_v e_{s*}(2p_i MRT)^{0.5} \qquad (2.2)$$

where n is the number of molecules per unit volume, c is the mean velocity of the molecules, A_v is Avagadro's number ($6.022(10^{23})$), p_i is 3.1415926, M is the molecular weight, R is the universal gas constant, and f if the fraction of water molecules colliding with the surface that are absorbed (Collie, 1982).

So, for water at 20°C (e_{s*} = 23.373 mb = 23373 dynes cm^{-2}) and f = 0.32, the rate molecules leave the surface is:

$E=.032*6.022(10^{23})*23373*(2*3.1416*18*8.314(10^{7})*293)^{-.5}$

$= 2.714(10^{20})$ molecules cm^{-2} s^{-1}

$= 0.00811$ gm cm^{-2} s^{-1}

$= 0.0811$ mm s^{-1}

$= 7000$ mm day^{-1}

Now, consider the case in which water evaporates into a near vacuum where air pressure is reduced almost to the saturation vapor pressure, just above the point at which water would begin to boil. Here the evaporation rate depends on molecular diffusion

(Brutsaert, 1982),

$$E = \kappa_e \rho (q_s - q_z)/z \qquad (2.3)$$

where q_s is the saturation specific humidity, q_z is the actual specific humidity, z is the height at which q_z is measured, ρ is the air density, and κ_e is the molecular diffusivity of water vapor. At 20°C, 25 mb, and zero humidity at 5 cm, E would be approximately:

$$E = (0.257 \text{ cm}^2 \text{ s}^{-1})(0.0000297 \text{ g cm}^{-3})(0.5-0)/5 \text{ cm}$$
$$= 7.6(10^{-7}) \text{ g cm}^{-2} \text{ s}^{-1}$$
$$= 7.6(10^{-6}) \text{ mm s}^{-1}$$
$$= 0.66 \text{ mm day}^{-1}$$

Now let us raise the air pressure and consider a typical windless day near sea level, 1000 mb, with ρ = 0.0011884 g cm^{-3}, T = 20°C, κ_e = 0.257 cm^2 s^{-1}, q_s = 0.01454, and q_z = 0.01000 at z = 5 cm, the evaporation rate would be:

$$E = (0.257)(0.0011884)(.01454-.01)/5$$
$$= 2.8(10^{-7}) \text{ g cm}^{-2} \text{ s}^{-1}$$
$$= 2.8(10^{-6}) \text{ mm s}^{-1}$$
$$= 0.24 \text{ mm day}^{-1}$$

As can be seen by the above result, molecular diffusion under normal environmental conditions is a slow process, being impeded by collisions with air molecules. As the density of the air decreases,

collisions are less frequent, the mean free path of the molecules increases, and consequently the diffusion rate increases linearly. Limited only by molecular diffusion, evaporation thus increases linearly with decreasing atmospheric pressure.

The point of these calculations is to illustrate the evaporation extremes possible. Somewhere between these extremes, effusion and molecular diffusion, lie the evaporation conditions found in nature. Typically in Hawaii, for example, daily evaporation rates range from 1 to 10 mm per day. Instantaneous rates (based on data presented in Chapter VII) have been measured as at least $1.7(10^{-4})$ mm s^{-1}. While molecular diffusion depends solely on the vapor pressure gradient, in natural environments turbulent diffusion generally dominates the vapor transport. In 1802, Dalton suggested that evaporation was simply a function of the vapor pressure deficit and wind speed. His suggestion can be written as,

$$E = f(u)(e_s - e_a) \qquad (2.4)$$

where f(u) is some function of the air flow which accounts for turbulence.

Though over 100 years have passed since Dalton offered this simple formula, a satisfactorily general

formulation of f(u) has yet to be discovered. Instead, various methods have been used to attempt to model and understand evaporation in the environment, ranging from energy and mass balances to measuring the water vapor flux through the lower atmosphere directly. What follows is a summary of the most important of these approaches along with the relevant equations.

Almost all of the methods presented in the following section deal with potential evaporation, broadly defined as evaporation from a continuously wetted surface, which, as stated in Chapter I, is ultimately referenced to pan evaporation. Only the mass budget method, eddy correlation, and methods that incorporate a surface resistance to diffusion term deal with actual evaporation. For these limited cases, the transpiration through plant stomata is included in the term evaporation.

Energy Balance and the Penman Equation

Energy balance methods estimate evaporation indirectly by estimating it as a residual term in an accounting of sources and sinks for energy. The energy balance methods are the most widely used practical

method of estimating evaporation and the equations presented here will be used later in this study as well.

Bowen ratio

Energy budget methods account for the total flux of energy toward and away from the surface. The energy budget can be written as:

$$Q^* + A = \lambda E + H + G + S + P_s \qquad (2.5)$$

where Q^* is net radiation, A is advection, λ is the latent heat of evaporation, E is evaporation, H is heat flux to the air, G is heat flux to the ground, S is storage, and P_s is energy used in photosynthesis. Photosynthesis typically accounts for only about 1% of the energy balance (Brutsaert, 1982). For a complete day, net G and S are usually considered to be negligible, although the cumulative effect of these terms may be evident in an annual cycle. Over moist homogeneous surfaces A would also be negligible. This leaves the simple relation:

$$Q^* = \lambda E + H \qquad (2.6)$$

That is, net radiation, being the net absorbed solar radiation minus net longwave radiation, is partitioned between latent and sensible heat flux to the atmosphere. In 1926, Bowen showed that if sensible and latent heat

absorb all the energy added to the system then,

$$H/E = (K_h/K_e)(T_s-T_a)/(e_s-e_a) \quad (2.7)$$

where K_h and K_e are the transfer coefficients for heat and water vapor respectively, is the psychrometric constant, T_s is surface temperature, T_a is air temperature, e_s is surface vapor pressure, and e_a is the vapor pressure of the air. This equation, combined with (2.6), provides a fairly simple method of estimating evaporation. If the transfer coefficients are assumed equal, then the problem reduces to surface and standard height temperature and humidity measurements along with net radiation. The method requires instantaneous readings. The principal difficulty lies in determining surface temperature and vapor pressure.

The Penman equation

H.L. Penman (1948) proposed a method of computing evaporation potential from routine surface meteorological observations. The result has become known as the combination approach as Penman combined "sink strength" and "energy balance" into a single formula. He began with (2.4), the Dalton equation, in terms of potential evaporation,

$$\lambda E = f(u)*(e_s - e_a) \quad (2.8)$$

Now substituting (2.8) into (2.7) and assuming that $K_h=K_e$ (valid for neutral conditions),

$$H = \gamma f(u)*(T_s - T_a) \qquad (2.9)$$

Here Penman introduced Δ, the slope of the temperature versus saturation vapor pressure curve, which is symbolically written as de_*/dT_a and can be approximated by,

$$\Delta = (e_{s*}-e_{a*})/(T_s-T_a). \qquad (2.10)$$

where the * subscript denotes saturation values. Inserting (2.10) into (2.9) yields,

$$H = (\gamma/\Delta)f(u)*(e_{s*} - e_{a*}) \qquad (2.11)$$

This can be rewritten algebraically as:

$$H=(\gamma/\Delta)f(u)*(e_{s*}-e_a) - (\gamma/\Delta)f(u)*(e_{a*}-e_a) \qquad (2.12)$$

By assuming that the surface is at saturation vapor pressure and substituting (2.8) into (2.12),

$$H = (\gamma/\Delta)\lambda E_p - (\gamma/\Delta)f(u)*(e_{a*} - e_a) \qquad (2.13)$$

Substituting (2.6) into (2.13),

$$Q^* = \lambda E_p+(\gamma/\Delta)*\lambda E_p-(\gamma/\Delta)f(u)*(e_{a*}-e_a) \qquad (2.14)$$

Simplifying,

$$(\gamma/\Delta)Q^* = \lambda E_p(1+(\gamma/\Delta))-f(u)*(e_{a*}-e_a) \qquad (2.15)$$

or, rearranging,

$$\lambda E_p = ((\gamma/\Delta)Q^*+f(u)*(e_{a*}-e_a))/(1+(\gamma/\Delta)) \qquad (2.16)$$

and rearranging again,

$$\lambda E_p = (\Delta Q^* + \gamma f(u)*(e_{a*} - e_a))/(\Delta+\gamma) \qquad (2.17)$$

which is Penman's original equation.

The formulation neatly does away with the need for surface observations, requiring only standard height meteorological measurements of radiation, temperature, humidity, and wind. For this reason and because of its great success in duplicating measured evaporation, Penman's equation has become the mainstay for practical evaporation estimation.

Penman originally calibrated his equation using measurements from cast iron evaporation pans 0.76 m in diameter. He found that under similar weather conditions, evaporation from bare wet soil was 90% that of open water, and evaporation from well watered turf ranged from 60% to 80% that of the open water value depending on the season. His tests were conducted in Rothamstead, England.

The Penman method has many shortcomings. Theoretically, Δ should be taken at the average of T_s and T_a, rather than just at T_a; it assumes no horizontal divergence in H and λE; the diffusivity coefficients for heat and water vapor are assumed equal; and it ignores other energy sinks and advection. Shortcomings in application include: calculations should be instantaneous, though averages provide reasonable

estimates; the original terms contained much empiricism; climatic data are usually taken under non-potential (water availability not limited) conditions; and no consideration of plant and soil characteristics is given (Van Bavel, 1966).

Modifications of Penman's formula

Penman presented a sound theoretical method of estimating the evaporation rate based on thermodynamic and aerodynamic principles. In the extreme case, where water is evaporating into a saturated atmosphere (this is a diabatic system where slight temperature increases accompany slight vapor pressure increases), Slatyer and McIlroy (1967) showed that the Penman formula reduces to:

$$\lambda E = \Delta Q^{*}/(\Delta+\gamma) \qquad (2.18)$$

This they called equilibrium evaporation and the quantity represents the theoretical minimum evaporation from a wet surface. Priestley and Taylor (1972) found that by introducing an empirical constant, , the formula provided excellent agreement with measured evaporation rates. Thus (2.18) becomes,

$$\lambda E = \alpha \Delta Q^{*}/(\Delta+\gamma) \qquad (2.19)$$

The average constant recommended by Priestley and

Taylor for a moist surface in the absence of advection was 1.26 and subsequent research has shown a remarkable consistency in this parameter, usually determined to lie between 1.20 and 1.30 (Monteith, 1985). A satisfactory theoretical explanation for this consistency has not been advanced, but Monteith (1981) suggested that the additional energy source implied in the constant might be entrainment of dry air through an inversion layer. De Bruin (1983a) pointed out that in the wet humid tropics, the temperature seldom rises above 32^{o}C and that, perhaps by no coincidence, the Priestley-Taylor equation predicts all Q^{*} will be absorbed as latent heat at just that temperature. He also proposed a model for the α parameter based on surface resistance, r_s (discussed below) (de Bruin, 1983b).

The idea of reformulating Penman's original aerodynamic term in as a function of resistance to diffusion was first proposed by Penman and Schofield (1951) and later formalized by Monteith (1965). Monteith envisioned Penman's equation as dependent on diabatic and adiabatic processes. The so-called energy term in the equation represents a diabatic processes, that is, energy from outside the system is partitioned into sensible and latent heat according to known

thermodynamic principles. The aerodynamic term, on the other hand, represents an adiabatic process, being merely a redistribution of the energy already present. This includes evaporation from the surface at the expense of sensible heat from the air.

In an adiabatic exchange, the increase in latent heat would equal the decrease in sensible heat of the air. In unsaturated air cooling to the wet bulb temperature (T_{wb}), the latent heat and sensible heat exchange are related by:

$$\lambda E = \rho c_p (T_a - T_{wb}) \qquad (2.20)$$

In other words, the heat density of the air times the change in temperature equals the increase in latent heat.

This can be written in terms of the vapor pressure deficit of the air ($e_{a*} - e_a$) by following a thermodynamic path to the wet bulb point (dependent on γ) and then along the saturation vapor pressure curve (using an approximate slope, Δ, evaluated at the mean of T_a and T_{wb}). Equation 2.20 then becomes,

$$\lambda E = \rho c_p (e_{a*} - e_a)/(\Delta + \gamma) \qquad (2.21)$$

Now, the conversion of sensible to latent heat depends on the <u>rate</u> of exchange. Here a resistance term, r_a, was introduced, defined as the time required

for a unit volume of air to exchange energy with a unit surface area. By analogy to Ohm's electrical resistance: r_a is the resistance, heat exchange is the current, and the vapor pressure deficit is the voltage. Rewriting (2.21) as a rate equation, then, gives:

$$d(\lambda E)/dt = \rho c_p((e_{a*} - e_a)/r_a)/(\Delta + \gamma) \quad (2.22)$$

The constant, r_a, is often called the aerodynamic resistance. Basically, r_a replaces f(u) in (2.4) and depends mainly on turbulence, i.e. wind velocity, ground heating, and surface roughness. The results of this equation generally yield λE in units of g cm^{-2} s^{-1}. By combining the diabatic (Penman's energy term (2.18)) and adiabatic term (2.22), Monteith rewrote Penman's equation as:

$$d(\lambda E)/dt = (\Delta(Q^*+A)+\rho c_p((e_{a*}-e_a)/r_a))/(\Delta+\gamma) \quad (2.23)$$

Monteith expressed the the external energy supplied to the system in general terms and I have expressed this as net radiation plus advection. In this equation λE, the external energy supply, and internal energy exchange are expressed as rates.

All equations to this point describe evaporation from a saturated surface. For non-saturated surfaces, Monteith included a stomatal or canopy resistance term, r_s. The term can be included in (2.23) by noting that

the actual vapor pressure deficit at the surface is related to a saturation vapor pressure deficit at the surface by:

$$(e_s - e_a) = (e_{s*} - e_a) r_a/(r_s + r_a) \qquad (2.24)$$

In the original Penman equation a key assumption was that the surface was at saturation vapor pressure. However, (2.24) can be incorporated into the Bowen Ratio (2.6) as,

$$H/\lambda E = \gamma(1 + r_a/r_s)(T_s - T_a)/(e_{s*} - e_a) \qquad (2.25)$$

The term $\gamma(1 + r_a/r_s)$ thus appears as a modified psychrometric constant and can be incorporated into (2.23) by,

$$\lambda E=(\Delta(Q^*+A)+\rho c_p((e_{a*}-e_a)/r_a))/(\Delta+\gamma(1+r_a/r_s)) \qquad (2.26)$$

Vapor Flux Through the Atmospheric Boundary Layer

In this section, many of the approaches to modeling turbulent processes in atmospheric boundary layer (ABL) are reviewed. Brutsaert (1982) defines the ABL as "the lower part of the atmosphere where the nature and properties of the surface affect the turbulence directly." In general, use of these methods is restricted to diagnostic studies of evaporation, rather than practical prediction of the phenomena, because of the high input data or expensive instrumentation

requirements. The discussion provides some insight into the physical processes involved in the turbulent transport process.

Eddy correlation

Wind flow near the surface is turbulent in nature, eddies being responsible for the vertical transport of momentum, water vapor, and any other admixture. As the horizontal wind carries eddies past a fixed point the vertical wind at the point will alternately be directed upward and downward. Measurements of the difference in vapor pressure in the upward and downward motions reveal the vapor flux away from the surface. The evaporation rate is the average of these fluxes, or:

$$E = \rho \overline{w'q'} \qquad (2.27)$$

where the bar indicates averages values, the prime denotes instantaneous deviations from the mean value of the vertical wind speed, w, and specific humidity, q. Evaporation can be estimated with continuous measurements of these quantities by the eddy-correlation technique. Widespread adoption of the method as a practical tool awaits reliable and affordable fast-response instrumentation.

Mean profiles

Besides instantaneous eddy flux measurements, water vapor transport through the surface sub-layer can be inferred by measuring mean profiles of wind, humidity, and/or temperature. Profile equations for momentum, water vapor, and sensible heat flux follow from dimensional analysis. That is, the gradient is proportional to the quantity leaving or being absorbed by the surface. For momentum, the shear stress, or momentum flux, τ, is proportional to the wind gradient,

$$\tau = \rho K_m (du/dz) \tag{2.28}$$

Similarly, for water vapor and sensible heat,

$$E = -\rho K_e (dq/dz) \tag{2.29}$$

$$H = -\rho c_p K_h (dT/dz) \tag{2.30}$$

The transfer coefficients (analagous to the coefficient of molecular diffusivity, but applying under turbulent conditions, and sometimes called the eddy diffusivity) are proportional to the turbulent properties of the atmosphere,

$$K_m = k u_* z / \varnothing_m \tag{2.31}$$

$$K_e = k u_* z / \varnothing_e \tag{2.32}$$

$$K_h = k u_* z / \varnothing_h \tag{2.33}$$

where u_* is called the friction velocity defined as,

$$u_* = (\tau/\rho)^{1/2} \qquad (2.34)$$

The friction velocity is presumed to be independent of height and represents the velocity whose square is exactly proportional to the shear stress, a property confirmed by observation (Sutton, 1955).

The constant of proportionality for momentum, k, or Von Karmen's constant, is non-dimensional and usually taken as 0.4. The $\varnothing$ terms are empirical stability correction factors, i.e. the relative contributions of mechanical and convective turbulence. Combining (2.28) through (2.34) and integrating, yields:

$$u_2 - u_1 = (u_*/k)\ln((z_2-d)/(z_1-z_o)) - \Phi_m) \qquad (2.35)$$

$$q_1 - q_2 = (E/ku_*\rho)\ln((z_2-d)/(z_1-z_o)) - \Phi_e) \qquad (2.36)$$

$$T_1 - T_2 = (H/ku_*c_p\rho)\ln((z_2-d)/(z_1-z_o)) - \Phi_h) \qquad (2.37)$$

where Φ is the integrated form of $\varnothing$. Here the constant, z_o, the velocity axis intercept of the velocity versus the log of height curve sometimes called the roughness length, has been added to account for deviations from the logarithmic relationship between wind speed and height near the surface. For grass, this value lies between 0.01 and 0.05 meters (Panofsky and Dutton, 1984). The value of d_o, sometimes called the zero plane displacement height, is approximately equal to 2/3 the average height of the roughness obstacles,

$$d_o = 2h_o/3 \qquad (2.38)$$

For surface values and measurements at one height only, (2.35) to (2.37) become,

$$u = (u_*/k)\ln((z-d_o)/z_o) - \Phi_m) \qquad (2.39)$$

$$q_s - q = (E/ku_*\rho)\ln((z-d_o)/z_o) - \Phi_e) \qquad (2.40)$$

$$T_s - T = (H/ku_*c_p\rho)\ln((z-d_o)/z_o) - \Phi_h) \qquad (2.41)$$

In the absence of wind profile data, z_o can also be approximated as,

$$z_o = h_o/7.5 \qquad (2.42)$$

(Chamberlain, 1968; Perry and Joubert, 1963; Plate, 1971).

Several methods have been developed to parameterize Φ_m, Φ_h, and Φ_e under stable, unstable, and neutral conditions (Monin and Obukhov, 1954; Paulson, 1970; Panofsky and Dutton, 1984).

Now, u_* is common to (2.35)-(2.37) and (2.39)-(2.41) and can be found from (2.35) with wind measurements at two levels, being,

$$u_* = k(u_2-u_1)/(\ln((z_2-d)/(z_1-d_o)) - \Phi_m) \qquad (2.43)$$

Given wind and humidity measurements at two levels, or at one level with additional surface humidity measurements, E can be found from (2.36) or (2.40) and (2.43). Similarly, by employing (2.6) with wind and temperature measurements, E can be found as a residual

term by computing H from (2.37) or (2.41) and (2.43). Since the stability length, L_o, is calculated from H and E, the solution to the equations must be an iterative one. Brutsaert (1982) recommends an averaging time for measurements of 30 to 60 minutes.

The mean profile method has been recommended for regional scale evaporation estimates as it does away with the need to consider the complex pattern of soil and vegetation characteristics (Brutsaert, 1986).

Interfacial sub-layer

A review of the transfer mechanisms in the shallow layer adjacent to the surface in the presence of wind is given by Brutsaert (1982). Three cases are considered; the first involves flow over over smooth surfaces, with the roughness Reynolds numbers below 0.13. The roughness Reynolds number is a measure of the inertial to viscous forces acting on the fluid and is defined as,

$$z_{o+} = u_* z_o / \nu \qquad (2.44)$$

where ν is the kinematic viscosity of air given by,

$$\nu = \mu / \rho \qquad (2.45)$$

where μ is the dynamic viscosity of air. The kinematic viscosity is the analog of K_m for laminar flow.

In one solution to the smooth flow case, Brutsaert (1975) solved the molecular diffusion equation for transport into microscale eddies,

$$E = C_s \kappa_e^{.67} (\rho_{es} - \rho_{eh}) u_* \nu^{-.67} \qquad (2.46)$$

where C_s is an empirical constant (approximately 1/13.6). The water vapor density ρ_{eh}, refers to a height,

$$h = 30 \nu / u_* \qquad (2.47)$$

above the surface. This is approximately the depth of the interfacial sublayer, or the layer between the surface and the fully turbulent region of the atmosphere. Merlivat (1978) found this solution adequate up to a roughness Reynolds number of 1. Flow of this type is rare in the environment because it implies a virtual absence of turbulence.

Brutsaert (1982) next considers what he calls bluff surfaces. These surfaces are covered with impermeable objects such as rocks, waves, or large, stiff leaves and produce Reynolds numbers exceeding 2. By considering water vapor flux in a series of injections into eddies in contact with the surface, Brutsaert (1975) derived,

$$E = C_R \kappa_e^{.5} u_*^{.75} (\rho_{es} - \rho_{eh}) (\nu z_o)^{-.25} \qquad (2.48)$$

where C_R is approximately equal to 1/7.3.

To avoid difficult determinations of values at h,

the transfer equations can be written in generic form that depends only on values in the turbulent layer overlaying the interfacial sub-layer. The bulk transfer equation is,

$$E = Ce_z \rho u_z (q_s - q_z) \tag{2.49}$$

The bulk transfer Dalton number, Ce, can be written as

$$Ce_z = Cd_z^{.5}/(Da_o^{-1} - a_e^{-1}Cd_o^{-.5} + a_e^{-1}Cd_z^{-.5}) \tag{2.50}$$

where Da_o is the interfacial Dalton number and Cd is the drag coefficient, which at z, can be determined by,

$$Cd_z = u_*^2/u_z^2 \tag{2.51}$$

The interfacial layer parameters, Da_o and Cd_o, are difficult to determine but have been studied by diagnostic means with known evaporation rates. These parameters can be eliminated by writing (2.50) as,

$$Ce_z = a_e Cd_z^{.5}/(B^{-1} + Cd_z^{-.5}) \tag{2.52}$$

where

$$B = (a_e(Da_o^{-1} - a_e^{-1}Cd_o^{-.5}))^{-1} \tag{2.53}$$

For smooth surfaces, B has been found to be estimatable from the Schmidt number, which is

$$Sc = \nu / \kappa_e \tag{2.54}$$

Brutsaert (1982) lists several of these formulations in his Table 4.1. Representative is Brutsaert's (1975) equation,

$$(a_e B)^{-1} = 13.6Sc^{2/3} - 13.5 \tag{2.55}$$

For bluff roughness surfaces, less agreement exists. Table 4.2 in Brutsaert gives a number of these expressions. Typical is Brutsaert's (1975) equation,

$$(a_e B)^{-1} = 7.3 z_{o+}^{.25} Sc^{1/2} - 5 \qquad (2.56)$$

For surfaces with permeable obstacles, such as vegetation, the state of knowledge is poor for three principal reasons. First, separation of the effects of porosity induced roughness and porosity itself. Second, the absence of coherence in turbulent response to different types of rough surfaces. Third, difficulty in measuring shear at the porous "wall."

The equations for the interfacial sublayer are not a practical solution for estimating evaporation from the surface. They are more valuable as diagnostic tools when the evaporation rate is known. Thus they provide a tool for sensitivity studies of the effect of changes in the various parameters on the evaporation rate and for studying the bulk roughness properties of the surface.

Mass Budget

Mass budget methods yield evaporation as a residual term. The soil moisture budget can be written as:

$$P = E + R_o + R_c + S_w \qquad (2.57)$$

where P is precipitation, E is evaporation, R_o is

runoff, R_c is recharge and S_w is the change in soil moisture storage.

On an annual basis in river basins, the evaporation can be simply approximated as the precipitation minus the runoff. This assumes that over long periods, changes in groundwater storage are negligible.

The soil water budget will also yield evaporation. This can be accomplished with soil moisture profiles or calculated indirectly by using transpiration-soil moisture relationships. The soil moisture budget can be tracked using a water balance model.

The mass budget is also the fundamental method of lysimeters, evaporation pans, and other atmometers. The measured difference between water entering and leaving the instrument is considered evaporation.

The preceding discussion has presented an overview of the various methods of estimating evaporation and the relevant physical theory. This study is concerned only with potential evaporation, and thus none of the methods that include a surface resistance term or deal with actual evaporation will be used. Primarily, the Penman equation (2.17) and its subsequent versions will be used when comparing measured and modeled evaporation. This is because these equations, and particularly the

Priestley-Taylor equation (2.19) (Ekern, 1983), have been shown to provide reasonable estimates of measured evaporation in Hawaii.

Solar Radiation

The driving variable in the energy balance approaches to modeling evaporation is net radiation, which in turn is highly dependent on incoming solar radiation. Insolation at the earth's surface depends on the extraterrestrial solar radiation at Earth's orbital position, the attenuation of extraterrestrial solar radiation by a cloudless atmosphere, and the further reduction of incoming solar radiation by clouds. These processes are described below along with a summary of the equations used in calculating clear-day insolation for this study.

Extraterrestrial solar radiation

The intensity of extraterrestrial solar radiation depends on the radiant output of the sun, the distance of the Earth from the sun, and the altitude of the sun in the sky. The average value of the intensity of extraterrestrial radiation, often called the solar constant, is about 1370 W m^{-2}. This value fluctuates

regularly throughout the year because of the eccentricity of the Earth's orbit about the sun, being about 3.5% below the average value at apogee (about 4 July) and 3.5% higher at perigee (about 3 January). The position of the sun in the sky and the length of the day throughout the year are summarized in a sky chart. Figure 2 shows a sky chart for Honolulu's latitude.

The quantity of extraterrestrial radiation that would fall on a horizontal surface above Earth's atmosphere (often called Angot's value after the turn-of-the-century French meteorologist Charles Alfred Angot) can be calculated by,

$$dI_o/dt = (J_o/E_o)\cos(\tau) \qquad (2.58)$$

where I_o is the solar radiation intensity on a horizontal surface, J_o is the solar constant (1370 W m^{-2}), E_o is a correction based on the square of the actual to average Earth-Sun distance, and τ is the zenith angle of the sun (List, 1966). The solar zenith angle, τ, can be found from,

$$\cos(\tau) = \sin(\phi)\sin(\delta)+\cos(\phi)\cos(\delta)\cos(h) \qquad (2.59)$$

where ϕ is the latitude, δ is the sun's declination, and h is the sun's hour angle. The solar declination can be estimated by (from Iqbal, 1983),

$$\delta = (0.006918-0.399912\cos(\Gamma)+0.070257\sin(\Gamma)$$

$$-0.006758\cos(2\Gamma)+0.000907\sin(2\Gamma)$$
$$-0.002697\cos(3\Gamma)+0.00148\sin(3\Gamma)(180/\pi) \quad (2.60)$$

where Γ is the day angle given by,

$$\Gamma = 2\pi(\text{day} - 1)/365 \quad (2.61)$$

where day is the Julian day of the year. Julian days are defined in this study as the day number of the year, ranging from 1 on 1 January to 365 on 31 December. E_o (in (2.58)) can be estimated by,

$$E_o = 1.000110 + 0.034221\cos(\Gamma) + 0.001280\sin(\Gamma)$$
$$+0.000719\cos(2\cos\Gamma) + 0.000077\sin(2\Gamma) \quad (2.62)$$

To obtain Angot's value (2.58) must be numerically integrated from hour angle zero (solar noon) to the sunrise hour angle, ω, and multiplied by two. ω is found from,

$$\omega = \cos^{-1}(-\tan(\phi)\tan(\delta)) \quad (2.63)$$

In this study, Gauss Quadrature is used as the numerical integration technique.

Clear sky radiation

When considering the attenuation of solar radiation by a cloudless atmosphere, the air is generally separated into five components: dry air, water vapor, carbon dioxide, aerosols, and ozone. Each has distinctive absorption bands and scattering properties.

A summary of the atmospheric attenuation of solar radiation (and absorption of terrestrial radiation) is shown in Figure 3. In this study, a model for clear day radiation developed by Bird and Riordan (1986), called SPCTRAL2, is employed. This model has proven accurate for estimating clear day insolation at sea level in Hawaii (Nullet and Ekern, 1988a). A description of the model will serve as both an introduction to the physical processes involved in depletion of solar radiation by a clear atmosphere and a summary of the SPCTRAL2 approach.

SPCTRAL2 parameterizes attenuation of the solar beam in 122 separate wavelength bands between 0.300 and 4.0 microns. Atmospheric transmittance after Rayleigh scattering is estimated by,

$$T_r = \exp(-m/(\lambda^4(115.6406 - 1.335/\lambda))) \qquad (2.64)$$

where λ is the wavelength and m is the optical mass estimated by,

$$m = (\cos(\tau) + 0.15(93.885 - \tau)^{-1.253})^{-1} \qquad (2.65)$$

Transmission after aerosol scattering and absorption employs the Angstom turbidity formula in,

$$T_{sa} = \exp(-m\beta_n\lambda^{-\alpha_n} \qquad (2.66)$$

where β_n and α_n are the Angstrom turbidity coefficient and wavelength exponent respectively. These factors depend on the physical characteristics of the aerosol.

Transmittance after water vapor absorption is estimated by,

$$T_w = \exp(-0.2385a_w WM/(1+20.07a_w WM)^{0.45}) \qquad (2.67)$$

where W is the precipitable water and a_w is the water vapor absorption coefficient as a function of wavelength. Ozone transmission is calculated by,

$$T_{oz} = \exp(-a_o O_3) \qquad (2.68)$$

where a_o is an ozone absorption coefficient and O_3 is the total ozone in atm-cm. Uniformly mixed gas transmittance is given by,

$$T_u = \exp(-1.41a_u m/(1+118.93a_u m)^{0.45}) \qquad (2.69)$$

where a_u is an absorption coefficient. Equations 2.64 through 2.69 express the direct beam radiation reaching the surface. The additional contribution of diffuse radiation is expressed primarily as a function of the single scattering albedo of the aerosol and of Rayleigh scattering.

For this study, several parameters are considered constant throughout the year, including ozone = 0.26 atm-cm and the Angstrom turbidity coefficient and wavelength exponent being 0.05 and 1.3. Precipitable water is considered to be 3.0 cm at sea level, declining to 1.5 cm at 1670 meters. Other parameters are as given by Bird and Riordan (1986). Solution to the model was

obtained by numerical integration through the daylight hours of each day of the year. The computer program, including numerical integration subroutine (Gauss quadrature), gauss weighting coefficients, and extinction coefficients for each wavelength band are given in Appendix E.

Clouds

The presence of clouds greatly complicates accurate prediction of incoming solar radiation both because of their enormous variability in location and annual and seasonal patterns and because of the complexity of calculations involved. The attenuation of solar radiation in clouds depends principally on absorption by water vapor and on Mie scattering. Water vapor absorbs solar radiation in the near infrared, as shown in Figure 3, and thus absorption is a function of the optical depth of water in the cloud. Mie scattering in a homogeneous cloud layer can be estimated, assuming completely diffuse scattering, by a two stream approximation (Paltridge and Platt, 1976),

$$(1/3^{1/2})dQ/d\tau_e = -Q + Q\,o_s(1-bf) + Q_r\,o_s bf \qquad (2.70)$$

where τ_e is the total extinction optical depth, o_s is the single scattering albedo, and bf is the fraction of

the radiation scattered into the backward hemisphere on a single scatter. Solution of (2.70) requires a parameterization of the path length as a function of wavelength.

Typically in climatology applications, because of the complexity of calculations and uncertainty in cloud properties and distribution, the reduction in solar radiation due to clouds is modeled using empirical equations derived from utilizing climatic average cloudiness or hours-of-bright sunshine. Such models are often place specific.

Advection

Advection is the horizontal transport of a quantity such as sensible heat, momentum, or water vapor. When one studies evaporation, advective effects become apparent in the presence of inhomogeneous terrain. Basically the air flow carries an upwind profile of humidity and sensible heat over a downwind terrain, over which the upwind profile would be out of equilibrium. Gradually, the profile adjusts to the new terrain and eventually reaches a new equilibrium. Some distance is required before the atmospheric profile changes from the upwind to downwind equilibrium states. The air layer

near the ground that changes profile is called the transition zone, and it is in this region that advection effects are most felt. Assuming the wind flow is horizontal and in the x direction, the adjustment of the atmospheric profile can be represented by the partial differential equations (Brutsaert, 1982),

$$udq/dx = d/dz(Kdq/dz) \qquad (2.71)$$

$$udT/dx = d/dz(KdT/dz) \qquad (2.72)$$

where T is a close approximation of potential temperature and K is the turbulent diffusion coefficient ($K_e = K_h$). The effect of advection at a site thus depends upon the distance from the upwind discontinuity, the wind speed and the differences in the equilibrium boundary layer profiles.

Three types of sensible heat advection effects on the evaporation rate are commonly recognized, the "clothsline effect", the "leading-edge or fetch effect", and the "oasis effect." The clothsline effect refers to mixing of the advected quantity through the canopy of downwind vegetation, for example, through the forest canopy at the edge of a cleared field. The fetch effect describes the development of the boundary layer over the downwind terrain. The oasis effect refers to an isolated terrain patch, such as an irrigated field.

Subsidence caused by cooling through evaporation at such patches contributes to the evaporation rate (Oke, 1978).

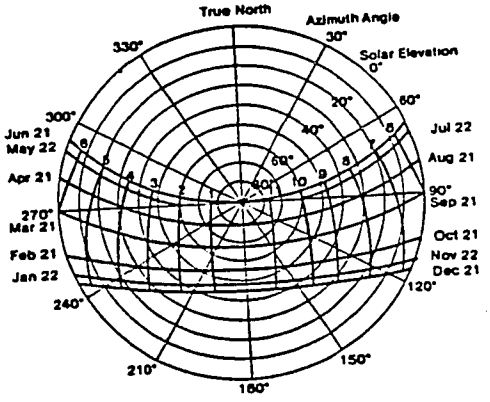

Figure 2. Sky chart for Honolulu, Hawaii

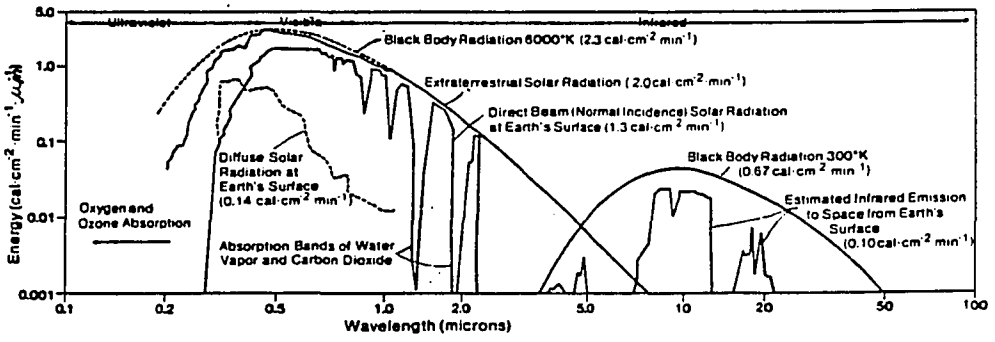

Figure 3. Electromagnetic spectra of solar and terrestrial radiation

III. STUDY SITE AND DATA

This chapter presents a description of the principal study site and its climate and the data bases compiled for the study. Four basic sources of data are used: 1) long term climate measurements on the northwest flank of Haleakala, Maui (MauiNet), 2) short term evaporation measurements at several of the MauiNet sites in the winter of 1987-1988 and the summer and fall of 1988, 3) pan evaporation and solar radiation data collected by Hawaiian Sugar Growers throughout the state, and 4) Hilo rawinsonde observations.

Study Site

The island of Maui covers about 1888 square kilometers and lies in the north-central Pacific Ocean near 156° West longitude and 21° North latitude (Figure 4). The study site faces the north and west and lies between elevations 180 m to 2130 m. The land cover consists of mixed pasture and cropland interspersed with native and exotic forest. In general, the vegetation is more profuse in the rainy areas grading to dryland scrub in the drier portions. The vegetation surrounding the

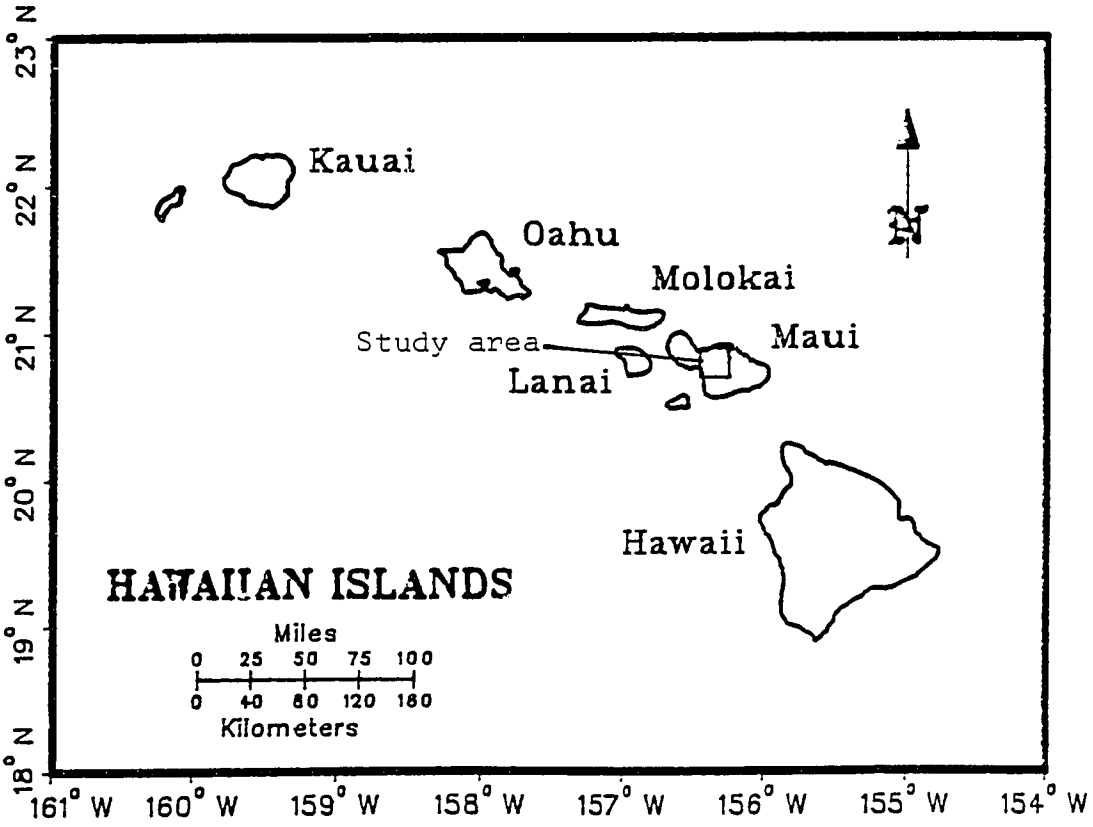

Figure 4. Location map

actual climate stations is, for the most part, grass of various heights.

The general oceanic climate in the area is dry, with about 700 mm rainfall annually, and days are generally sunny as a consequence of the stability provided by the persistent subsidence inversion normally present at 1800 to 2500 meters. Under steady northeasterly winds this inversion is often called the trade wind inversion, but subsidence inversions are also common under other wind flow patterns. In this study, the term inversion will be understood to mean a subsidence inversion under all surface wind flow conditions. Northeasterly trade winds dominate the surface air flow and consequently also dominate island weather patterns. This is most graphically demonstrated by presenting the mean annual rainfall map for the island shown in Figure 5 (from Giambelluca et al., 1986). The dominance of the tradewinds on airflow can also be seen in the average windflow pattern shown in Figure 6 (from Noguchi, 1979). A sea breeze circulation in the lee of Haleakala is also evident. The sea breeze is reinforced by a vortex in the lee of Haleakala, known locally at the Maui Vortex, during the day through the 600 to 1500 meter level (Leopold, 1949).

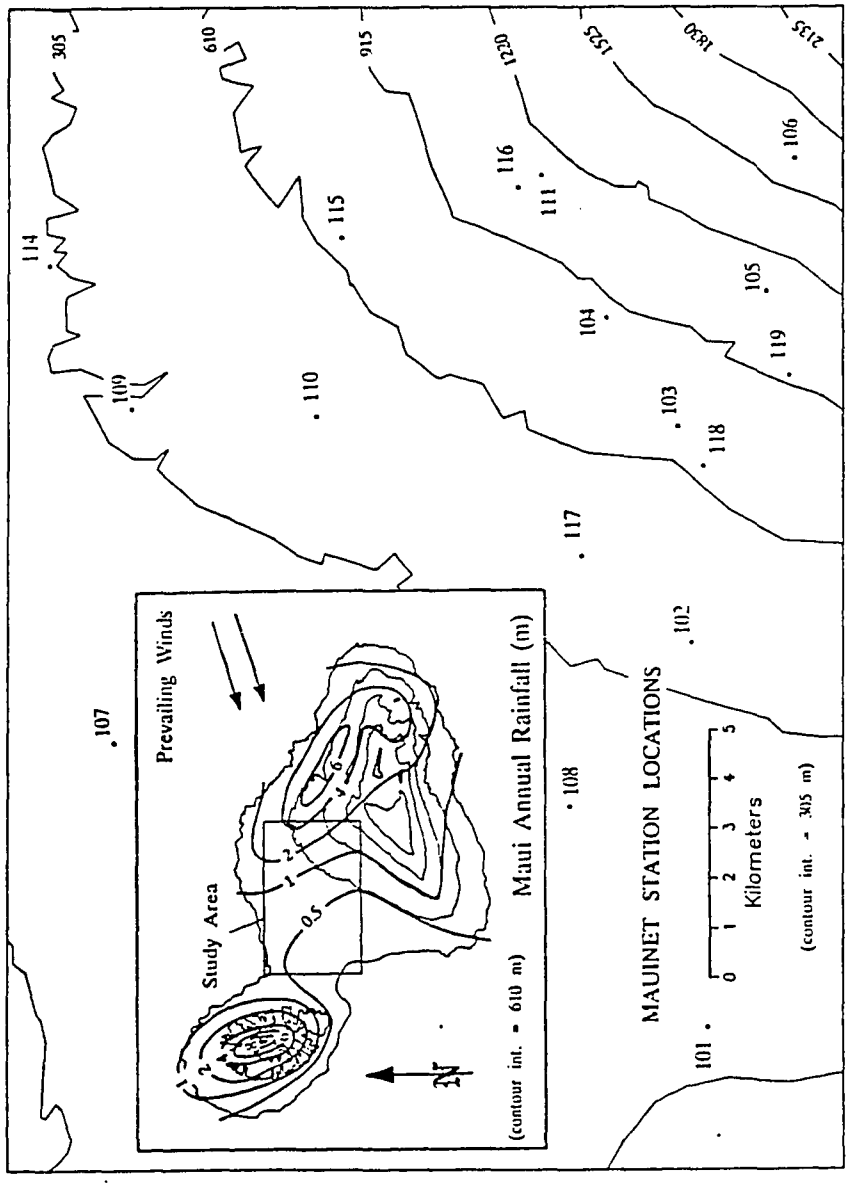

Figure 5. Mauinet station locations

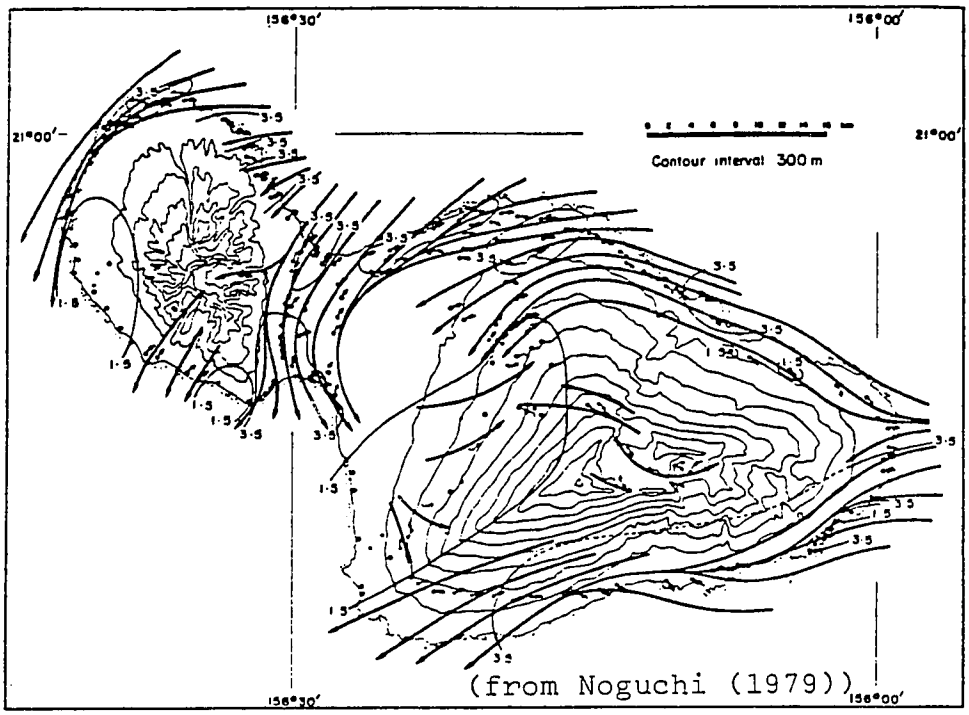

Figure 6. Wind flow over Maui

MauiNet Data

The study site (Figure 4) lies on the northwest flank of Haleakala, Maui. This location was chosen because of the availability of the extensive mesoscale climate-monitoring network that comprises MauiNet, and because of excellent access to wide variety of climatic regimes found on the mountain. MauiNet was established in conjunction with the University of Hawaii College of Tropical Agriculture and is used for a variety of agricultural research projects. The location of the stations is shown in Figure 5 and station information is given in Appendix A.

The network has been in place since July, 1983 (periods of record for individual stations are given in Appendix A). Data are logged on Campbell CR-21 Dataloggers. Measurements include solar radiation (Licor LI-200S silicon cell pyranometers), maximum, minimum, and average temperature (Fenwal UUT-51J1 thermistors), maximum, minimum, and average relative humidity (Phys-Chemical Research Model PCRC-11 sensor), and, at some sites, rainfall, soil temperature and moisture, and wind.

The MauiNet data was provided by Haruyoshi Ikawa

of the University of Hawaii Department of Agronomy and Soil Science in raw form, that is, exactly as read from the CR21 data loggers, as daily totals or averages. Seventeen of the sites were chosen for analysis based on length of record. The data was provided in 50 or 60 files that were then condensed into a single file for each of the 17 stations. The accumulated data comprised about 1.5 megabytes. The raw data required considerable modification before it was suitable for analysis. First a list of the periods of record and missing periods (sometimes several months) was accumulated. Next a number of unreadable characters, double records, and related problems had to be combed from the data. Then a list of obviously erroneous data was compiled. This involved graphing each climate element in turn at each station and looking for outliers. Finally, the solar radiation and humidity data had to be adjusted because of sensor drift or calibration differences. These corrections are on file with the Department of Agronomy and Soil Science.

The problem with the relative humidity sensors is illustrated in Figure 7 for the case of Station 106. The jumps correspond with sensor changes. Virtually all of the humidity sensors showed approximately the same

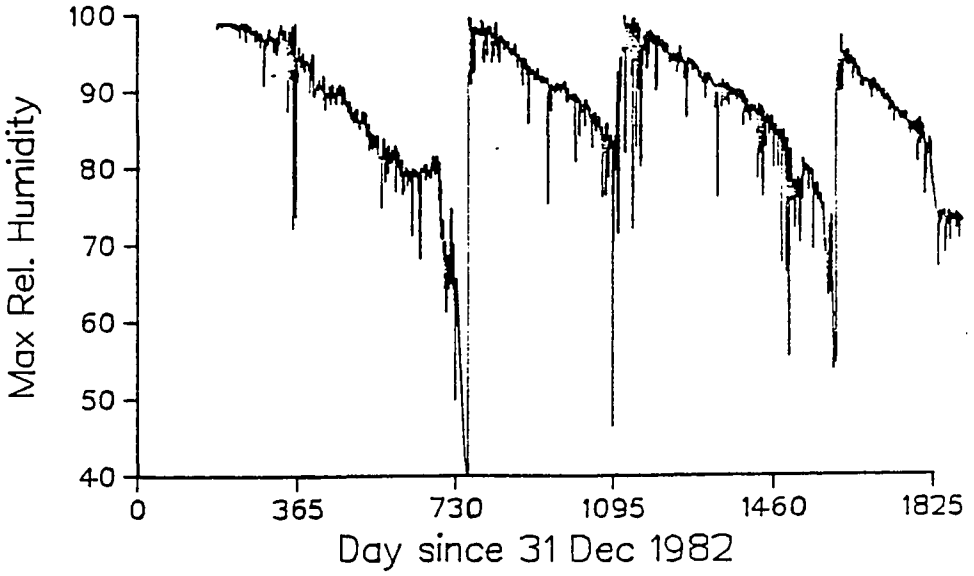

Figure 7. Humidity sensor decay at station 106

linear decline. The small variability seen in the maximum relative humidity values suggested a method of rehabilitating the data. All humidity data were increased by an amount equal to the average maximum humidity measured when the sensor was new minus the current maximum humidity.

The solar radiation sensors did not exhibit obvious drift but they had never been intercalibrated. The effect of this is illustrated in Figure 8 for the case of station 108. In this figure measured daily solar radiation (plotted for convenience by Julian day) is compared with a modeled clear day radiation baseline. The jump in measured radiation compared to the clear day baseline is clearly visible at the time of the sensor change. Some the stations had as many as two sensor changes, each with a different calibration. To standardize the solar radiation data, readings from each sensor were compared with the clear day baseline values (the clear day radiation model is discussed in Chapter II) and a linear correction factor thus derived. These factors ranged from 0.92 to 1.10. This standardization procedure also negates the effects of local shadows on the instruments.

To map solar radiation it was necessary to account

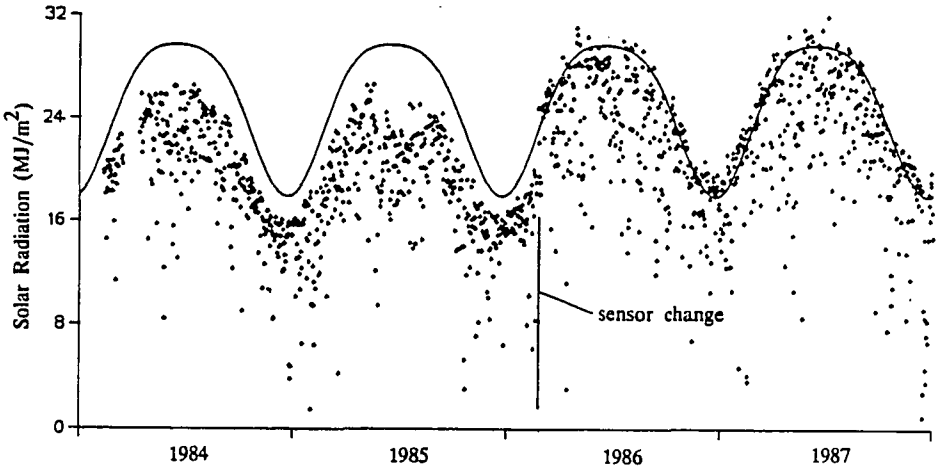

Figure 8. Measured global radiation and modeled clear-day radiation at station 108

for missing periods and to standardize data to a common base period. Missing periods were accounted for by multiplying station values by the ratio of the average clear day radiation for the winter, summer, and year by the ratio of the average modeled clear day value for the entire period to the average modeled clear day value for only the days with measured solar radiation. Data were adjusted to account for different periods of record by assigning each year a factor based on the long term-stations 104, 106, and 108. These factors were 1983:1.06, 1984:1.01, 1985:1.04, 1986:1.00, 1987:1.01. In essence, this standardized each year to 1986.

Evaporation Measurements

Between mid-November, 1987 and early January, 1989, two field experiments at the study sites were conducted. During the winter of 1987-1988, evaporation was measured using Ekern Evaporimeters at six sites (106, 114, 115, 116, 117, 119). In addition, net radiation (Fritchen-type net radiometer) and wind (pulse counting anemometers) were measured at three sites (106,116,117). The Ekern Evaporimeter was developed by Dr. Paul Ekern and is described in Ekern (1983). The instrument is a 6" PVC cap reservoir containing a 6" black carborundum

stone evaporating surface. Each morning the reservoir is filled and the volume recorded. The previous day's evaporation rate is then obtained by dividing the measured volume by the surface area of the instrument. Ekern recommends multiplying evaporimeter evaporation by 0.54 (Ekern, 1982b) to correspond to pan evaporation. Wind and net radiation were recorded on Licor model 1000 data loggers. The evaporation stations (see Figure 5) were chosen to represent both high and low rainfall transects and represent an elevation gradient from 287 meters to 1646 meters.

In addition to monitoring evaporation at six sites, two brief experiments were conducted to test the properties of the Ekern Evaporimeter. First, a net radiometer was placed under the rain shield and recorded values compared with adjacent net radiation measurements over grass. The purpose was to explore a possible cosine effect, i.e. a possible increase in reflection of solar radiation from the plastic evaporimeter shield at low solar angles. A sample day is shown in Figure 9. The figure shows a fairly constant ratio of shielded radiometer to open radiometer during the daylight hours averaging about 0.9, indicating that the cosine effect due to the plastic shield is not significant. The

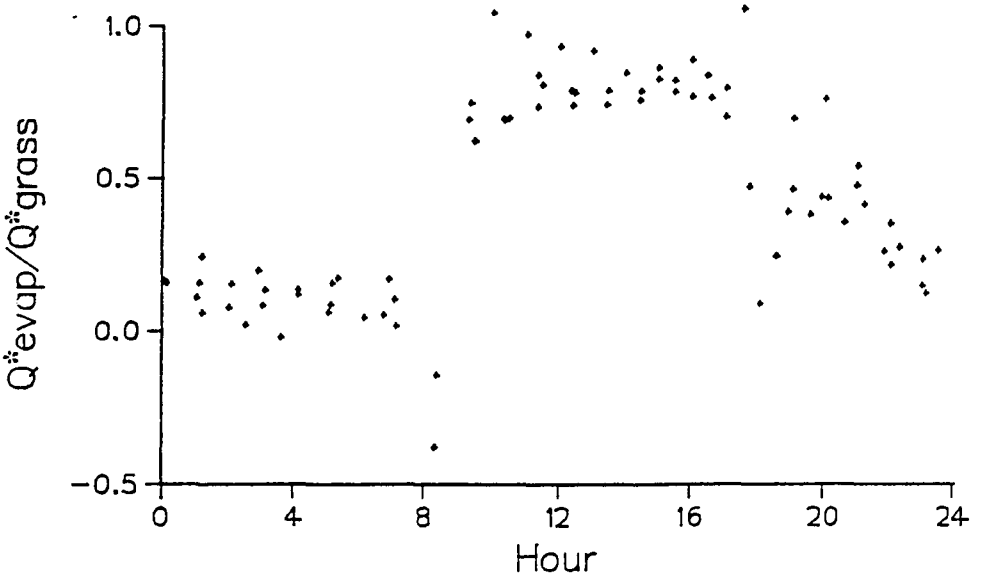

Figure 9. Net radiation comparison

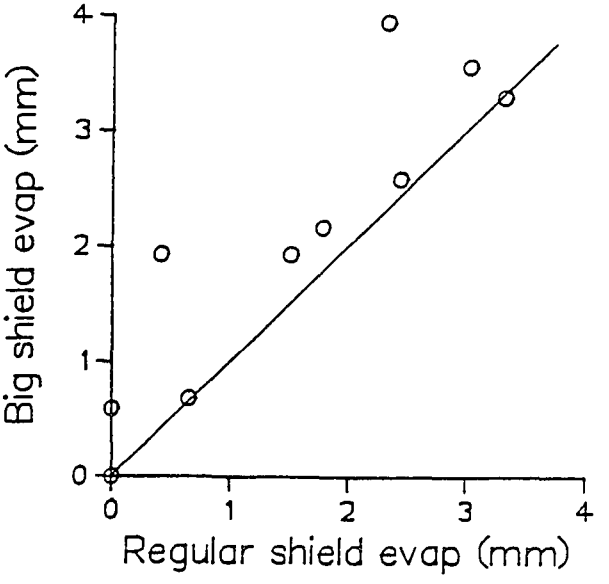

Figure 10. Shield size comparison

second experiment explored possible wetting of the instrument evaporating surface by windblown rain. An evaporimeter with a large shield (0.6 x 0.6 meters) was maintained alongside an instrument with a regular shield (0.35 X 0.35 meters). The results for eight days are shown in Figure 10. As evaporation values for the instrument with the large shield are all higher than the one with the regular shield, it is apparent that some rain falls on the evaporimeter despite the shield. This phenomenon had been observed earlier on rainy, windy days when measured evaporation was zero. The results suggest that the instrument underestimates evaporation on high wind speed, rain days. This effect must be especially pronounced in cloudy areas of the mountain where the drop sizes are small and more buoyant. Accordingly, several days of measurements have been discarded.

In the summer of 1988, a second series of evaporation measurements began at stations 106, 119, and a new high elevation site at the Haleakala National Park Ranger Station at 2100 meters. A modified version of the Ekern Evaporimeter was used). This instrument is capable of continuous recording through an optical sensor, which monitors drops that are fed to the

carborundum stone system described above according to the atmospheric demand. Net radiation, wind, temperature, and humidity were also recorded.

Pan Evaporation and Solar Radiation Data

To study the effects of advection (Chapter VI), estimated evaporation based on solar radiation data was compared with pan evaporation at 49 sites located throughout the Islands. Pan evaporation (Ekern and Chang, 1985) and solar radiation (How, 1978) measurements in Hawaii have been published by the State of Hawaii. Most of these data were collected by the Hawaiian sugar growers and disseminated through the Hawaiian Sugar Planter's Association. Pan data have been standardized to the US Weather Bureau Class A evaporation pan configuration according to standardization factors developed by Ekern and Chang (1985). Corrections range from +8% to -20% depending on the height of the pan above the ground, color and composition fo the pan, and the presence or absence of a screen.

The solar radiation data used in the comparison were measured by wig-wag integrators. These field instruments utilize vapor pressure changes to force

anhydrous methyl alcohol against gravity and alternately expose spherical sensors to sunlight. The number of times the sensor alternates is a measure of the radiant energy falling on the sensor. This value is converted to global radiation totals on a horizontal surface by calibration values worked out by comparison of monthly totals to a reference pyranometer. Han-Shun-Cheong (1972) gives a detailed description of these instruments.

Rawinsonde Data

The nearest station with regular rawinsonde observations is Hilo, approximately 150 kilometers to the southeast, on the windward shore of the island of Hawaii. These data were available from the National Center for Atmospheric Research in Boulder, Colorado through 1986. Only midnight and noon GMT observations (local time is ten hours earlier) were used and only at the standard levels (every 50 mb including surface) to 500 mb. The data have been quality controlled by the National Climatic Data Center and include wind speed and direction, geopotential height, relative humidity, and air temperature. Hilo is not an ideal location to use as a baseline site because of the influence of the large

mountains to the West on air flow. Nonetheless, it is the closest station and provides coherent atmospheric profile results, as discussed in Chapter VIII.

IV. FIELD WORK

This chapter reports the results of evaporation measurements in the winter of 1987-1988 at six sites (MauiNet stations 106, 114, 115, 116, 117, and 119) and in the summer and fall of 1988 at three sites (119, 106, and 151). Measured evaporation is compared with evaporation estimated by several meteorological methods. This comparison as a serves basis for the discussion of climatic controls on the evaporation rate to be discussed in subsequent chapters.

Models

Net radiation was measured at stations 106 and 117 between 24 November and 4 December 987 and at stations 106 and 116 between 24 December 1987 and 9 January 1988. These data were used to calibrate a model for estimating net radiation from solar radiation, temperature, and humidity. The model is based on the radiative energy balance equation

$$Q^* = (1 - \alpha)K + L^* \qquad (4.1)$$

where Q^* = net radiation (MJ m^{-2}), α = the albedo, K = global radiation (MJ m^{-2}), and L^* = net longwave

radiation (MJ m^{-2}). Net longwave radiation was estimated using a modified version of a formula suggested by Doorenbos and Pruitt (1977). The modified equation makes use of measured global radiation as an index of the effect of cloud cover on outgoing longwave radiation (replacing their hours of bright sunshine term) and takes account of diminishing optical mass with increasing elevation. The modified equation is:

$$L^* = \sigma T^4 (0.34-0.044 e_a^{0.5}) (1000/p) (K/K_{cd})^{\beta} \quad (4.2)$$

where σ = the Stefan-Boltzman constant ($5.67(10^{-8})$J m^{-2} T^{-4} sec^{-1}), T = temperature (^oK), e_a = vapor pressure (mb), p = atmospheric pressure (mb), K_{cd} = clear day global radiation at sea level (MJ m^{-2}), β = an empirical exponent. For α = 0.19 and β = 2.0, residuals (modeled minus observed net radiation) for stations 106, 116, and 117 were 0.2, -0.1, and -0.1 MJ m^{-2} for average measured net radiation of 6.8, 5.9, and 9.4 MJ m^{-2} respectively. Correlation coefficients between measured and modeled daily net radiation were 0.82, 0.97, and 0.88 respectively for the three stations.

Four evaporation models were tested: the original Penman (1948) equation and three modified versions of it, Van Bavel (1966), Monteith (1965), and Priestley-

Taylor (1972). Penman's original equation is given by (2.17). For the aerodynamic term $(f(u)(e_{a*}-e_a)=E_a)$ Penman originally proposed,

$$E_a = (0.263+0.138u)(e_s-e_d) \qquad (4.3)$$

where e_s = saturation vapor pressure of the air (mb), u = wind speed at two meters height (m s^{-1}) and the resulting E_a is in mm per day. (Calculations here including atmospheric pressure dependence (Storr and Hartog, 1975) of the psychrometric constant.) Van Bavel suggested the same form as (1) but recommended a different E_a term, which, assuming ideal gas behavior, becomes:

$$E_a = 3150*u*(e_s-e_d)/(T(\ln(z_a/z_o))^2) \qquad (4.4)$$

where z_o = roughness length of the surface and z_a = wind measurement height (same units as z_o). The roughness length is estimated at 0.00002 m for this study (average for smooth surfaces (Brutsaert, 1982)). Monteith (1965) suggested a new approach to modeling E_a that included a measure of the resistance to the diffusion of water vapor. This modification is generally known as the Penman-Monteith equation and is given in (2.26). In this equation, surface resistance is considered to be zero because the evaporating surface is wetted. Also c_p is equal to 1004.0 J kg^{-1} $^oK^{-1}$. The aerodynamic

resistance can be estimated by (Thom and Oliver, 1977):

$$r_a = 4.72(\ln(z_a/z_o))^2/(1+0.54u) \quad (4.5)$$

Priestley and Taylor suggested that, under certain conditions, the E_a term could be dropped entirely from the Penman equation. Instead a scalar was introduced (averaging 1.26 in their study) yielding (from 2.19):

$$E = 1.26(\Delta Q^*/\lambda)/(\Delta+\gamma) \quad (4.6)$$

Data from Winter Experiment

Weather instruments have been described in Chapter III. The field work yielded a dataset of 24 days with concurrent measurements of evaporation, solar radiation, temperature, humidity, and wind speed at the six sites. These five data matrices are given in Appendix B. (Temperature and humidity for nine days at station 106 were missing and had to be estimated using data from nearby stations by regression equations. Also, wind was not measured at the central stations (stations 119 and 115) of each transect, but was estimated as the average of the higher and lower site. Wind at stations 117 and 106 was measured at 2 meters, and at stations 116 and 114 at 3 meters.)

Results from Winter Experiment

Average evaporation values (adjusted to pan evaporation), estimated evaporation by each of the four models, and corresponding average solar radiation, temperature, vapor pressure deficit, and wind speed values, for 24 days of concurrent measurements are shown in Table 1. The spatial distribution of measured evaporation in shown in Figure 11 (residual values from the Penman equation are given in parentheses). Evaporation was greatest at the lowest and highest elevations along the low rainfall transect (stations 117, 119, 106) and least at the central elevations. The evaporation values shown for the low elevation stations 114 and 117 correspond well with long-term average values for nearby pan evaporation stations given by Ekern and Chang (1985). The station 114 average evaporation value of 3.6 mm day^{-1} compares well with the nearby pan evaporation station 486.5 average December value of 3.5 mm. The station 117 average of 4.2 mm day^{-1} compares well with the nearby pan evaporation station 317.1 value of 4.3 mm day^{-1} for December. The lowest average measured evaporation value, 2.4 mm per day at station 116, is just 57% of the greatest value at

TABLE 1. Winter evaporation comparison and data

Station	106 mean	114 mean	115 mean	116 mean	117 mean	119 mean
Penman	2.4	2.8	2.8	2.1	2.9	2.5
Van Bavel	1.9	2.5	2.4	1.8	2.6	2.2
Penman-Monteith	2.0	2.5	2.5	1.9	2.7	2.2
Priestley-Taylor	2.1	2.9	2.8	2.1	3.1	2.6
Evap. (mm)	4.2	3.6	3.0	2.4	4.3	3.1
Solar (MJ/m^2)	13.7	13.8	14.6	10.5	15.6	14.4
Temp. (^oC)	12.9	20.6	18.5	15.7	20.2	16.8
(e_s-e_d) (mb)	3.9	2.2	2.3	2.1	3.2	2.2
Wind (m/s)	1.5	3.6	3.0	2.4	1.7	1.6

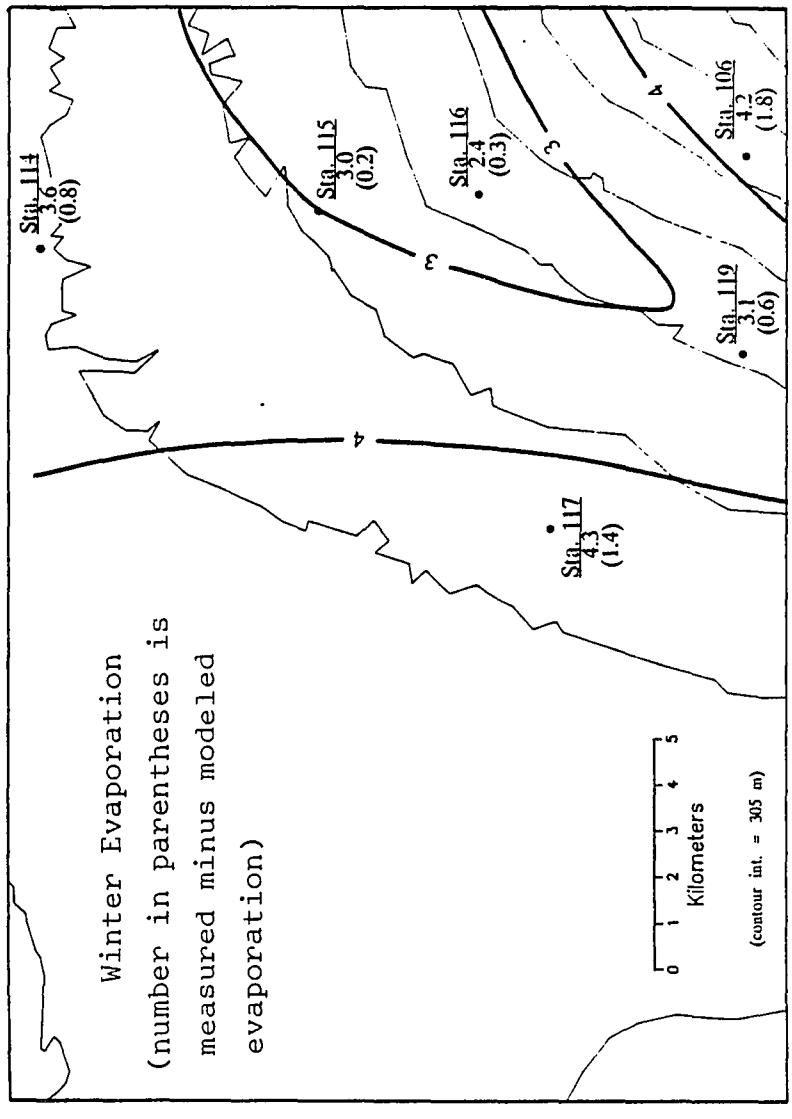

Figure 11. Average evaporation from winter experiment

station 117. Estimates using the original Penman equation provided the highest correspondence with measured evaporation. The Van Bavel and Monteith versions had slightly lower correlations. The Priestley-Taylor estimates were the least correlated with measured values, particularly at sites with the highest vapor pressure deficit.

Comparing daily means, all models underestimate measured evaporation at all sites. The least biased models are the original Penman and Priestley-Taylor equations. The closest correspondence between measured and estimated evaporation was found at the middle elevations between about 600 and 1200 meters (stations 115, 116, 119), a zone corresponding approximately to the cloud belt on the mountain. At the highest elevation site, station 106, evaporation was severely underestimated by all four models. In fact, measured evaporation here exceeded the evaporation equivalent of measured net radiation (1 mm evaporation = 2.47 MJ m^{-2} net radiation) by about 1 mm day^{-1}. Evaporation was also significantly underestimated by the models at the lowest sites, stations 114 and 117.

It is clear that standard evaporation models do not

adequately represent winter evaporation on Haleakala and that factors not included in the models play an important role determining the evaporation rate. For example, estimated evaporation (Penman) was just 57% of measured evaporation at station 106 and 63% of measured evaporation at station 117. For all but the highest elevation site, the probable source for the evaporation not explained by the given models, primarily dependent on radiative energy, is positive heat advection. Variations in radiant energy are discussed in Chapter V and advection is discussed in Chapter VI. At the highest elevation station, 106, mixing of dry air through the inversion and general subsidence above the inversion seems to provide quite a large energy source for evaporation. To study this phenomenon, a transect through the inversion was maintained in the summer of 1988. This experiment is detailed next.

Data from Summer Experiment

The purpose of this experiment was to examine the performance of the models described above in estimating evaporation at the higher elevations. Three sites were maintained on Haleakala between 15 June 1988 and 7 September 1988. They included stations 119 and 106, two

of the stations described in Chapter III, and a new site higher on the mountain at the Haleakala National Park Ranger Station, station 151. The sites form a transect on the western slope of the mountain at elevations of 945, 1645, and 2130 meters.

Each site was equipped with a pyranometer, net radiometer, anamometer, recording psychrometers, and a continuous recording evaporimeter. The first three instruments were described in Chapter III. The psychrometer is built with two thermistors, one of which is continuously wetted from a wick in a reservoir and aspirated with a small fan. The evaporimeter is similar to the Ekern Evaporimeter described in Chapter III except in place of the small reservoir that must be refilled each day, a large reservoir is provided. Water is fed to the carborundum stone through a small sealed tube which includes a view section through which the flowing water drips. The droplets interrupt a photocell beam. Each interruption is recorded as one count on the Licor data loggers. Data are recorded each hour. The calibration, determined on Oahu, is 46 drops/ml (Giambelluca, personal communication.)

Results from the Summer Experiment

Few concurrent evaporation measurements at all three sites were available because of the difficulty in maintaining the recording evaporimeters. Table 2 summarizes the periods of reliable data from the evaporimeters that coincide with complete measurements of net radiation, wet and dry bulb temperature, and wind. The actual daily totals and averages are summarized in Appendix C. In all, the data-set consists of 29 days of data at Station 119, 40 days at Station 106, and 14 days at Station 151.

TABLE 2 Summer Evaporation Periods

Station 119		Station 106		Station 151	
Begin (MMDD)	End (MMDD)	Begin (MMDD)	End (MMDD)	Begin (MMDD)	End (MMDD)
0707	0722	0617	0618	0617	0619
0810	0820	0715	0820	0707	0717
0902	0903	0906	0906		

Measured daily evaporation is compared with evaporation estimated using (4.3) through (4.6), (2.17) and (2.26). The results of this comparison, as well as average values of net radiation, wind speed, vapor pressure deficit, and air temperature, are given in Table 3. The vapor pressure deficit values at stations 106 and 119 have been corrected by comparing recording psychrometer data with Mauinet data. Accordingly, the vapor pressure deficit values were reduced to 56% and 52% at stations 106 and 119, respectively, of the original measured values. Table 3 shows that the models which incorporate an aerodynamic term vary more at the higher elevation sites. At the lowest site, with more moderate wind and vapor pressure deficit values, the models were better behaved. The Van Bavel (Van Bavel, 1966) model yielded the largest average residual (measured minus estimated evaporation), 0.9 mm, and the Penman (1948) model the smallest at 0.5 mm. It should be noted here that residuals from the Penman-Monteith model are an artifact of the selection of surface and ai· resistance values which could be adjusted to give zero residuals. It is interesting to note that while average net radiation declined between 945 meters at

TABLE 3. Summer evaporation comparison and data

	STATION		
	119 mean	106 mean	151 mean
Penman (mm/day)	3.3	3.2	5.2
Van Bavel (mm/day)	3.1	2.8	4.6
Monteith (mm/day)	3.2	2.9	4.8
Priestley- (mm/day) Taylor	3.8	3.0	4.9
Evap. (mm)	3.3	3.6	6.4
Net Rad. (MJ/m^2)	10.9	8.8	14.8
Temp. (^oC)	18.3	15.7	13.0
(e_s-e_a) (mb)	2.6	4.7	6.0
Wind (m/s)	0.9	1.8	2.8

Station 119 and 1645 meters at Station 106, evaporation increased. This suggests an additional energy source for evaporation at the higher elevations, an observation that is explored further in Chapter VII.

The 15 June 1988 through 7 September 1988 average data are concurrent for each station and can be used as a baseline comparison for the non-concurrent data shown in Tables 3 and 4. The concurrent data suggest that the average measured evaporation at stations 119 and 106 are somewhat lower than would be the case with complete records, and that evaporation at station 151 is somewhat higher.

TABLE 4. Estimated summer evaporation comparison

		non-concurrent		concurrent		
Station	Elev. (m)	Evap. (mm)	E_{pt} (mm)	E_{pt} (mm)	Q^* (MJ/m^2)	T_a (^oC)
119	945	3.4	3.8	4.1	11.6	18.3
106	1645	3.7	3.0	3.2	9.3	15.8
151	2130	6.4	4.9	4.4	13.4	12.8

(E_{pt} is evaporation estimated using Eq. 4.6)

Calibration of Atmometers

Additional evaporation measurements with the recording evaporimeters in September and October, 1988, at stations 106 and 151 yielded data that appeared to

contradict the summer measurements (data summarized in Appendix G). Evaporation data at station 106 were quite similar to the summer measurements but evaporation at the highest station, 151, was anomalously low. In an attempt to resolve this discrepancy, a field trip was conducted to Maui in January of 1989 to compare the recording evaporimeter measurements with non-recording Ekern evaporimeter measurements. The data are summarized in Appendix H. Based on the data gathered, the following conclusions were made: (1) The calibration of 44 counts/ml at station 106 based on 5 days of measurements suggests that the 46 counts/ml used in this study is valid, (2) Ekern evaporimeter data at stations 119 and 106 support conclusions based on both the summer and winter experiments (discussed in Chapters V, VI,and VII), (3) the recording atmometer at station 119 was malfunctioning (this instrument had been altered since the summer measurements), (4) data at station 151 is unreliable because persistent rain and mist continually wet the evaporation stone in high winds by blowing under the shields. Neither the recording atmometer nor the Ekern evaporimeter appear capable of accurately reflecting the atmospheric evaporation demand under wet, high wind conditions at this stage of their development.

V. RADIATIVE ENERGY

The results given in Chapter IV illustrate that solar radiation is the dominant energy source for evaporation on tropical islands (although, perhaps, the issue is open to debate for the highest station, 106). For example, the Priestley-Taylor equation, primarily dependent on solar radiation, provides evaporation estimates comparable to the other models that incorporate an aerodynamic term (see Tables 1 and 3). This is, of course, well known and explains why the Priestley-Taylor model, with its minimal input data demands, is popular. The reason net radiation is such a good measure of evaporation is that over the long term, it becomes the major source in the energy balance equation (2.6) while the major sinks become the sensible and latent heat fluxes to the atmosphere.

To understand the distribution of evaporation on the mountain, then, it is first necessary to understand the distribution of radiative energy. In this chapter the major sources of variation in the components of net radiation, solar and longwave radiation, are identified and discussed. Then these elements are combined to map

net radiation over the study area, and the resulting pattern interpreted in terms of variation in solar and terrestrial radiation. The long term MauiNet data serve as a database for the investigation.

Solar Radiation

The spatial variation in incoming solar radiation at the study site is shown in Figures 12 and 13. Figure 13 further shows the annual variation in insolation. The annual variation can readily be explained by the apparent motion of the sun throughout the year and subsequent changes in the length of daylight, sun angle, and intervening optical mass of the atmosphere. This annual cycle in clear-day radiation at Maui's latitude is illustrated in Figure 14. The SPCTRAL2 model (see Chapter II) was used to estimate clear-day values. Winter insolation is about 2/3 summer insolation. Only a slight (1%) annual cycle in atmospheric transmissivity has been reported over Hawaii (Pueschel et al., 1972) and thus the primary source of variation is simply the annual variation in the path of sun in the sky.

Year-to-year changes in solar radiation are primarily due to changes in average cloud cover. This can be inferred as no long-term trends in atmospheric

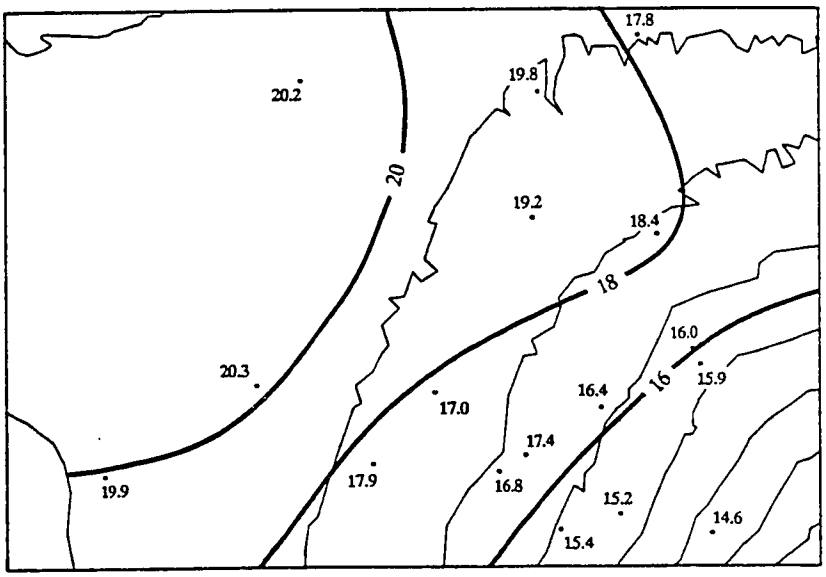

Figure 12. Average annual global radiation at Mauinet sites (MJ m^{-2} day^{-1})

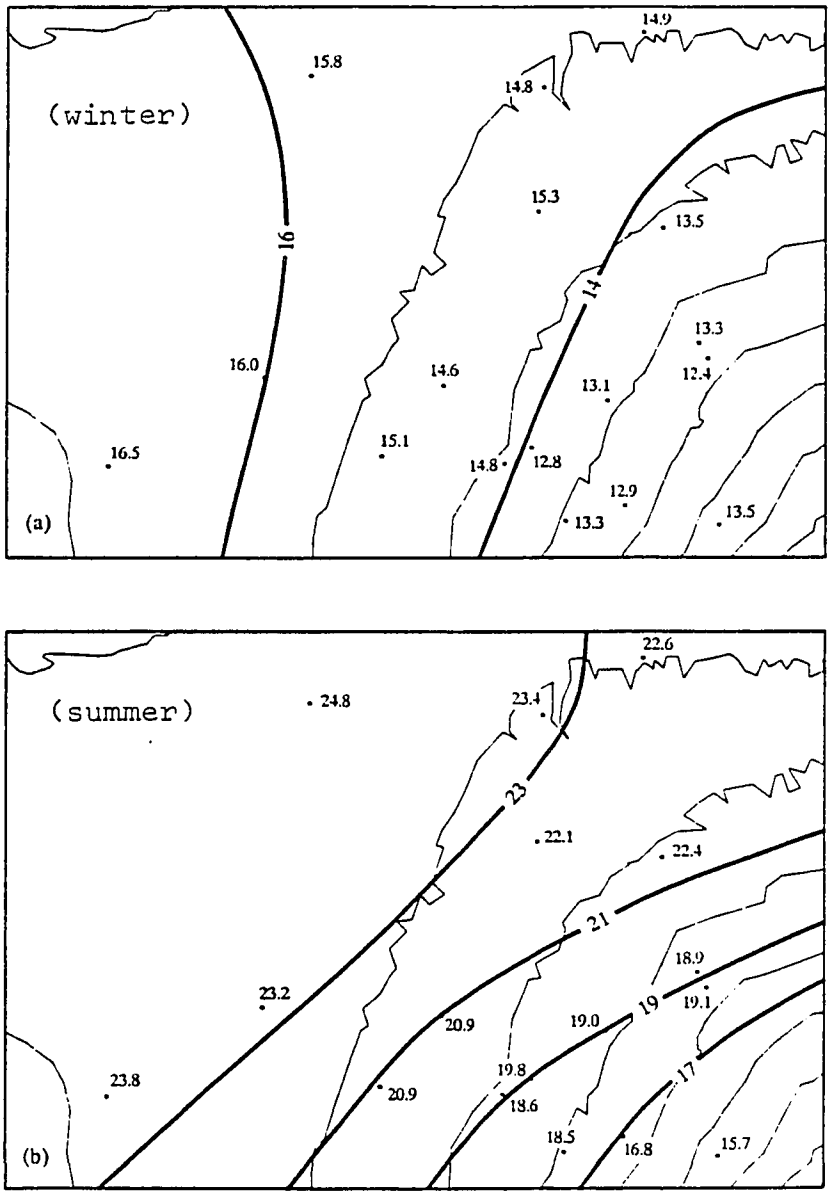

Figure 13. Average seasonal global radiation at Mauinet sites (MJ m^{-2} day^{-1})

transmissivity have reported (Szymber et al., 1985; Hoyt and Frolich, 1983). Short term variations in atmospheric transmissivity caused by volcanic aerosols, however, may significantly reduce insolation (Mendonca et al., 1978). For example, the aerosol cloud from the El Chichon eruption in Mexico in 1982 reduced global radiation at sea level in Hawaii by about 6% (Nullet and Ekern, 1988a). Cloudiness effects on radiation may show long term trends. A study has shown that radiation over the past 30 years has been steadily declining (Ekern, 1982a). It is possible that surface air temperatures, which have been increasing in Hawaii over this period, may somehow cause an increase in cloud cover and, consequently, have caused the observed decrease in solar radiation (Nullet and Ekern, 1988b).

It can be seen in Figure 14 that insolation at the higher elevation on clear days is about 7% higher than at sea level. This is because the optical mass of dry air decreases with elevation (about 17% lower at 1650 meters than at sea level) and because most of the water vapor in the atmospheric column is confined to the surface air mass below the inversion. A typical precipitable water profile is later shown in Figure 20. Water vapor absorbs solar radiation in several

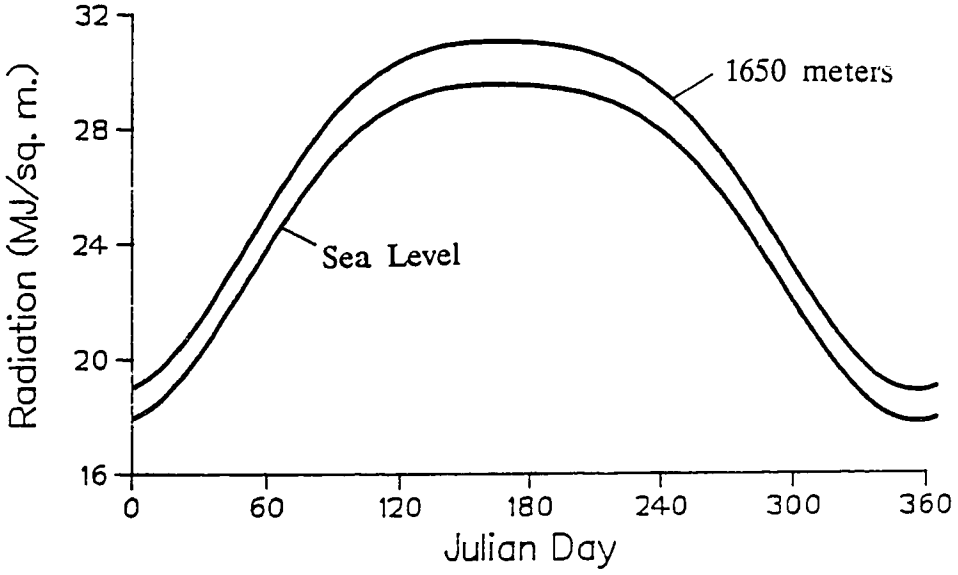

Figure 14. Modeled clear-day radiation

wavelength bands in the near infrared (Figure 3).

Although clear day radiation varies with elevation, the horizontal and vertical gradients in solar radiation seen in Figures 12 and 13 are primarily due to the influence of topography on cloud cover. Islands influence cloud formation principally through orographic uplift and by thermal circulations. A sense of the magnitude of insolation reduction of solar radiation by clouds can be given by mapping the percentage of clear-day radiation for summer and winter at the MauiNet sites (Figure 15). The percentage reduction in solar radiation from clear day values caused by clouds is simply 100 minus the values shown in Figure 15. It can be seen that reduction ranges from 15% at low, leeward sites in summer to 49% at the highest elevation in summer. It is also evident that annual differences exist in the reduction of solar radiation by clouds formed by local circulations. The drier leeward stations are more affected by daytime clouds in summer than in winter. This strongly suggests a more vigorous thermal circulation during the high-radiation summer period, as well as a more persistent Maui vortex. The dry leeward slopes and barren ground above the inversion heat up during the daytime and force

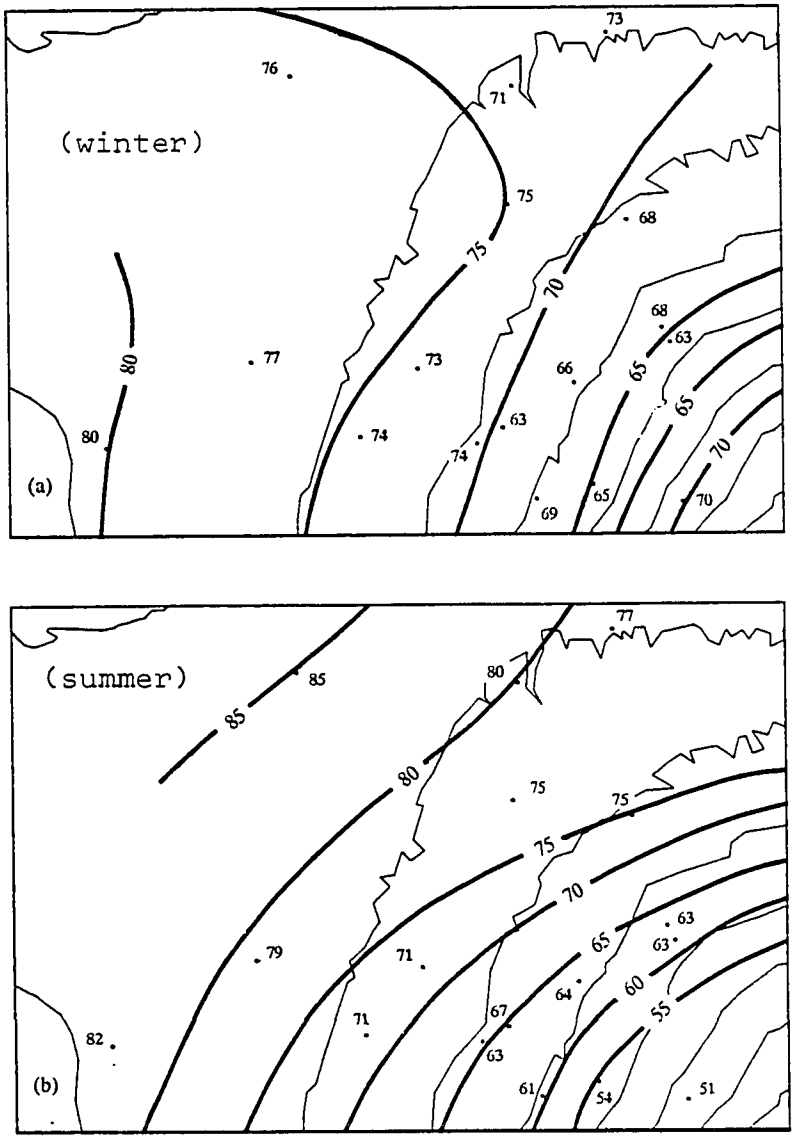

Figure 15. Percent of clear-day radiation reaching ground at Mauinet sites

sea and valley breeze circulations. The orographic cloud, whose influence is most evident in the reduction of solar radiation on the wetter sites, appears to exert a more uniform reduction in solar radiation throughout the year than the sea-breeze clouds exert at the leeward sites.

In comparing the reduction in insolation in winter and summer shown in Figure 15, it can be seen that the percentage reduction by clouds decreases with elevation from about 1200 meters in winter but increases in summer. Figure 15 also shows that horizontal gradients in insolation are more pronounced in summer than winter. This may be related to higher wind steadiness in summer. That is, the orographic cloud is a more or less permanent feature of the northwest ridge of Haleakala in summer, whereas in winter, orographic clouds forming on the western slopes of the mountain under Kona wind conditions may occur more frequently.

Although not evident in Figure 15, it has also been shown (Ekern, 1982a) that shadow and solar zenith angle can play important roles in the reduction in solar radiation at certain sites on tropical islands. For example, in south-facing valleys, the solar beam can penetrate below the stationary cloud deck at low solar

zenith angles in winter. At these sites, inland solar radiation may be only slightly less than coastal values. It can also mean higher winter insolation receipt in winter than summer at these sites. In contrast, at the foot of north facing cliffs, shadow may greatly decrease insolation.

Net Longwave Radiation

Net longwave radiation is an important component of the radiation balance given in (4.1). The net solar radiation minus net longwave radiation yields net allwave radiation, which is a measure of the radiant energy available for evaporation. Outgoing longwave radiation can be estimated by the Stefan-Boltman law,

$$L_o = \epsilon \sigma T_s^4 \qquad (5.1)$$

where ϵ is the surface emissivity, σ is the Stefan-Boltzman constant, T_s is in ^oK. The incoming longwave radiation is primarily a function of the amount of water vapor overlaying the site (precipitable water), the cloud cover, and the air temperature profile. These factors were included in the net longwave formula (4.2).

The primary sources of variation in net longwave radiation, then, are surface temperature, cloudiness, and precipitable water. The temperature within the

study site is shown in Figure 16. It can be seen that the primary source of variation is elevation and a typical lapse rate for both summer and winter is about $6^{o}C\ km^{-1}$. Slight horizontal gradients are also evident at the lower elevations. For example, average summer temperatures at station 102 are about $1.5^{o}C$ higher than those at station 114, which is at approximately the same elevation. The vertical temperature gradient would mean a reduction in outgoing longwave radiation of about 31 $W\ m^{-2}$ per kilometer or a reduction of about 7% of the sea level value per kilometer.

Figure 17 illustrates the distribution of average water vapor pressure on the mountain. As can be seen, the vapor pressure decreases with elevation. This is because water vapor pressure decreases geometrically with elevation and because of entrainment of dry air near the inversion. The vapor pressure distribution provides an indication of the precipitable water profile in the atmosphere.

To quantify the profile of the longwave radiation budget more accurately and to study the effect of the inversion discontinuity, temperature measurements were taken on the nights of 27 November 1987 and 7 January 1988. Surface and sky temperatures were measured with

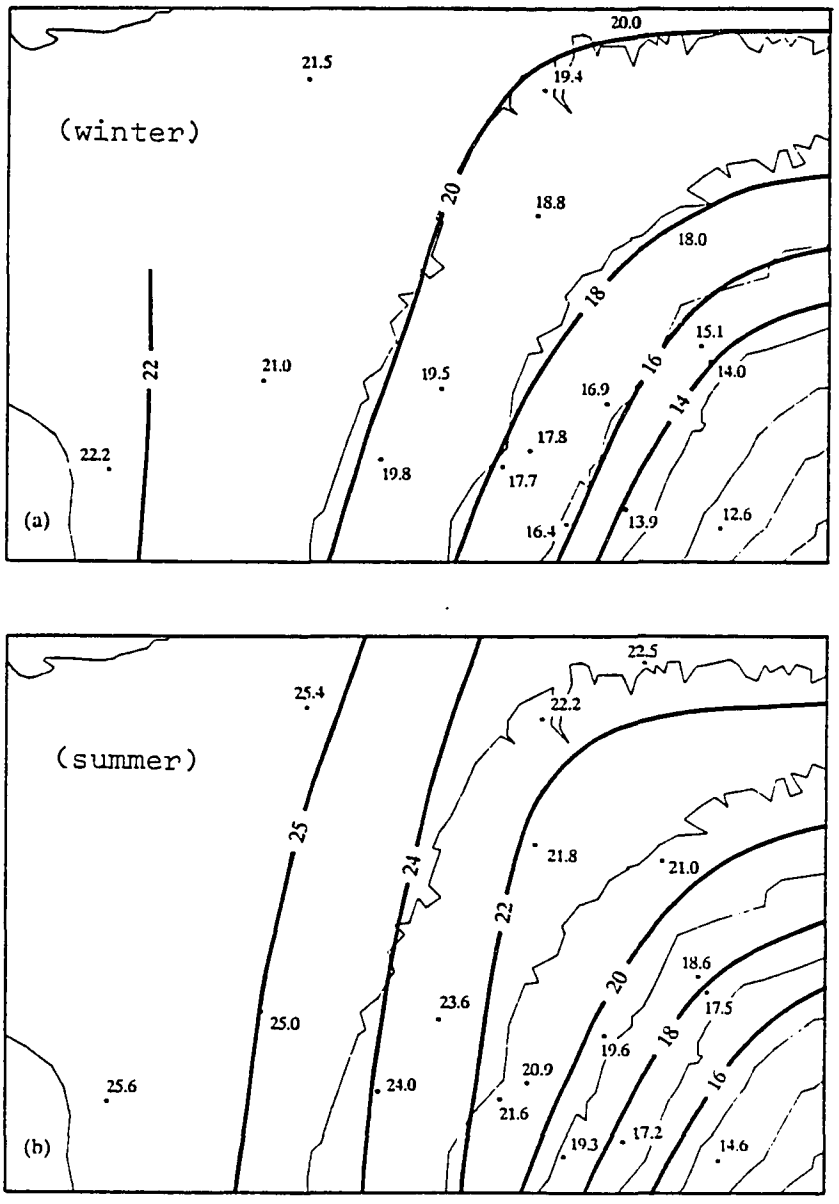

Figure 16. Average seasonal temperatures at Mauinet sites (°C)

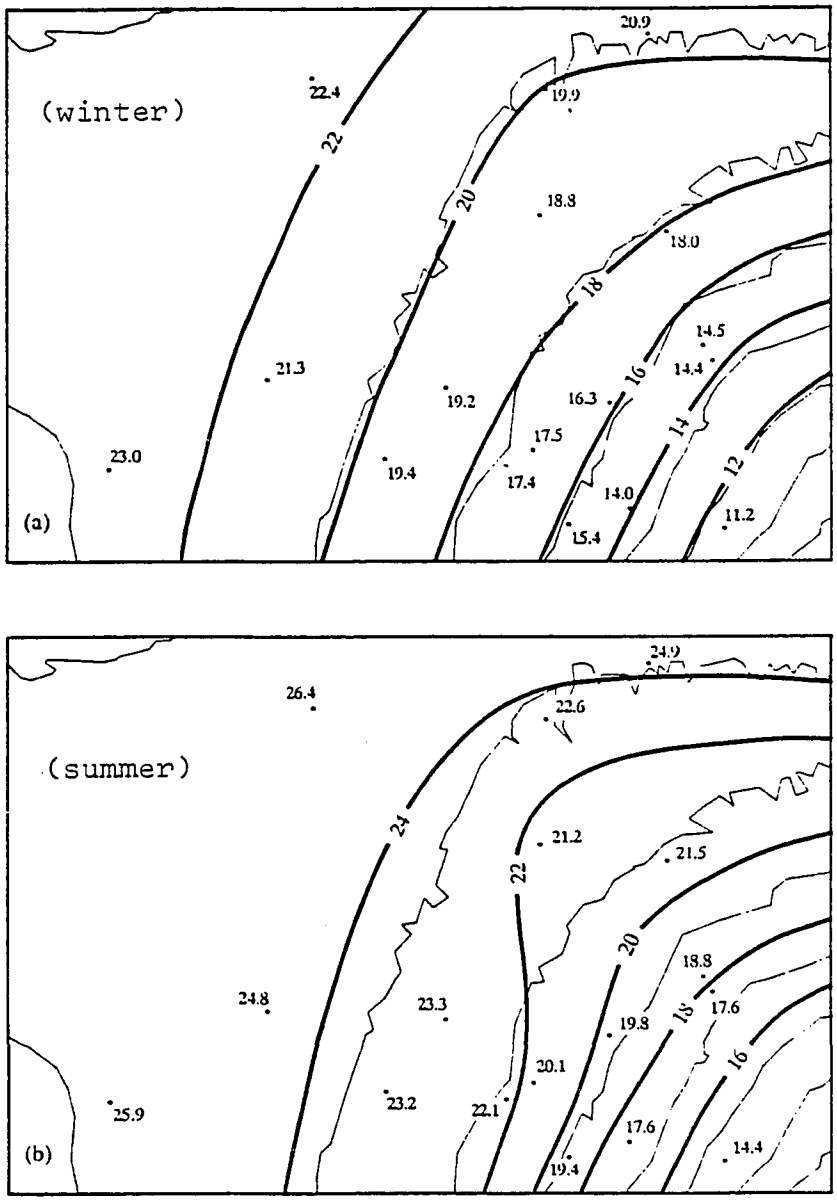

Figure 17. Average seasonal vapor pressure at Mauinet sites (mb)

an Everest Interscience model 210 infrared thermometer and dry and wet bulb ambient air temperatures were measured with an Assmann aspirated psychrometer. Surface temperatures were taken over vegetation, except for measurements above 750 mb where the slopes were devoid of vegetation. Sky temperatures were determined by the IR thermometer directed to the zenith. On at least one occasion (925 mb on 27 November 1988) clouds interfered with clear sky readings. The transects began at the highest point of Haleakalā, Red Hill, at 3055 meters elevation, at about 8:30 PM and ended at sea level approximately three hours later. Readings were taken at every 25 mb pressure interval. Atmospheric pressure and elevation were determined using a Lietz digital altimeter.

Data from the transects are given in Appendix D. Incoming and outgoing longwave radiation were determined using (5.1). The emissivity of the instrument was set at 0.98. The vapor pressure was determined using the equations of psychrometry. The saturation vapor pressure for any temperature is given by:

$$e_* = a_o+T(a_1+T(a_2+T(a_3+T(a_4+T(a_5+Ta_6)) \qquad (5.2)$$

where e_* is the saturation vapor pressure, T is air temperature in ^oK, and the coefficients are

$a_o = 6984.505294$, $a_1 = -188.9039310$, $a_2 = 2.133357675$, $a_3 = -1.288580973(10^{-2})$, $a_4 = 4.393587233(10^{-5})$, $a_5 = -8.023923082(10^{-8})$, $a_6 = 5.136820929(10^{-11})$ (Brutsaert, 1982).

The actual vapor pressure of the air is found by subtracting a correction from the wet-bulb temperature-saturation vapor pressure. This correction is given by:

$$d_g e = 0.000660(1+0.00115Tw)p(Td-Tw) \qquad (5.3)$$

where Tw is the wet bulb temperature in ^{o}C, Td is the dry bulb temperature in ^{o}C, and p is the air pressure in mb (List, 1966). The relative humidity is then (to a very close approximation) the actual vapor pressure of the air, ea, divided by the saturation vapor at ambient air temperature, e_*.

The water vapor density at each observation site can be found by applying the gas laws:

$$\rho_v = 0.622e_a/(R_w T) \qquad (5.4)$$

where R_w is the gas constant for water vapor (461.5 Joule kg^{-1} K^{-1}), T is the air temperature (^{o}K), e_a is given in Pascals, and ρ_v is given in kg m^{-3}.

Precipitable water is estimated for each layer by averaging the water vapor density at the top and bottom of each layer. The product of ρ_v (in kg-m^{-3}) and the depth of the layer it represents (in m) yields

precipitable water (ppw) in mm. For elevations above the 3055 meter level, it is reasonable to assume that, under average conditions, an additional 5 mm ppw might be found (Bodhaine and Pueschel, 1974). The total calculated ppw above sea level of 27.6 mm for the 27 November 1987 transect is in accord with other studies (Yoshihara and Ekern, 1978; Grody et al., 1980). The total precipitable water for the 7 January transect was 19.8 mm.

Results of the two transects are graphed in Figures 18 through 20. Incoming longwave radiation clearly decreases with height more rapidly than does outgoing longwave radiation despite the fact that, according to the exponential relationship in (5.1), equal reductions in ground and apparent sky temperature should have the opposite effect. This increase in longwave loss, then, must be due to the decline in absorption by atmospheric water vapor with elevation and consequently and more rapid decline in apparent sky temperature with height than in ground temperature. On a diurnal basis, measurements by Mendonca and Iwaoka (1969) on Mauna Kea show a fairly uniform changes in temperature at the surface between sea level and 3400 meters throughout the day in response to solar heating, with some distortion

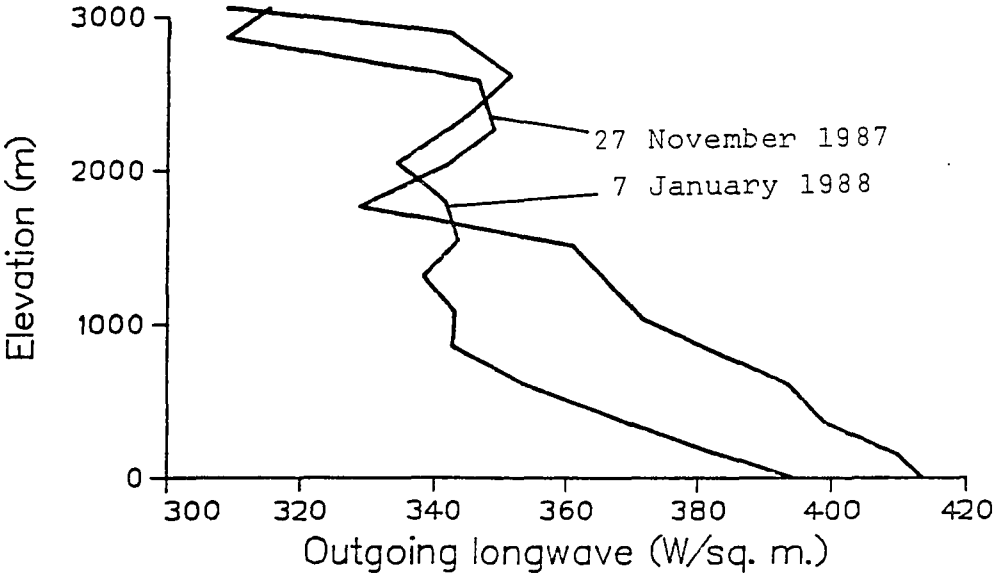

Figure 18. Outgoing longwave radiation transect

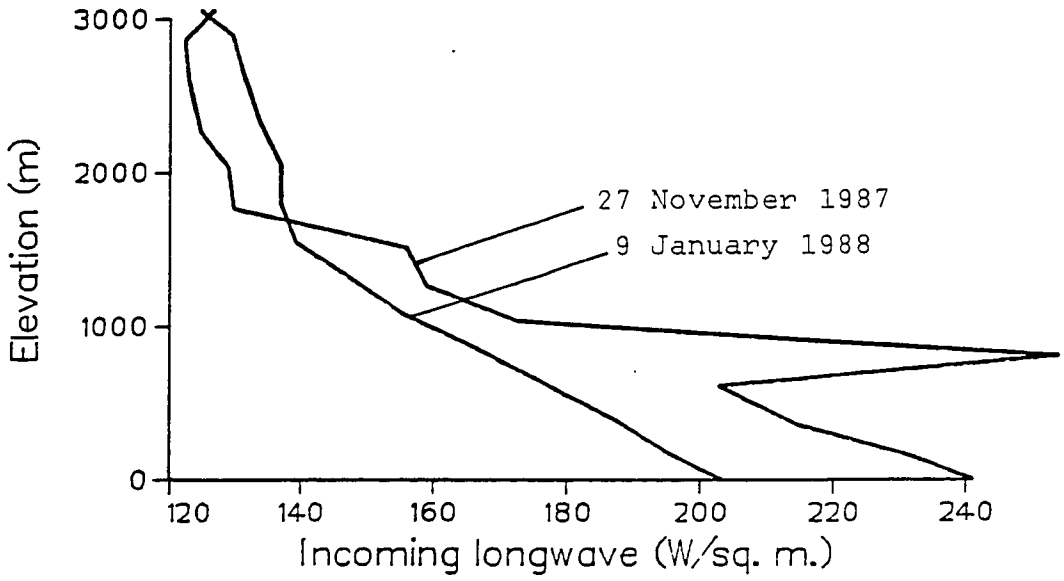

Figure 19. Incoming longwave radiation transect

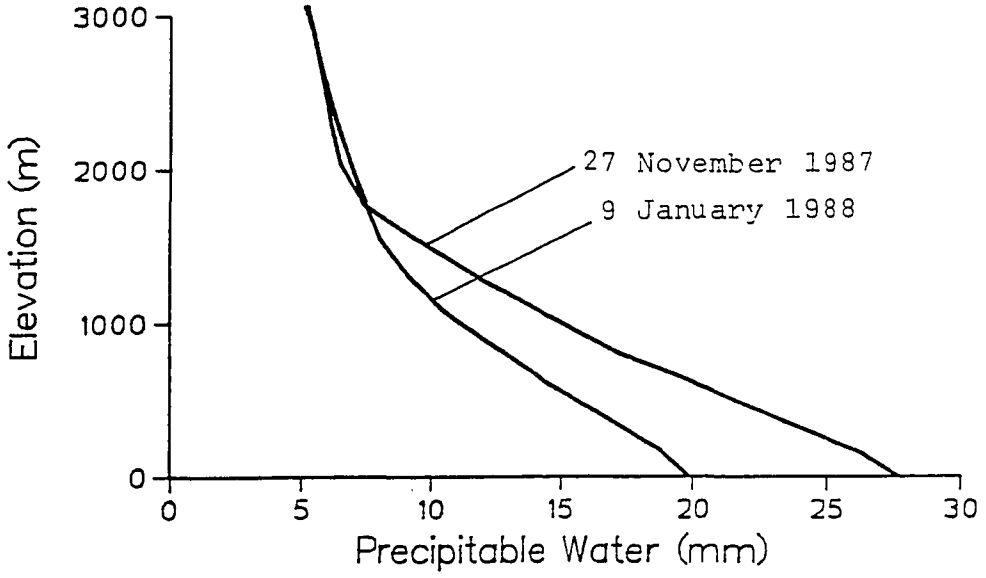

Figure 20. Precipitable water transect

near the inversion level.

According to (4.1), the observed increase in longwave radiation loss with elevation has the effect of decreasing the percentage of solar radiation retained as net radiation at the surface on a daily basis. Of course, the incoming longwave measurements do not represent hemispherical radiation but only a solid angle of about 20^{o} centered on the zenith. Nonetheless, sky radiation from all angles are closely related (Martin and Berdahl, 1984). The reason for the rapid decline in sky radiation is the decline in precipitable water with elevation, as shown in Figure 20. Water vapor is a very efficient absorber of longwave radiation. For example, 1 cm of water vapor will absorb 73% to 76% of emitted longwave radiation at 40^{o}C (Moller, 1951). The precipitable water vapor profile, and its effect on sky radiation, is the principal reason for the pressure correction in the net radiation formula (4.2) developed in Chapter IV.

The second obvious feature of the night temperature transects is the presence of a temperature inversion. The subsidence inversion over the Hawaiian Islands region is an upper air feature attributable to the adiabatic heating of descending air associated with

anticyclonic circulation. This type of inversion is often called a subsidence inversion. Other inversion types are ground inversions, formed on clear nights in stable air when outgoing longwave radiation rapidly cools the surface, and inversions associated with the movement of cold anticyclonic air at high latitudes. Inversions were present during both transects and are represented in the figures by the sharp slope breaks in the outgoing longwave radiation profiles. On 27 November 1987 the inversion began just below the 2000 meter elevation and on 7 January 1988 at a lower elevation near 1000 meters. We believe the latter transect to be nontypical because of the presence of two inversions.

Through and above the inversion the rate of decrease in incoming longwave radiation decreases as the rate of decline in precipitable water decreases. This indicates that the pressure correction in (4.2) may not be appropriate at the highest elevations. Some evidence of this contention can be given by the observation that the residual value of estimated net radiation by (4.2) minus measured net radiation at station 106 was positive, while that of the other two stations was negative. An interesting observation from the

7 January 1988 measurements between 1000 and 1500 meters is that although the outgoing longwave radiation profile breaks sharply at the inversion height, the incoming longwave radiation profile decreases more gradually, similar to the precipitable water profile. Thus incoming longwave radiation continues to decline sharply through the layer 1000 to 1500 meters while the outgoing longwave radiation profile stabilizes. This suggests that models that estimate sky radiation as a function of outgoing longwave radiation will be somewhat inaccurate. Above 1500 meters, the profiles are similar.

As a final note on the night-temperature transects, an attempt was made to model hemispherical longwave radiation. An equation given by Martin and Berdahl (1984), based on thousands of measurements in the continental U.S., was used that relates surface air temperature and sky radiation. The equation is,

$$_{s} = 0.711 + 0.56(Tw/100) + 0.73(Tw/100)^{2}) \qquad (5.5)$$

where $_{s}$ is the sky emissivity (sky radiation divided by black body radiation at the surface air temperature) and Tw is the wet bulb temperature. Estimates of hemispherical sky-radiation values (using (5.5)) were subtracted from measured outgoing longwave radiation

(ground temperature values from the night transects) and compared with measured hourly average net longwave radiation at stations 106, 116, and 117. The comparison is presented in Table 5 below.

TABLE 5. Estimated and measured net longwave radiation

Date	Time	Sta.	Q^* @2300 W/m^2	Q^* @0000 W/m^2	s	est. W/m^2
27Nov87	2202	106	-40	-59	0.78	-71
27Nov87	2310	117	-34	-33	0.84	-45
7Jan88	2210	106	-49	-49	0.73	-71
7Jan88	2245	116	-45	-46	0.75	-71

The estimates are all higher than measured values. The discrepancy may be due either to a deficiency in the model, or to the presence of clouds over the MauiNet sites at some point during the hours in which the average net radiation was recorded. Without actual simultaneous measurements of net radiation and sky and ground temperatures on the transect, it is impossible to tell whether or not the model is accurate. The estimates do seem reasonable, however, when compared with longwave radiation measurements from other studies. For example, Charnell (1963) found that nighttime net longwave radiation over the sea surface off Barber's Point on Oahu to range from 63 to 84 W m^{-2} under clear

skies. Ekern (1983) measured values over grass for an open ridge site (St. Louis Heights) at 60 to 62 $W\ m^{-2}$.

When clouds are present, net longwave radiation is greatly reduced. Cloud bottoms act as black body emitters at the cloud bottom temperature. Figure 15 gives an indication of the cloud pattern over the study site. In winter, cloud cover increases with elevation until about 1200 m and then decreases again. In summer, cloud cover decreases with elevation throughout the study area. Of course, this figure is only a measure of daytime cloudiness. Nighttime cloud cover is also important in the longwave radiation balance. In a study of summer weather on Haleakala, Lyons (1979) found a strong daytime cloudiness maximum (rising from 38% at 9 am to 75% at 4 pm) in the lee of Haleakala at the National Weather Service (NWS) US Weather Bureau (USWB) Raingage #191, near the MauiNet station 101. Higher on the slope at NWS USWB raingage #5003, near MauiNet station 106, the afternoon cloud maximum was much less pronounced, rising from 35% at 9 am to 55% at 4 pm. The afternoon cloud maximum was attributed to sea and valley breeze circulations. Diurnal cloud patterns are part of the difficulty in estimating net longwave radiation. In

general, this information is not available and models depend on daytime ground or satellite-based cloud observations, hours-of-bright-sunshine, or, as in this study, the percentage reduction of clear-day solar radiation as cloud indices.

In (4.2), the square of measured insolation over clear-day solar radiation was found to fit measured net radiation values well. This factor worked well for leeward (station 117), high elevation (station 106) and wet inland (station 116) sites. A possible physical explanation for the necessity of the exponent in (4.2) might be that thin cloud is more transparent to solar radiation than to longwave radiation. Thus, a small reduction in solar radiation might indicate a larger percentage reduction in net longwave radiation.

Net Allwave Radiation

To determine the combined effect of variations in solar and longwave radiation on net radiation, the primary energy source for evaporation, the average estimated net radiation for summer and winter over the study site has been mapped in Figure 21 using (4.1), (4.2), and the long-term MauiNet solar radiation data. As in Chapter IV, the albedo is assumed to be 0.19 and

β, an exponent used to model the effect of cloudiness in (4.2), is 2.

A couple of interesting features of the net radiation distribution are evident in Figure 21. First, the comparison of the seasonal maps reveals that in summer net radiation is a higher percentage of solar radiation than it is in winter. This is illustrated in Figure 22. In summer, net radiation averages a fairly constant 68% to 70% of solar radiation, regardless of location on the mountain. This is consistent with Ekern (1965) who found that net radiation averaged 2/3 of solar radiation over pineapple, sugar cane, and grass at low elevations in Hawaii. In winter, however, this ratio is lower, ranging from 0.63 at the lowest elevations to only 0.54 at station 106. This reveals another difference between the winter and summer ratio of net to solar radiation, namely, in winter a gradient is evident while in summer the gradient is absent.

These observations can be interpreted as follows. In Hawaii, the temperature remains fairly constant year round, yet solar radiation drops to 2/3 its summer value in winter (see Figure 14). However, as net longwave radiation depends on surface temperature, it remains fairly constant throughout the year. According

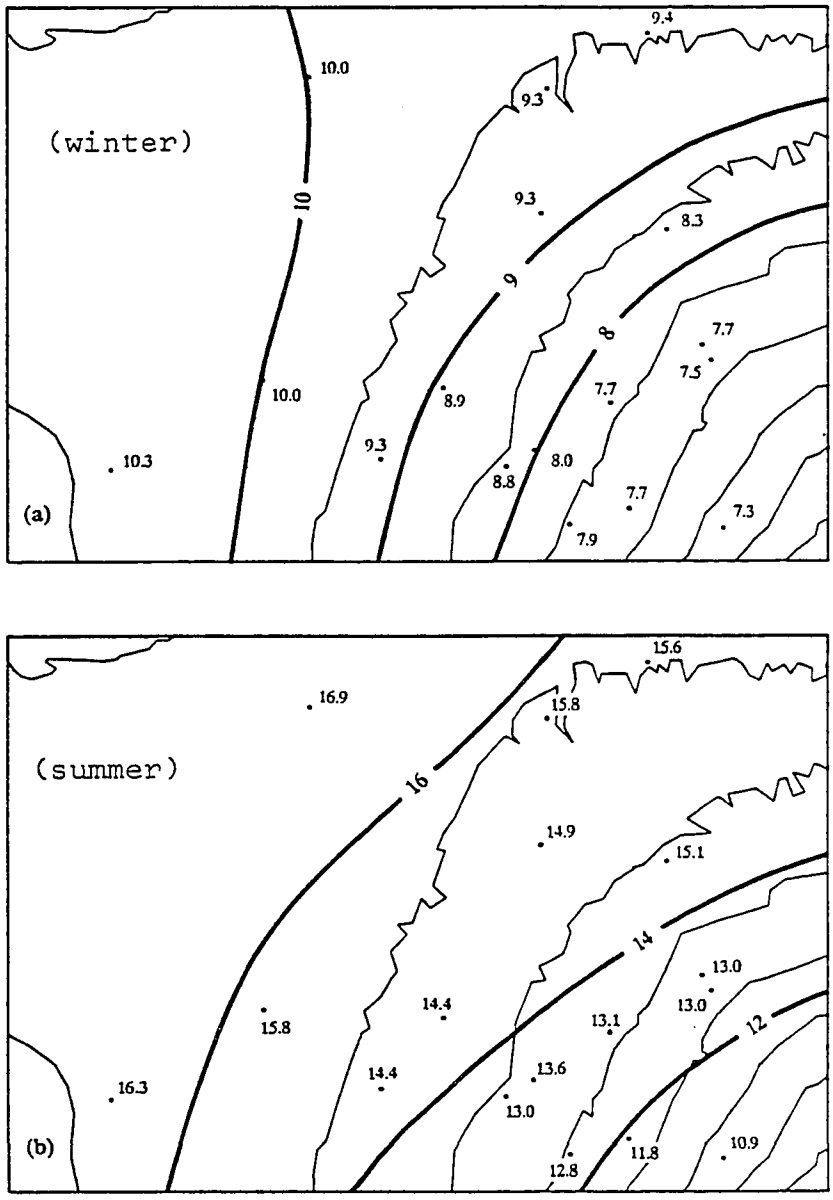

Figure 21. Average seasonal estimated net radiation at Mauinet sites (MJ m^{-2} day^{-1})

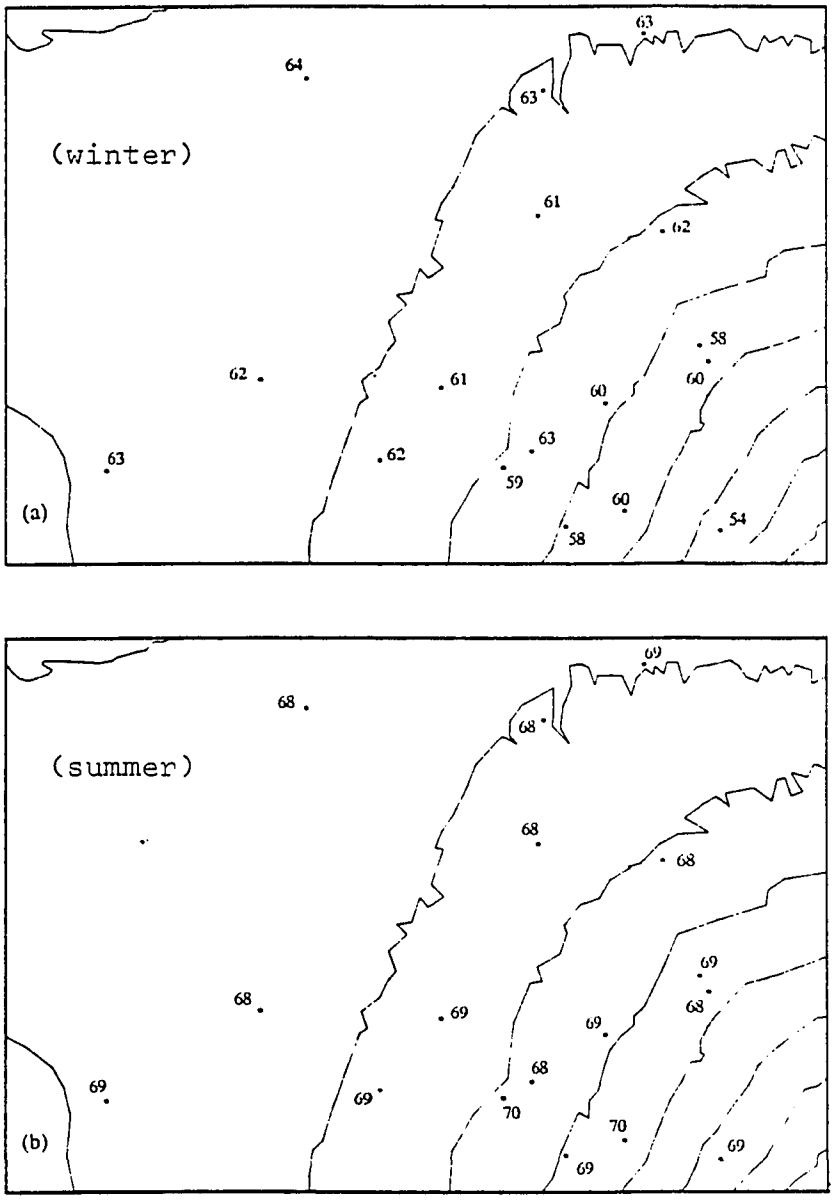

Figure 22. Average seasonal net radiation as a % of global radiation at Mauinet sites

to (4.1) then, the ratio of net to solar radiation would be higher in summer than winter and that is what is observed in Figure 22.

To explain the presence of a net to solar radiation ratio in winter and its absence in summer, it necessary to refer to Figures 15 and (4.2). Figure 15 shows that average cloud cover (inferred by the % reduction in clear day solar radiation) in the upper slopes increases with elevation in summer, but in winter begins to decline at around 1200 m. In (4.2) it can be seen that net longwave loss depends of the reduction in solar radiation from clear-day values (a measure of cloud cover) squared. The effect of clouds to both decrease incoming solar radiation and longwave radiation loss tends to produce net radiation gradients over the study area. These gradients are less steep than the solar radiation gradients. Thus the exponential decrease in outgoing longwave radiation just offsets the more linear decrease in incoming solar radiation with elevation in summer. In winter, however, average cloud cover is less than in summer and decreases with elevation after about 1200 m. At higher elevations, net longwave loss is a higher fraction of outgoing longwave radiation than at sea level, as suggested by Figures 18 and 19 and by the

pressure correction term in (4.2). In other words, counterradiation decreases more quickly with elevation than does outgoing longwave radiation. This helps explain the apparent anomaly that above 1200 m solar radiation increases in winter while net radiation continues to decrease with elevation. It should be noted here that, due to the cosine effect, the Licor pyranometers record values about 5% higher than the true insolation receipt in winter (Ekern, personal communication). If this correction were incorporated into Figure 22, the winter ratios of net to solar radiation would be higher and would approach the summer values at the lowest elevations.

Extrapolating these results, one would expect the ratio of net to solar radiation to further decline with elevation above station 106. This is confirmed in measurements by Ekern (1965) who reported net to solar radiation ratios of 0.50 and 0.41 at Mauna Loa Observatory (3055 m elevation) on the island of Hawaii for clear days in June and December respectively.

Calculations reveal that, for individual days, the ratio of net to solar radiation varies with both the season and cloud cover. On clear days, according to (4.1) and (4.2), the ratio of net to solar radiation

varies from 66% to 58% (decreasing with elevation) in summer, and from 58% to 42% (also decreasing with elevation) in winter. Thus gradients are observed in both summer and winter. On cloudy days (1/2 average solar radiation), however, the ratio is more constant, being 74% to 76% in summer and 72% to 68% in winter. To generalize, it appears that, at a given site, the ratio of net to solar radiation increases with cloud cover. Also, for a given cloud cover amount, the ratio of net to solar radiation decreases with elevation.

The variation in net radiation help explain the evaporation distribution seen in Figure 11. Net radiation does not completely explain the evaporation rates observed in the winter field experiment, however. A residual amount, indicating alternate energy sources, is evident at all of the evaporation experiment sites. At all but the highest sites, this source of energy is probably positive heat advection. Advection will be the subject of the next chapter.

VI. ADVECTED ENERGY

A possible source of energy for evaporation not adequately considered in equations 4.3 through 4.7 is sensible heat advection. Sensible heat advection (horizontal transport of energy through the flow of air) occurs in non-homogeneous areas. This is particularly the case when sharp boundaries in surface conditions exist, such as the coastline of an island. Air moving onshore retains its oceanic character, that is, temperature and vapor pressure are controlled by the ocean surface. Surface air over land, however, is much more responsive to the radiation balance and vegetation characteristics.

Pan Evaporation Comparison Model

To determine the effect of advection on evaporation at low elevations, pan evaporation data from many stations around the state was compared with evaporation estimated by the Priestley-Taylor equation (4.6). Nullet (1987) gives preliminary results of this comparison. Deviations from the Priestley-Taylor model are assumed primarily due to an additional source of

energy for evaporation, advection. Similar approaches to isolating the effects of advection have been taken by Morton (1975), Brutsaert and Stricker (1979), and Singh and Taillefer (1986). A great deal of pan evaporation and solar radiation data have been collected in Hawaii, mostly by Hawaii sugar growers, and summaries of these data have recently been published by Ekern and Chang (1985) and How (1978). Pan evaporation values were standardized to the US Weather Bureau Class A pan by Ekern and Chang. The solar radiation data have been measured primarily by wig-wag integrators.

Net radiation is the primary forcing mechanism in (4.6) and was estimated using (4.1) and the original form of (4.2) given by Doorebos and Pruitt (1977). Air temperature was approximated by the formula:

$$Ta = 22 + 4\sin(16(Month-1)) \qquad (6.1)$$

where Ta is in ^{o}C and Month refers to the number of the month (January being 1 and December being 12). This formula was developed for this study based on average monthly air temperatures for Honolulu Airport. Elevation is not considered because virtually all of the pan evaporation stations are below 400 meters. A more exact formulation is not necessary because the net radiation formula is not particularly sensitive to air

temperature over the range found near sea level in Hawaii.

Stations with at least two years of concurrent measurements of solar radiation and evaporation were identified. This produced a list of 49 lowland sites, averaging over seven years concurrent measurements, to be used in the comparison and included stations on Hawaii, Maui, Oahu, and Kauai. Pan evaporation for these 49 sites was then compared with Priestley-Taylor evaporation modeled using monthly average net radiation (estimated from solar radiation as described above) and temperature. State key numbers for the 49 sites used are given in Appendix F.

Oceanic Sources

The results indicate a pattern of both positive advection (enhancing evaporation) and negative advection (suppressing evaporation). To illustrate this, advection is assumed to be responsible for differences between modeled and measured evaporation, i.e., the residual value. A pattern in the residual value (measured minus estimated evaporation) emerges when sites are ranked by differences in summer and winter residuals. To quantify the pattern, sites were ranked

by the sum of July, August, and September residuals minus the sum of January, February, and March residuals and plotted in Figure 23. In this figure, a second-order polynomial (a curve fitting equation of the form $y = a + bx + cx^2$) was fit through the ranked station's residual values for each month to enhance the visibility of the residual pattern. The lowest ranked station is closest to the viewer and the highest ranked is farthest away. The annual residual pattern for sample stations is shown Figure 24.

It became clear that the lowest ranked stations were predominantly windward, that is directly exposed to the onshore flow of oceanic air. This is quantified in Figure 25 in a diagram that shows the ranked stations plotted in polar coordinates with the radius being ten kilometers minus the distance of the site from the coast, and the azimuth corresponding to a direction from the nearest significant obstruction (mountain) blocking the prevailing air flow. Essentially, this figure represents the locations of stations on an "ideal island." It can be seen that 9 of the 10 lowest ranked sites are windward and the 10 highest ranked sites are all leeward locations.

The results of the comparison of modeled and

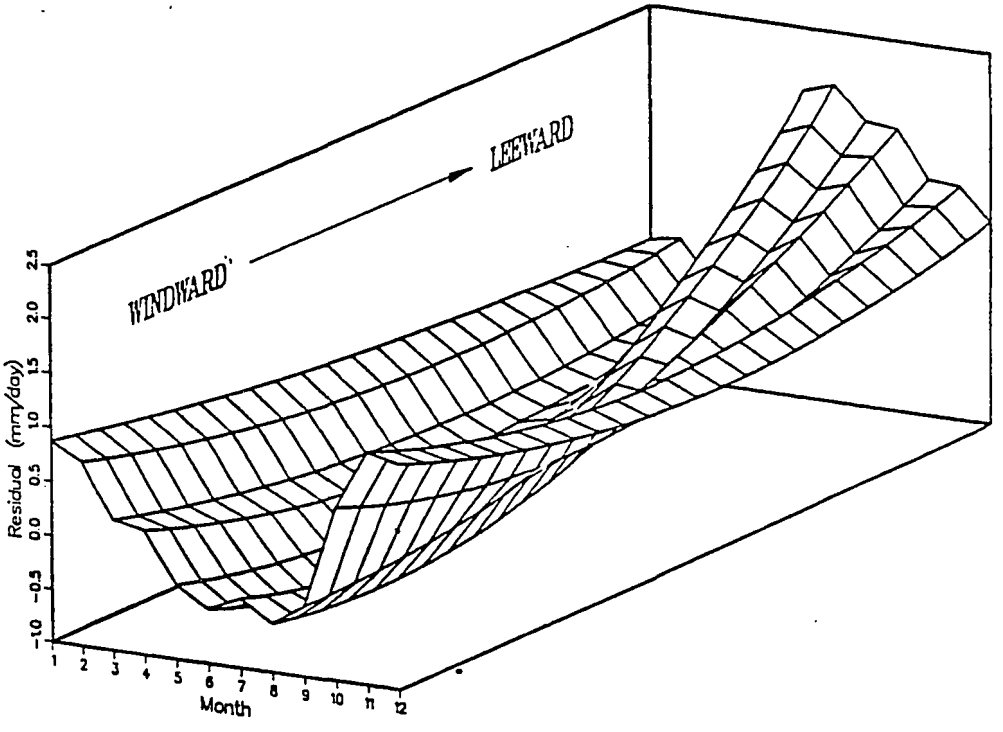

Figure 23. Advection pattern at pan evaporation sites

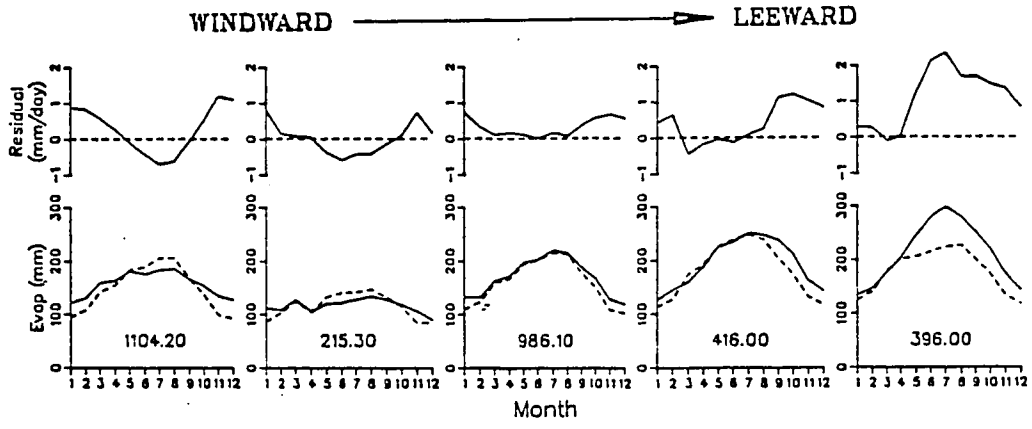

Figure 24. Sample estimated and pan evaporation comparisons

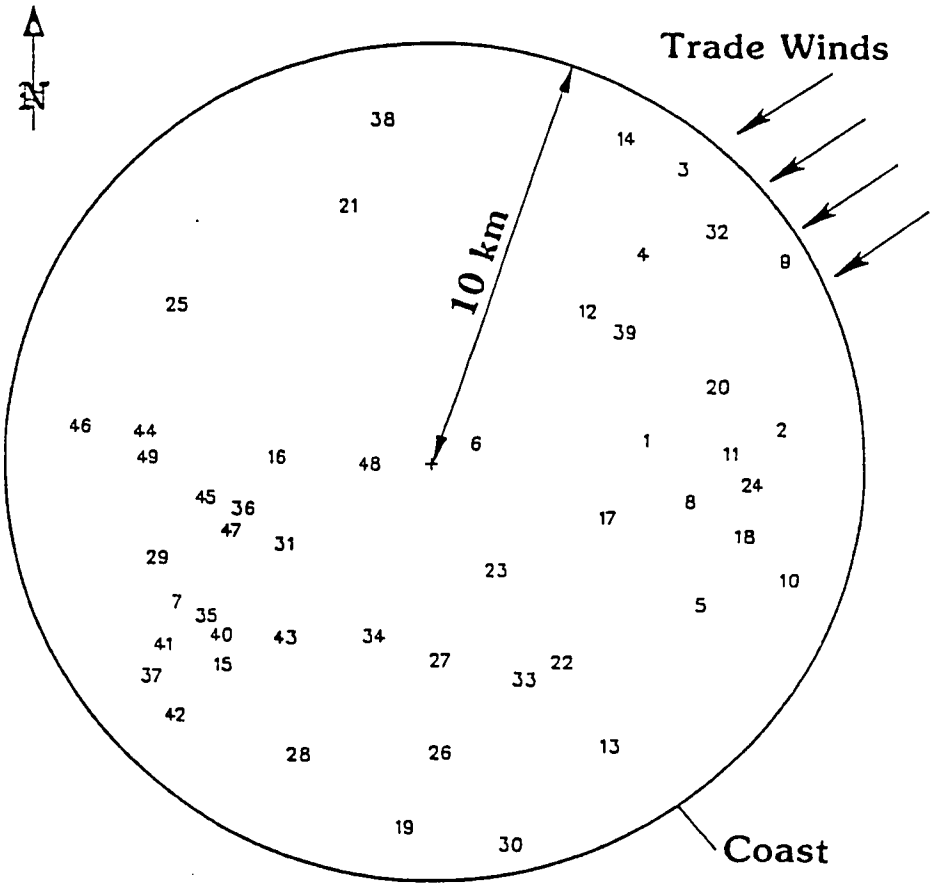

Figure 25. Pan evaporation station locations relative to nearest trade wind obstruction.

measured pan evaporation, illustrated in Figure 23, can be interpreted as follows. At sites with onshore wind flow, evaporation is enhanced in winter and suppressed in summer by advection of sensible heat from the surrounding ocean. The mechanism that dampens the annual air temperature wave in the Hawaiian Islands also appears to dampen the evaporation cycle. This mechanism is the enormous thermal inertia of the surrounding ocean which limits the average monthly ocean surface temperature range over the course of the year to just 2.5°C. Over land, the annual surface air temperature range is about twice this and in the absence of an oceanic influence would be far greater.

The near-surface atmospheric profile in equilibrium with the ocean surface encounters a sharp discontinuity as it moves over land with onshore air flow. The process of adjusting to the new moisture and temperature characteristics of the land surface involves sensible and latent heat exchanges between the surface and near-surface atmosphere. The net flow of energy can be either toward the surface, resulting in evaporation enhancement if sufficient moisture is available, or away from the surface, which will tend to warm the overlaying air at the expense of evaporation from the surface.

The approximate onshore flow of advected sensible heat can be calculated from the bulk transfer equation,

$$A = \rho C_p (T_x) u \qquad (6.2)$$

where A is heat advection, ρ is the density of air, c_p is the specific heat of air at constant pressure, T_x is the difference in temperature over a surface due to advection, and u is the horizontal wind speed. Schroeder (1980: pg. 30) reported an approximately $2^{o}C$ temperature suppression by cloud and onshore advection of sensible heat on 28 June 1978 near Anoehoomalu on the island of Hawaii. Assuming that advection accounted for approximately one half of this cooling, the approximate advected sensible heat can be calculated from (6.2). Letting $T_x=1^{o}C$, $\rho=1.27$ kg m^{-3}, $c_p=1004$ J kg^{-1} $^{o}C^{-1}$, and $u=10$ m s^{-1}, and substituting these values into (6.1) yields horizontal advection of 13 KJ m^{-2} s^{-1} through a plane perpendicular to the surface and parallel with the coastline.

It appears then, that the ocean, already well known to moderate island temperatures, moderates evaporation as well. An idea of the magnitude of the oceanic influence is shown in Figure 26. Here the average residual value (measured minus estimated evaporation) for the twenty lowest ranked sites is plotted for each

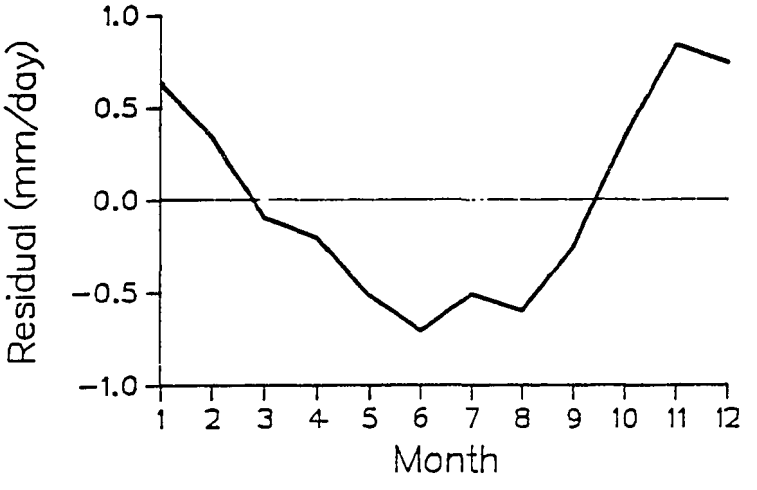

Figure 26. Advection pattern at windward sites

month. The resulting curve clearly illustrates the annual pattern of oceanic advection. The average residuals fluctuate between a maximum of +0.84 mm in November and -0.71 mm in June.

To corroborate the suggestion that positive heat advection from ocean sources exists, one could infer that in winter air temperatures over land were cooler than at the same elevation in the free atmosphere and vice versa in summer. This would indicate a sensible heat gradient and imply heat flow toward land in winter and away in winter. That this is indeed the case is illustrated later in Figure 33. This figure shows land temperatures at the MauiNet sites minus free atmosphere temperatures at the same altitude from the Hilo rawinsonde profiles. In winter the free atmosphere is warmer, and in summer, cooler. This implies that, on average, Maui is a heat sink in winter and a heat source in summer.

Land Sources

Actually, the influence of oceanic sensible heat advection may be ubiquitous at lowland sites, but is obscured by regular pattern of positive heat advection in summer at dry leeward locations. Land areas can

become a source of heat advection when insufficient surface moisture exists to meet the atmospheric demand. Radiative energy that normally would have been converted to latent heat in the evaporation process, thus is absorbed by the surface and is converted to sensible heat. This sensible heat energy dissipates into the surface air layer by the same turbulent diffusion processes as water vapor and is carried in the moving air stream. Although the fetch on the Hawaiian Islands is generally short, heating of dry land areas in the vicinity of evaporation stations has greatly increased measured evaporation. Advection of heat from dry land areas in summer can far exceed the oceanic advection. For example, the highest positive residual in the pan evaporation comparison with modeled evaporation was +2.8 mm for station 396.00 in the Maui saddle in June.

It is difficult to generalize the magnitude of land advection sources because of the heterogeneous nature of the land surface, although clearly advection from land sources will be higher in areas of low rainfall (see Figure 5). By contrast to the homogeneous surrounding ocean, the land surface may include such diverse terrain as dry lava rock, rain forest, and desert scrub. Complicating this mottled pattern the is irrigation of

agricultural areas in otherwise dry environments such as the Maui saddle and west Kauai.

Distribution

The December value of oceanic advection of about +0.7 mm (Figure 26) is quite close to the residual between measured winter evaporation at the near-coastal site 114 (see Figure 5) and modeled evaporation values (Table 1). It appears, then, that the discrepancy between modeled and measured evaporation for the winter observations at the coastal site can be explained in terms of onshore advection of oceanic air. It can be seen that the residual value at the two higher elevation sites, stations 115 and 116, on this transect is only half of the coastal site value. This implies either that the effect of onshore advection diminished with increasing fetch over land or that the advection potential diminishes with altitude in the free atmosphere. That wet inland sites are relatively advection-free has been suggested elsewhere by Ekern (1983) who found that the Priestley-Taylor equation provided accurate estimates of evaporation on a transect into high rainfall areas in the lee of the Koolau mountains on Oahu.

On the dry transect, the effect of advection appears slightly greater. This can, perhaps, be attributed to advection from land sources. This possibility is illustrated by comparing temperature profiles (during the winter field trip) for the two transects in Figure 27. This figure shows that the air temperature at station 117 is about 0.5°C higher than a comparable elevation on the wet transect and at station 119 is about 0.3°C warmer. The warmer air implies an additional heat source. Heating of the surrounding dry land is one possibility, another is condensation and subsequent adiabatic heating as the air flows over the northwest ridge of Haleakala. At the highest site, station 106, measured evaporation is twice the value estimated using the Priestley-Taylor equation (4.6). This suggests a significant additional energy source for evaporation not present, or at least not as important, at the other sites. This evaporation enhancement at high elevations is investigated in the next chapter.

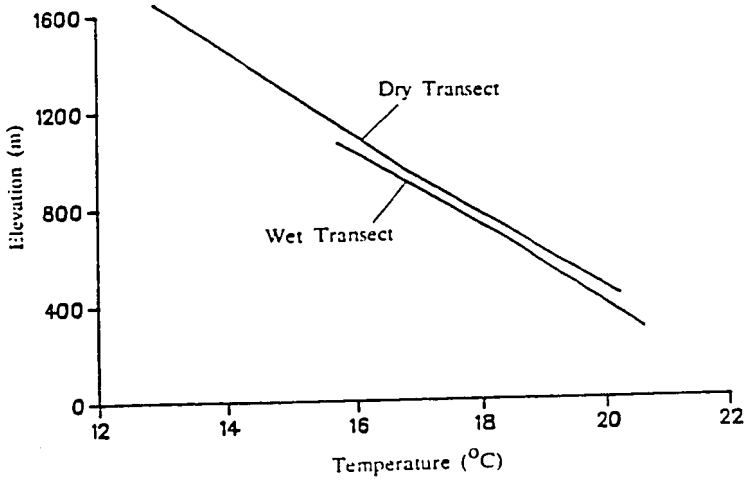

Figure 27. Air temperature profiles at winter evaporation experiment sites

VII. HIGH ELEVATION EFFECTS

Higher elevations in the mountains of Hawaii feature a climatic regime that is distinctly different than the sea level climate. (For reference, high elevations in the context of this study refers to elevations above about 1200 meters.) Besides predictable changes from sea level, such as decreasing air temperature and pressure with elevation, the presence of an inversion layer profoundly influences the climate on the upper slopes of the mountains. It can suppress vertical motion, thus reducing cloudiness. Radiative fluxes increase under the resulting clear skies, and rainfall decreases. Also, the large scale subsidence associated with the inversion causes a drying of the air and consequent reduction in absolute humidity. Turbulent and mechanical mixing of air through the inversion can extend this drying influence to below the inversion layer. Finally, it should be noted that the land area at high elevations is very small. For horizontally moving air, fetch distances are correspondingly small making it virtually impossible to establish an equilibrium atmospheric profile over land

areas. This suggests that the climate over land is probably more strongly influenced by the free atmosphere at high elevations than at inland areas near sea level.

To explore unique climatic influences on the evaporation rate at the higher elevations, evaporation measurements from a transect through the approximate altitude of the inversion are analyzed. These data were collected in the summer, 1988, experiment on Haleakala which was discussed in Chapter IV. This analysis is followed by a brief examination of the effect of decreasing air pressure on three evaporation models.

Evaporation Transect

As discussed in Chapter IV, a transect of three stations between 945 to 2100 meters was maintained in the summer of 1988. Average values for the measured climatic elements and a comparison with estimated evaporation by several models was given in Table 3. To isolate non-radiative influences on the evaporation rate, measured evaporation is compared with estimates by the Penman equation (2.17) and (4.3). This comparison, as well as a comparison with net radiation and the night evaporation rate (between midnight and 6am), is shown in Table 6.

TABLE 6. High elevation effects on evaporation

Sta.	Elev. (m)	Evap. (mm)	E_p (mm)	Evap-E_p (mm)	E_{nr} (mm)	Evap/E_{nr} (%)	E_n (mm/hr)
119	945	3.3	3.3	0.0	4.4	75	0.025
106	1650	3.6	3.2	0.4	3.6	100	0.073
151	2130	6.4	5.2	1.2	6.0	107	0.105

E_p is evaporation estimated by the Penman model
E_{nr} is the latent heat equivalent of Q^*
E_n is the night evaporation rate

The residual value (Evap-E_p) shown in Table 6 clearly increases with elevation, even though the Penman equation, unlike the Priestley-Taylor equation, incorporates a measure of the influence of the vapor pressure deficit. Also, the high ratios of evaporation to net radiation at the two highest stations strongly suggests an energy source for evaporation besides net radiation exists and that this energy source increases with elevation over the range of the transect. In other words, if all of the available net radiation were absorbed in evaporation, it would still be less than the measured evaporation rate. For example, the latent heat equivalent at station 151 is 6.0 mm (14.8 MJ m^{-2} / 2.47 MJ m^{-2} per mm) while measured evaporation is 6.4 mm. It can be noted here that evaporation measurements taken since the summer of 1988, given in Appendicies G and H,

support the comparison given in Table 6 except for station 151, where the accuracy of the more recent measurements is suspect.

An examination of the diurnal pattern of evaporation, and of the other measured data, provides further evidence of the additional energy necessary to account for the residual evaporation shown in Table 6. Figures 28 through 32 illustrate the average diurnal pattern of evaporation, net radiation, air temperature, vapor pressure deficit, and wind. Figure 28 clearly shows night evaporation at the sites and further shows that the night evaporation rate increases with elevation. The average value of the night evaporation rate is shown in Table 6. Energy for night evaporation is obviously non-radiative (Q^* is usually negative at night). It is possible that the night evaporation rate continues throughout the 24-hour period and overlays the diurnal evaporation pattern imposed by high daytime net radiation.

It also appears that the night evaporation rate is related to the vapor pressure deficit (the theoretical saturation vapor pressure at the ambient air temperature minus the actual vapor pressure of the air). As Figure 31 shows, the vapor pressure remains high throughout the

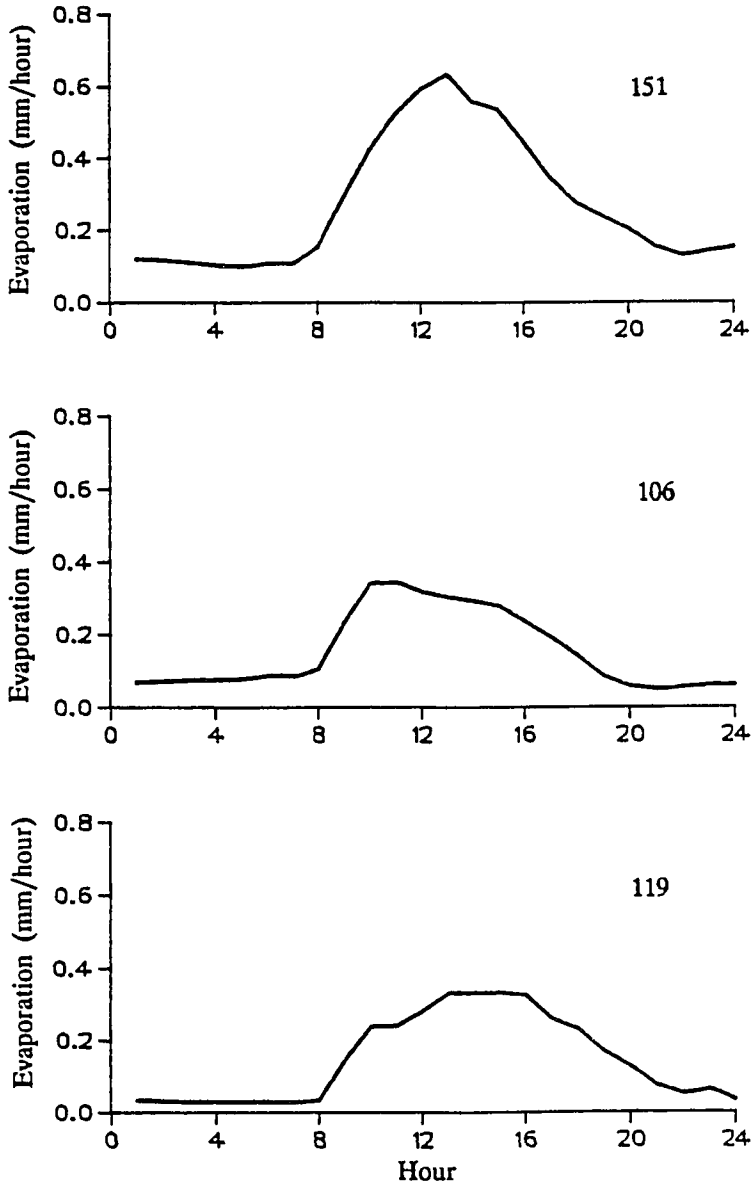

Figure 28. Diurnal evaporation pattern (summer)

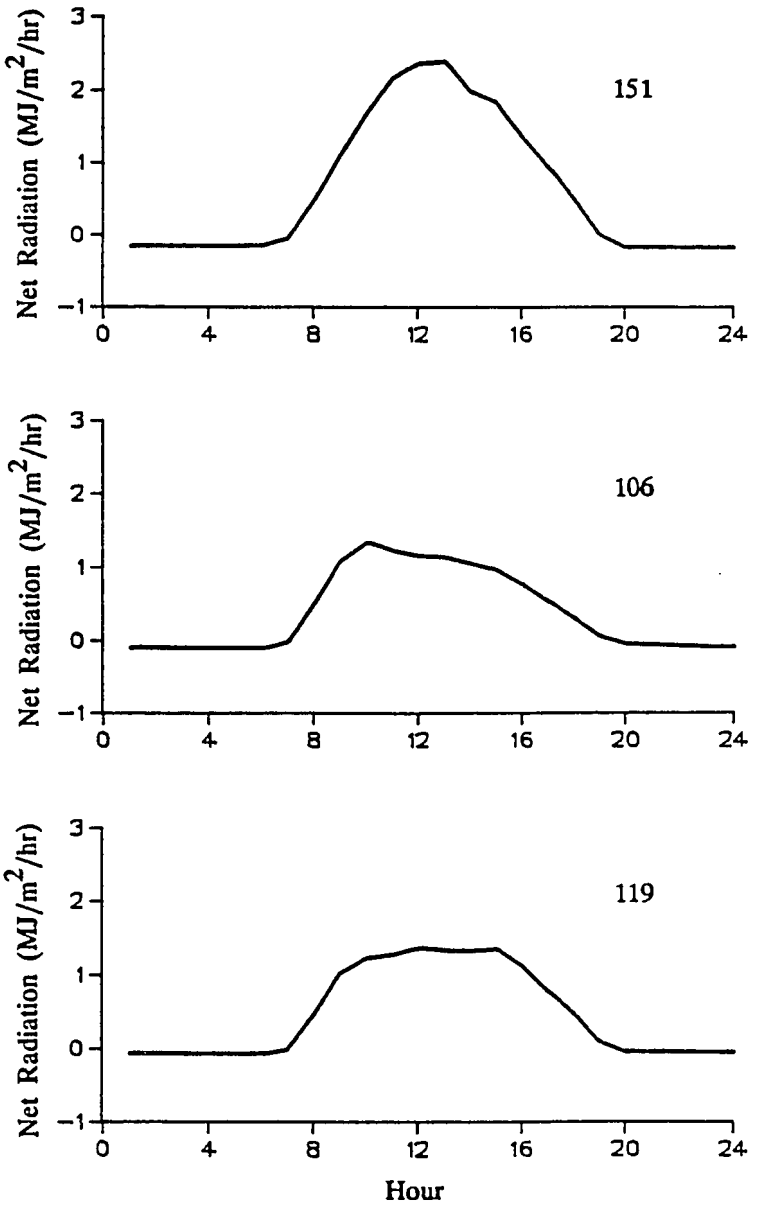

Figure 29. Diurnal net radiation pattern (summer)

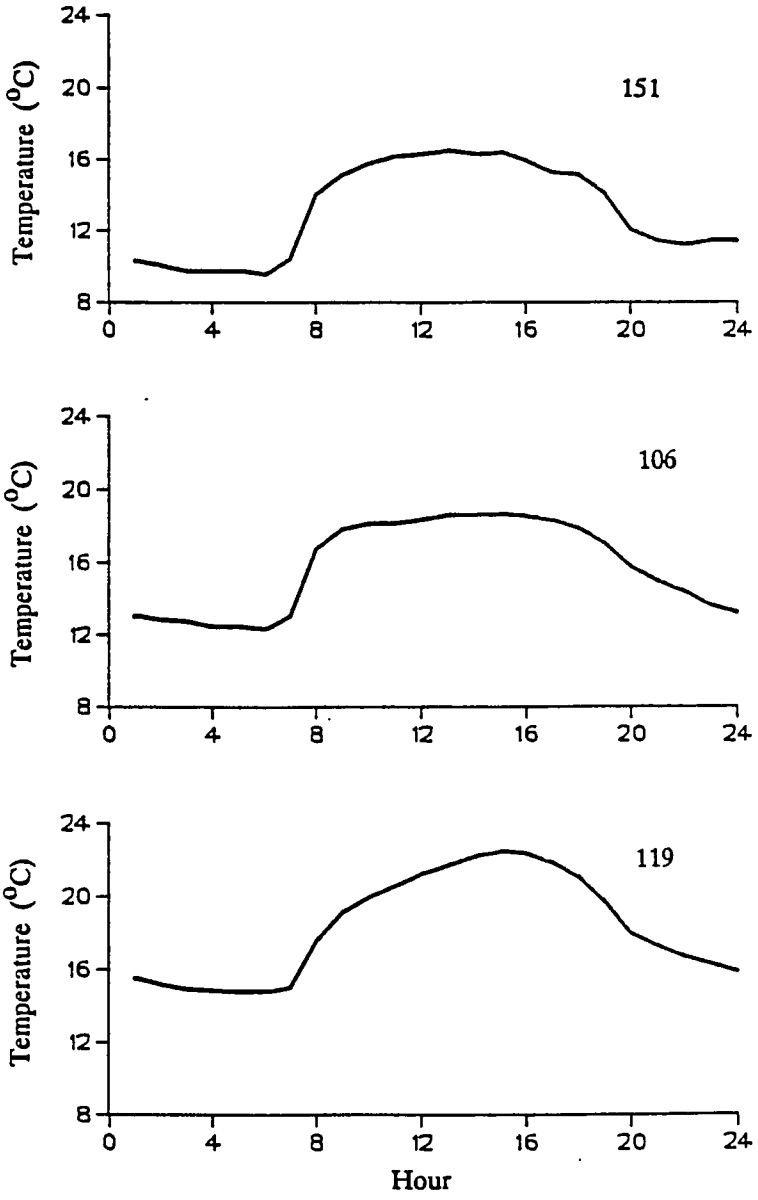

Figure 30. Diurnal air temperature pattern (summer)

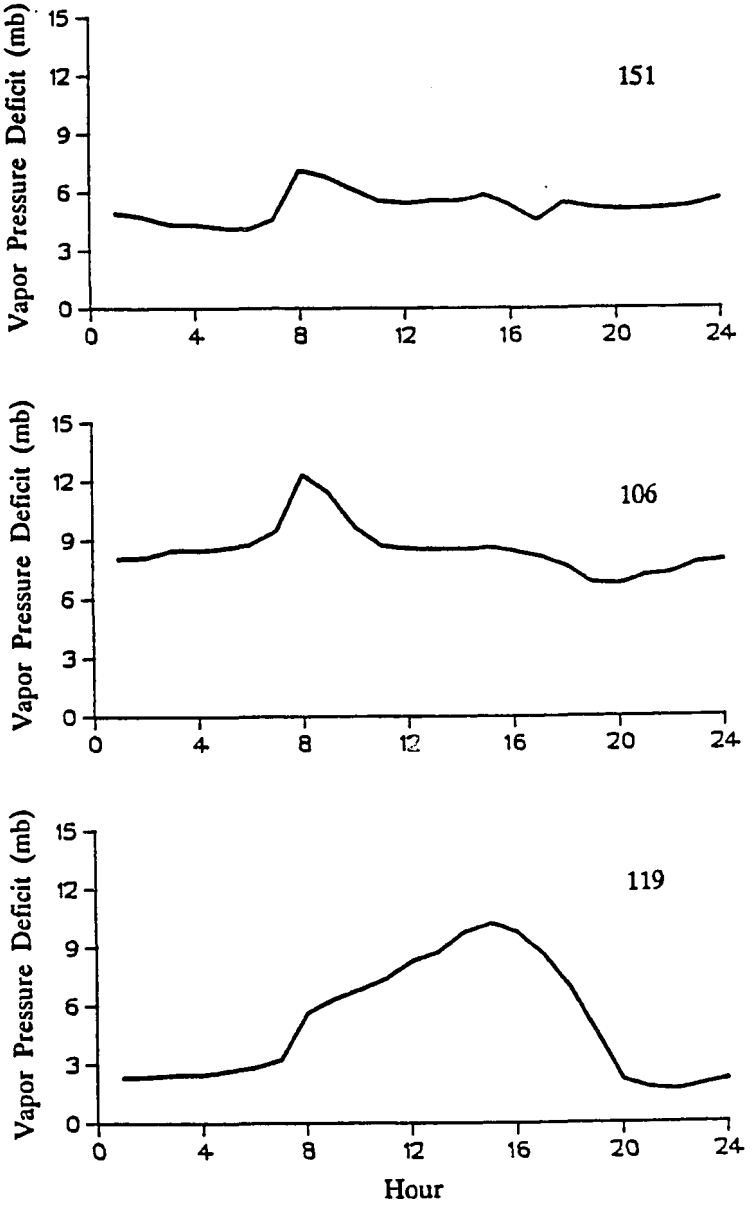

Figure 31. Diurnal vapor pressure deficit pattern (summer)

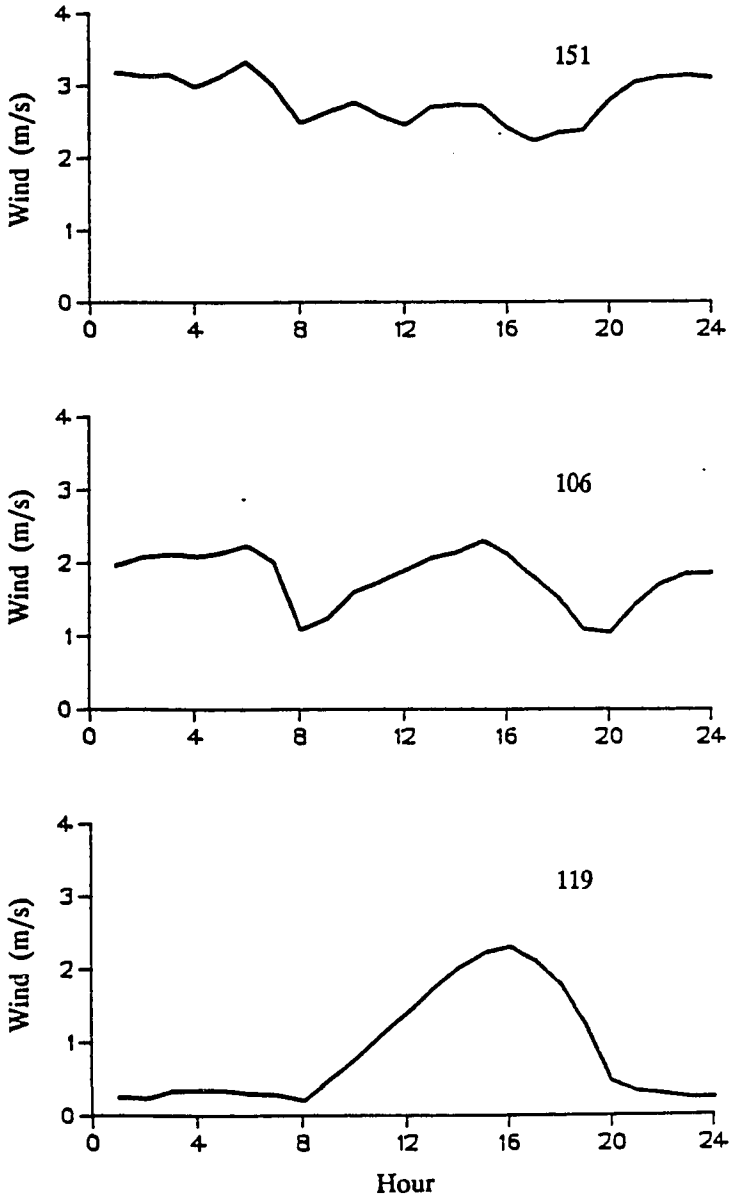

Figure 32. Diurnal wind speed pattern (summer)

night at the higher elevation sites, but falls dramatically at night at the lowest station. Interestingly, the correlation between daily evaporation and vapor pressure deficit increases with elevation, rising from 0.43 at Station 119, 0.81 to Station 106, to 0.86 at Station 151. The additional energy source for evaporation suggested in Table 6, then, appears to affect the evaporation rate in part by helping maintain a high vapor pressure deficit throughout the nighttime.

According to (2.6), the major source in the energy balance equation besides net radiation is sensible heat advection. At high elevations, the source of sensible heat advection can be neither the land or the ocean surface, which were discussed in Chapter VI. That the advection source is not daytime heating of dry land surfaces is suggested by the observation of nighttime evaporation. That the ocean is not the advection source is suggested in the diminishing effect of oceanic advection with distance inland discussed in Chapter VI. The source of advected sensible heat at high elevations must therefore be found in motions of the free atmosphere itself.

The above observations and discussion are interpreted as follows: The increase in the influence

of advected sensible heat on the evaporation rate with elevation is related to the large-scale subsidence prevalent over the Hawaiian Islands region. This subsidence adiabatically warms the air and reduces the humidity at altitudes near and above the inversion. The transect described in Chapter IV begins at 945 meters elevation, well below the trade wind inversion, and rises to 2130 meters, near the mean position of the inversion. The downward mixing of warm, dry air through the inversion both warms the near surface air and maintains a strong vapor pressure deficit throughout the 24-hour period at the highest stations, 106 and 151.

The net result of the downward mixing of air through the inversion is to substantially increase the evaporation rate at high elevations. For example, at station 106 this effect accounted for 19% of measured evaporation for the summer experiment (Table 3) and fully 50% of measured evaporation during the winter experiment (Table 1), assuming that the Priestley-Taylor equation (4.6) provides baseline evaporation estimates under advection-free conditions. In contrast to advection from oceanic sources, which enhances evaporation in winter but suppresses in summer, advection at high elevations enhances evaporation

throughout the year. This suggests that evaporation gradients between sea level and high elevations are sharper in summer than winter.

None of the common evaporation models described in Chapter IV, even those with an aerodynamic term, adequately accounts for advection at high elevations. This corresponds with the findings of Chapter VI where the models failed to account for the effect of advection from either land or ocean surfaces. Finally, although it seems reasonable to assume that the drying effect of subsiding air at high elevations should be related to inversion height and strength, no correlation was found between measured night evaporation at Station 106 and either inversion height or strength based on the summer evaporation measurements.

Atmospheric Pressure

A study of the effect of changing air pressure on the evaporation rate was not a principal goal of this project. Controlling the various environmental parameters to focus on the effect of atmospheric pressure would not be possible; temperature differences between elevations are inherent, for example. However, it is interesting to examine the effect of pressure on

various evaporation models. This may provide some insight into the actual environmental influence.

At the turn of the century, atmospheric pressure was considered one of the most important variables in determining the evaporation rate (Livingston, 1909). This followed from a consideration of molecular diffusion into a calm atmosphere (2.3). Considering only molecular diffusion then, an increase in elevation means a decrease in pressure and a corresponding linear increase in the evaporation rate. For example, moving from sea level to 500 mb would double the evaporation rate.

Horton (1934) pointed out that the atmosphere is seldom calm and thus turbulent mass transfer processes must be considered. He argued that the evaporation rate would only increase slightly, if at all, with elevation because "the reduction in barometric pressure cannot increase and may somewhat decrease the rate of vapor removal by mechanical action of the wind." A detailed study of the relation between p and E was carried out by Rohwer (1931). Using the Dalton style formula,

$$E = (0.44 + 0.118u)(e_s - e_a) \qquad (7.1)$$

where u was in average miles per hour at surface level and e was in inches of Hg, he compared measured and

estimated evaporation from small open-water evaporimeters at sites between sea level and 4300 meters. He concluded that evaporation increased with decreasing p and recommended multiplying (7.1) by the following correction, (1.465 - 0.0186p), where p was given in inches of mercury. The formula is constructed to give a correction of 1.00 at the elevation of Fort Collins, Colorado, 1500 meters. Unfortunately, Rohwer could not control for differences in net radiation and his conclusions must therefore be suspect.

Perhaps the most common modern formula that includes some consideration of atmospheric pressure is the Penman equation and its derivatives through its inclusion of the psychrometric constant, γ. Storr and den Hartog (1975) reminded the scientific community that γ was directly related to p by,

$$\gamma = c_p p / 0.622 \lambda \qquad (7.2)$$

For high elevation locations the implications are obvious. A reduction in in (2.17) means a higher fraction of Q^* is used in evaporation, while dependence on aerodynamic influences is reduced. Interestingly, this conclusion is opposite that of Chang (1985) obtained by studying pan evaporation measurements. Another modern evaporation model that contains a

pressure dependence is Brutsaert's bluff roughness evaporation equation (2.48). In (2.48) the evaporation rate is a function of the quotient of the powers of the molecular diffusivity and kinetic viscosity of air. Thus, Penman's equation considers the thermodynamic consequences of changing pressure, while (2.48) considers turbulent transfer.

The effect of varying pressure using the Penman formula, (2.17) and (4.3), Priestley-Taylor formula (4.6), and Brutsaert's formula (2.48) are illustrated in Table 7. The sample values were chosen to approximate average conditions for sea level, 900 mb, and 800 mb using Figures 12, 16, and 17.

TABLE 7. Evaporation (mm/day) and air pressure

	Priestley-Taylor			Penman			Brutsaert		
p (mb)	T (^{o}C)			T (^{o}C)			T (^{o}C)		
	24	16	8	24	16	8	24	16	8
1000	4.5	3.9	3.2	5.1	3.8	3.8	1.2	1.0	0.9
900	4.6	4.0	3.4	5.1	3.9	3.8	1.2	1.1	0.9
800	4.7	4.2	3.5	5.1	4.0	3.9	1.3	1.1	0.9

(Q^{*}=12 MJ/m^{2}, e_{a}=T_{a}, wind=5 m/s)

Table 7 shows little response to air pressure for the various models for the range of atmospheric pressure over the study area. It appears, then, that changing pressure has only a slight effect on the evaporation rate as compared to the other climatic variables.

In summary, decreasing air pressure has only a slight effect on the evaporation rate while downward mixing of dry air through the inversion appears to exert a considerable influence on the evaporation rate at high elevations. This advection source accounts for the large residual value between measured and modeled evaporation at station 106 (Figure 11) and for the increase in night evaporation with elevation seen in Figure 28. This high elevation advection source, fundamentally related to the large scale subsidence over the Hawaiian Islands, also accounts for the reversal in the evaporation gradient at high elevations seen in Figure 11 and in Table 3. Presumably, this influence increases with elevation above our highest station at 2100 meters.

VIII. MODELING EVAPORATION

In this chapter, I suggest an approach to modeling the spatial distribution of evaporative demand on tropical high islands based primarily on the analysis presented in the previous chapters. The importance and application of accurate evaporation estimates has been discussed in Chapter I. The discussion in this chapter is intended to provide a conceptual framework for a future modeling exercise but omits many important details, i.e. the suggested model is not actually put into practice here.

The suggested procedure involves making baseline estimates of PE using the Priestley-Taylor equation and then modifying the results by adding advection terms. This can be written as:

$$PE = PE_{pt} + PE_o + PE_l + PE_s \qquad (8.1)$$

where PE_{pt} is PE calculated by (4.6), PE_o, PE_l, and PE_s are the influences of advection from ocean, land, and synoptic scale subsidence respectively on PE. The Priestley-Taylor equation is chosen to provide baseline estimates of PE because of its relative simplicity, because, as shown in Chapter IV, it provides comparable

estimates to other models tested, and because it provides reasonable estimates of PE in advection free conditions in Hawaii. The Priestley-Taylor formula basically relies on temperature and net radiation data. An estimate of vapor pressure is used in calculating net radiation. The first step, then, is to estimate the distribution of these variables.

Temperature and Vapor Pressure

Temperature and vapor pressure near the surface on tropical island mountains can be estimated using atmospheric profiles obtained from nearby rawinsonde stations. To illustrate the viability of this method, temperatures and vapor pressures at study site stations are compared with temperatures and vapor pressures in the free atmosphere at equal altitudes. The rawinsonde data are from Hilo, 160 kilometers to the southwest of the study area. The small horizontal climate gradients found over tropical oceans suggest that the distance to the sounding station is not considered excessive. For example, the temperature difference between the Hilo soundings and those taken from Lihue (330 kilometers to the northwest of the study area) averages $+0.3^{\circ}C$ (Hilo warmer) in winter and $-0.1^{\circ}C$ (Hilo cooler) in summer

between the 1000 and 850 mb levels, the range of the study area, based on 1984 through 1986 data. The average soundings do not differ by more than $\pm 0.5^{\circ}C$ during either season between the 1000 and 600 mb levels.

Mountain surface minus free atmosphere temperature departures are shown in Figure 33. Actual near-surface air temperature values were shown in Figure 16. In general, climatic average air temperatures near the mountain are lower than free atmosphere temperatures in winter and warmer than the free atmosphere in summer. This implies that the mountain is, on the daily average, a heat sink to the atmosphere in winter and a heat source in summer. In summer a slight horizontal temperature gradient is evident. This is equal to 1.4° C between stations 109 and 102, for example. Similar horizontal gradients are not clearly discernable in the winter temperature map. The lapse rate, based on surface observations, is about $6^{\circ}C$ per kilometer.

Departures from the free atmosphere vapor pressure are shown in Figure 34. In winter, departures above 900 meters are all negative, while below that level departures are generally positive. In summer, departures are all positive, being on the order of 1 mb higher than the positive winter departures. This is

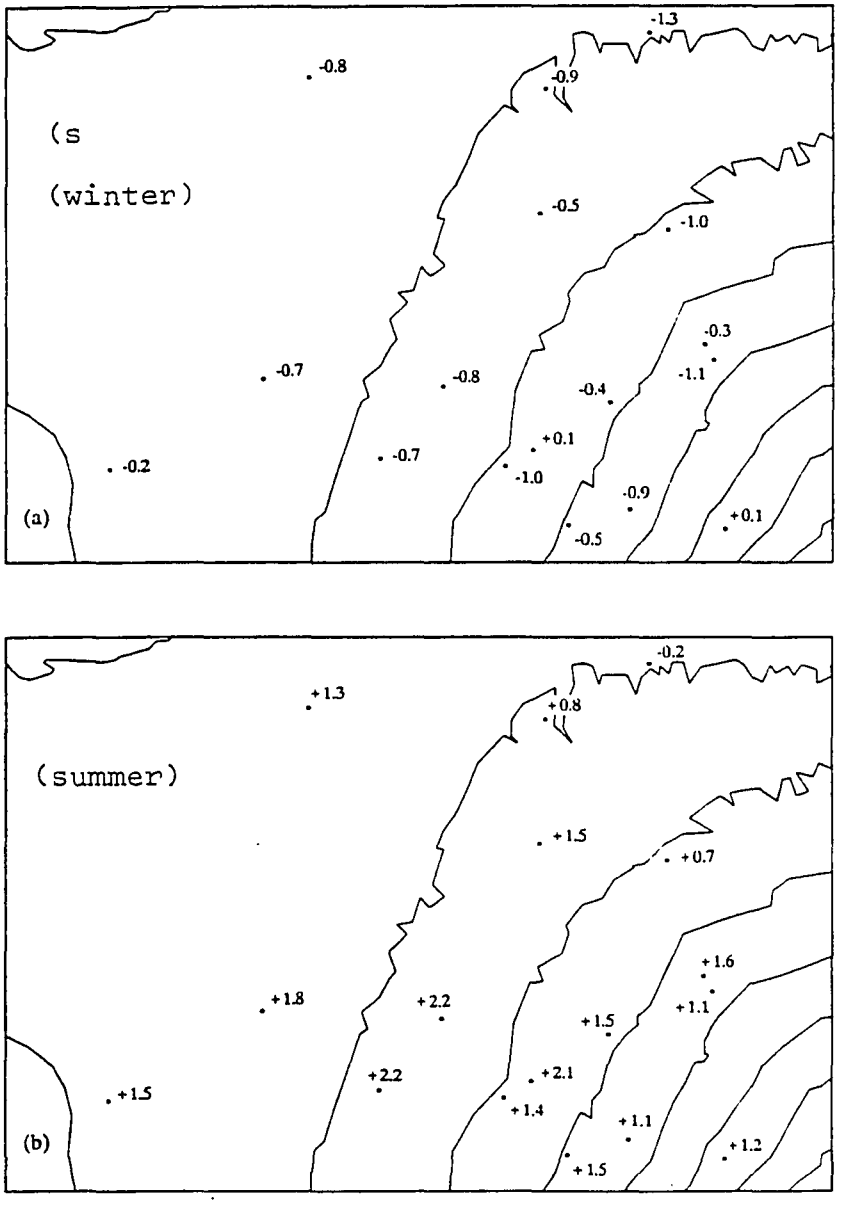

Figure 33. Seasonal average mountain minus free atmosphere air temperature (°C)

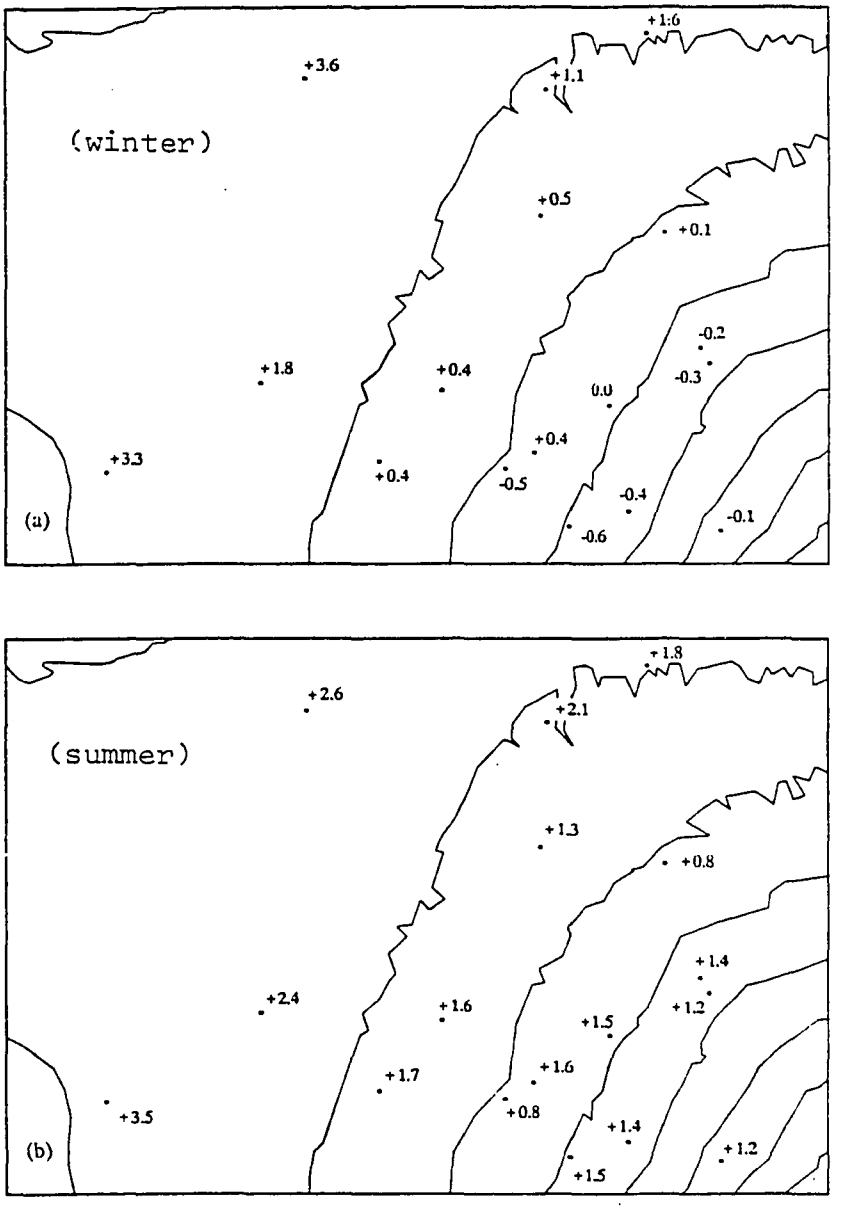

Figure 34. Seasonal average mountain minus free atmosphere vapor pressure (mb)

consistent with a surface water vapor source. That vapor pressure departures are not generally negative, suggests that condensation on the mountain surface originates primarily from ground rather than atmospheric sources. Below 300 meters, large positive departures from the free atmosphere are evident. This may be an artifact of the location of the rawinsonde station, Hilo, which is subject to diurnal thermal circulations.

Above 300 meters, the vapor pressure over land is within 1 mb of the free atmosphere vapor pressure in winter, and could possibly be equivalent. This is probably as accurate a statement as possible considering the problems with the measured relative humidity data and the fact that vapor pressure has been estimated using average daily temperature and humidity. In light of these considerations, the concordance with the vapor pressure in the free atmosphere seems remarkably consistent. The slightly higher departures in summer, about 1 to 2 mb, may reflect higher evaporation from land in the high solar radiation summer period.

For most applications, applying the free atmosphere value of vapor pressure (and relative humidity) and temperature to the mountain side would be adequate. In the case of Hawaii, a correction ranging from about

+0.5°C in winter to -1.5°C in summer could be applied to the free atmosphere temperature values. The horizontal gradient seen in summer may be due in part to subsidence heating in the lee of the northwest ridge of Haleakala, as well as warming as the air moves over land. This gradient could be modeled in part using a numerical air flow model such as that tested for Oahu by Lavoie (1972). Lavoie's model predicted a horizontal potential temperature gradient of about 1°C between Oahu's windward and leeward shores under typical summer trade wind conditions.

Net Radiation

Net radiation can be estimated using (4.1). As shown in Chapter IV, net radiation can be estimated fairly accurately if global radiation is known. To model global radiation, clear day baseline values must be calculated for each elevation on the mountain and then reduced according to a cloud index. The SPCTRAL2 model (Bird and Riordan, 1986), used in Chapter V, has proven to be accurate for modeling clear day values in Hawaii (Nullet and Ekern, 1988a). The range of clear-day global radiation totals over the study area is illustrated in Figure 14. Clear-day values at the

higher elevation are about 7% higher than sea level values.

In the Hawaiian Islands region, solar radiation over the open ocean is approximately 80% of the clear day value (Nullet, 1988). As seen in Figure 15, this is approximately the highest value in both summer and winter at the lowest elevations of the study site. Further attenuation from this value is due to the presence of clouds formed through the influence of the island on the airflow, primarily though thermal circulations and orographic forcing. Reductions in solar radiation due to these influences could be based on a cloud index derived from a coupled topographic forcing wind flow model, such as Lavoie's (1972), and a sea breeze model. The maximum depletion of clear-day solar radiation was 49% at the highest elevation station in summer (see Figure 15), and thus the cloud index would have to account only for reductions between about 20% and 50% of the modeled clear-day values. An alternative method of modeling the attenuation of solar radiation by clouds would be to map the distribution of clouds over the mountain using satellite images, such as GOES (Geosynchronous Orbiting Earth Satellite) images. Clear-day values could then be reduced to average

monthly global radiation using a model derived from a comparison of measured insolation at the MauiNet sites and the average cloud distribution.

Once an estimate of global radiation has been made, net radiation can then be computed from (4.1) and (4.2). As discussed in Chapter IV, an albedo value of 0.19 is suggested and ρ, a exponent that accounts for the effect of clouds on longwave radiation, is 2.0.

Advection

Advection was discussed in Chapters VI and VII. This includes the contributions of advection from land and oceanic sources, and from the downward mixing of dry air through the inversion. A simple correction for oceanic advection would be to add the residuals (measured minus modeled evaporation for leeward pan evaporation sites) shown in Figure 26 to the Priestley-Taylor estimates for near-coastal stations. For the months of January through December respectively these values are: 0.63, 0.34, -0.10, -0.21, -0.52, -0.71, -0.51, -0.60, -0.25, 0.34, 0.84, and 0.74. Further study is needed to determine how the effect of oceanic advection declines with distance from the coast. For example, as seen in Figure 11, the inland residual

values at Stations 115 and 116 are much lower than the residual value and the near-coastal site, 114. Modeling advection from land sources is a more difficult matter and could best be accomplished by the use of a water-balance model to predict the dryness of the soil and then possibly use the Bowen ratio as an index of advection potential. This index could be compared to the summer residual values found for leeward sites in Figure 23 to develop a suitable model for estimating the potential for advection from dry land surfaces to increase the evaporation rate.

A simple index for the additional evaporation evident at high elevations discussed in Chapter VII would be the height and strength (temperature increase) of the inversion. Figures 35 and 36 show scattergraphs of the night evaporation rate (evaporation between midnight and 6 am which was shown to increase with elevation between 945 and 2130 meters) at Station 106 and the inversion height and strength. The inversion data are taken from the noon GMT sounding at Hilo. Unfortunately, as shown in Figures 35 and 36, neither inversion height or strength seems to be closely related to night evaporation for the range of conditions found during the summer experiment. It appears that an

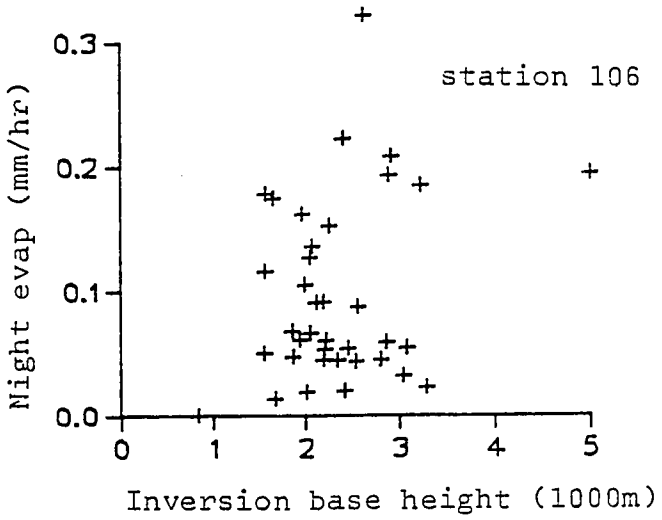

Figure 35. Evaporation and inversion height comparison

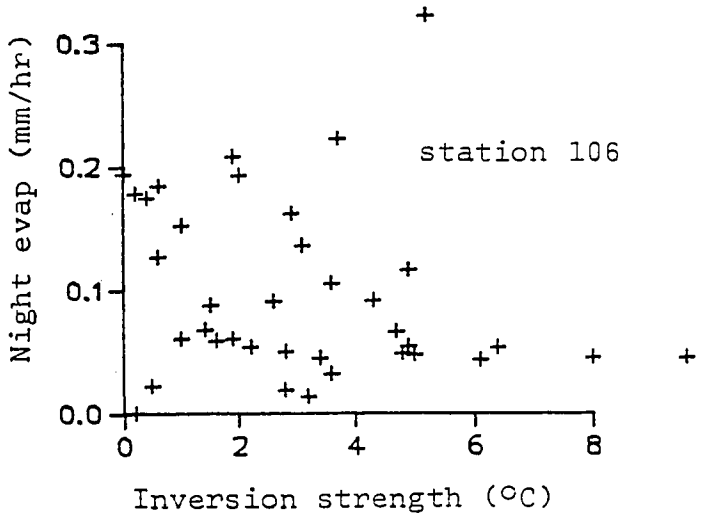

Figure 36. Evaporation and inversion strength comparison

empirical model would have to be developed that related evaporation enhancement to both elevation and season. Compiling the data necessary to develop this empirical model would require at least a year of measurements on a transect that includes stations 119, 106, 151, and perhaps a new station at the summit of the mountain. The annual pattern might be related to annual changes in the average free-atmosphere vapor pressure deficit, determined by rawinsonde data.

IX. CONCLUSIONS

Summary

The primary aims of the study were first, to identify and explain variation in potential evaporation at different elevations and different exposures on tropical high islands, and second, to provide reference data for modeling evaporation and suggest how an evaporation model appropriate for tropical high islands might be developed.

To accomplish these goals, new and existing data were analyzed to study climatic influences on the evaporation rate in the Hawaiian Islands, particularly on the 3055 meter elevation mountain, Haleakala, Maui. Existing data included measurements from 17 MauiNet climate stations on Haleakala, from pan evaporation and solar radiation stations around the state of Hawaii, and rawinsonde data from Hilo Airport. New data included Ekern evaporimeter measurements from a network of 6 stations at MauiNet sites in the winter of 1987-1988, recording evaporimeter measurements from a transect of 3 sites between 945 and 2130 meters in the lee of Haleakala in the summer and fall of 1988, and

supplemental wind and net radiation measurements at some of the evaporimeter stations.

These data were analyzed to identify and explain the distribution of radiant energy, the major source of energy for evaporation, and to quantify the contribution of sensible heat advection in determining the evaporation rate. Land, ocean, and synoptic scale subsidence all proved to be significant sources of advected energy.

Net radiation, the primary control on the evaporation rate, varies according to the solar and net longwave radiation distributions. Solar radiation on clear days, a baseline maximum value, increases by about 7% from sea level to the highest MauiNet site, 106, at 1650 meters. In winter, clear-day insolation is about 2/3 the summer value. The clear-day value can be estimated quite well using existing models that consider optical mass and the annual apparent path of the sun in the sky. Even though clear-day radiation increases with elevation, actual global radiation receipt declines with elevation because of increasing cloudiness due to local cloud producing mechanisms. The exception to this pattern over the MauiNet sites (for the period of record given in Appendix A) was above 1200 meters in winter

when global radiation increased with elevation. This suggests more vigorous sea-breeze and Maui vortex circulations in summer than winter. Also, horizontal insolation gradients are more pronounced in summer than winter. This may be related to more persistent winds in summer. Cloudiness decreased solar radiation over the study site from approximately the open ocean value at the lowest elevations, 85% of clear-sky radiation in winter and 80% in summer, to as little as 51% of clear-sky radiation in summer and 63% in winter higher on the mountain.

Longwave radiation transects from sea level to the summit of Haleakala suggested that incoming longwave radiation decreases more rapidly with elevation than outgoing longwave radiation under clear skies. This is related to the decrease in precipitable water in the atmosphere with height which absorbs and reemits outgoing longwave radiation. In the inversion layer, outgoing longwave radiation increased with elevation, while incoming longwave radiation continued to decrease. The cumulative effect was that net longwave radiation loss increased with elevation over the range of the transects.

Net radiation decreased with height, although

gradients were less pronounced than the solar radiation gradients. This was because the presence of clouds tends to moderate radiative flows. Net radiation was a higher percentage of solar radiation in summer than in winter because, while insolation drops to 2/3 of its summer value in winter, net longwave radiation remains fairly constant throughout the year. Also, a gradient in the ratio of net to solar radiation over the study site was apparent in winter (declining with elevation), but not in summer. This suggests a higher frequency of clear skies in winter than summer at higher elevations on the mountain.

Perhaps the most important contribution of this study was quantification of the importance of advection in influencing the evaporation rate on tropical high islands. At low elevations, advection from oceanic sources tended to moderate the annual fluctuation in the evaporation rate. The average influence at 20 pan evaporation stations ranged from +0.84 mm/day in November to -0.71 mm/day in June. In summer, positive heat advection from land sources increased evaporation by as much as 2.8 mm/day in the Maui isthmus. At high elevations, the evaporation rate increased in response to subsidence and the consequent mixing of dry air

through the subsidence inversion. The magnitude of advection at high elevations appeared to increase with elevation. This was most evident when comparing night evaporation at the three transect sites during the summer of 1989. The influence of advection at high elevations near and above the trade wind inversion was evident in both the summer and winter evaporation measurements. Several common evaporation models proved incapable of estimating the magnitude of the high elevation advection, underestimating evaporation at the highest sites. The evaporation enhancement appeared to be related to the maintenance of a high vapor-pressure deficit through the day and night, in contrast to the lower elevations where the vapor pressure deficit decreased dramatically at night.

It was suggested that potential evaporation could be modeled using the Priestley-Taylor equation modified by advection and high-elevation effect terms. Temperature and vapor pressure on the mountain could be estimated using rawinsonde data. Net radiation could be mapped from global radiation using a clear-day radiation baseline reduced to the open-ocean global radiation value, 80%, and further reduced based on a cloud index derived using a wind flow model or satellite derived

cloud estimates. Ocean advection could be accounted for at the lower elevations by simply adding a monthly modifier. Land advection could be related to soil moisture, estimated using a water balance. The effect of high elevation advection could be determined empirically, depending on season and elevation, or might be related to the free atmosphere vapor pressure deficit.

Conclusions

Existing models can only provide adequate estimates of evaporation in the Hawaiian Islands at wet inland sites where advection is minimal. These conditions existed for Ekern's (1983) study in the lee of the Koolau mountains on Oahu, for example. For lowland coastal sites, the effect of oceanic advection can account for up to 0.85 mm/day average evaporation enhancement in winter, easily 25% of total evaporation at some sites. At dry lee sites, advection from land sources can increase evaporation by much more than this. At high elevations, the effect of advection from synoptic-scale subsidence can account for fully 50% of the evaporative demand. This suggests that for applications that require accurate estimates of

evaporative demand, either a model that better accounts for effects of advection must be developed or users should rely on in situ evaporation measurements.

A logical next step for this study would be to build the evaporation model suggested in Chapter VIII. More data are needed first, however. The annual pattern of advection at high elevations needs to be studied with a transect beginning at 1000 meters or lower and running perhaps as high at the summit of the mountain. The relation of the night evaporation rate to the vapor pressure deficit needs to be quantified, if possible, and perhaps a new formula derived to model the phenomenon. In addition, models need to be developed to relate soil moisture to advection from land sources and fetch to ocean advection.

An evaporation model for high islands would have many applications in the Hawaiian Islands and other island groups in the tropics. In Hawaii such a model would be particularly useful when applied to a water balance to estimate recharge to existing aquifers. These estimates are used to plan sustainable yields from the aquifers. At present, no model is available to predict the distribution of net radiation and advection in the islands and so evaporation estimates depend

heavily on pan evaporation measurements in agricultural areas and sparse evaporation measurements in mountainous areas. Results from these measurements are generally extrapolated over large areas and consequently estimates contain large uncertainties. If these measurements were used to calibrate a model that considered topography, free atmospheric profiles, advection, and so forth, the resulting areal evaporation estimates would much better represent the gradients found in mountainous terrain and thus increase the confidence in estimated sustainable yield for the aquifers. Such a model would probably be of less use to large agricultural concerns in Hawaii as they have already compiled a large data base of pan evaporation measurements in most agricultural areas.

For developing nations in the tropical oceans, an evaporation model for high islands would be of great value as, in general, evaporation measurements are sparse or non-existent. The results could be used in agricultural development, aquifer development, and assessing drought hazard. As noted above, at present no such model exists.

Because of the magnitude of the influence of advection from land and ocean sources on evaporation, their inclusion in any model is considered important.

Probably of less practical importance would be the inclusion of advection at high elevations from synoptic-scale subsidence. This is not because the influence cannot be large, but because very few islands in tropics penetrate the inversion.

In addition to developing a suitable evaporation model, data need to be collected on other islands under other environmental conditions to verify the results given here. For example, a transect on the windward side of one of the islands would provide useful information. Also, no measurements were taken to study the evaporation rate from valleys, in which it has been shown elsewhere that the evaporation rate is unexpectedly high. Measurements on other islands in the tropics would provide a useful comparison to the data presented here as well. Ultimately, the potential evaporation estimates must be related to actual evaporation to be useful in water resources studies. A water-balance procedure could be used and checked against actual evaporation measurements, perhaps using eddy correlation instruments.

Finally, although many of the results presented in this study are based on data with a relatively long period of record, e.g. the Mauinet and pan evaporation

data, the high elevation effects discussed in Chapter VII are based on very limited measurements. Further measurements are needed to substantiate the claims made based on these limited data.

APPENDIX A. MAUINET STATIONS

	Station	Long	Lat	Elev (ft)	From (24 hour)	To	Comments
101	T. Hashimoto	1562705	204635	120	0783	—	
102	Pasture-Waiakoa	1562232	204646	1200	0783	—	
103	N. Nakamura	1561959	204655	2400	0783	0685	
104	Pasture-Kekoa	1561842	204744	2900	0783	—	
105	H. Hashimoto	1561823	204554	3850	0783	1187	
106	Pasture-Puupahu	1561648	204534	5400	0783	—	
107	Sugar-Paia	1562344	205322	200	0783	—	
108	Sugar-Waiakoa	1562430	204808	620	0783	—	
109	Pineapple-Haliimaile	1561946	205310	1130	0783	0685	
110	Pineapple-Pukalani	1561952	205100	1680	0783	0685	
111	Forest-Olinda	1561700	204828	3700	0783	0187	
112	M. Yamamoto	1562027	204638	2240	0484	0485	15 min 0485->0685
113	Sugar-Maalaea	1563040	204830	125	1087	—	30 min 1284->0585
114	Kuiaha	1561804	205408	940	0585	—	Wind, PAR, No Sm10
115	Haleakala I	1561745	205043	2100	0585	—	Wind, No Sm10
116	IBSNAT-Olinda	1561709	204844	3500	0785	—	Wind, PAR, No Sm10
117	Kula Ag. Park	1562130	204800	1400	0186	—	30 min 0785-> —
118	Pulehu Exp. Farm	1562027	204638	2100	0186	—	30 min 0785-> —
119	Kula Exp. Sta.	1561923	204538	3100	0186	—	30 min 0785-> —
122	Haleakala II	1561740	205043	2125	0287	—	Wind, PAR, No Sm10
301	NiFTAL Hamakuapoko	1562100	205502	320	1085	—	Wind, No Sm&Tsoil
302	Site 261	1562016	205216	1200	0186	—	Wind, No Sm&Tsoil
303	Site 275	1561852	204840	2400	0186	—	Wind, No Sm&Tsoil

Current standard measurements, 24 hour:

Air Temperature in ^{o}C	mean, max, min
Relative Humidity in %	mean, max, min
Soil Temp. @ 10cm in ^{o}C	mean, max, min
Soil Temp. @ 50cm in ^{o}C	mean
Soil Moisture @ 10cm in volts	max, min
Soil Moisture @ 50cm in volts	max, min
Solar Radiaton in MJ/m^2	total
Rainfall in mm	total
Battery Voltage in millivolts	

Current standard measurements, 30 minute:

Air Temperature ^{o}C	mean
Soil Temp. @ 10cm in ^{o}C	mean
Soil Temp. @ 50cm in ^{o}C	mean
Soil Moisture @ 10cm in volts	mean
Soil Moisture @ 50cm in volts	mean
Relative Humidity in %	mean
Solar Radiation in MJ/m^2	total
Rainfall in mm	total

APPENDIX B1. WINTER EVAPORATION DATA (mm)

YR	DAY	106	114	115	116	117	119
87	327	85	67	122	112	167	61
87	328	94	151	146	97	147	91
87	329	132	95	100	61	190	112
87	330	362	170	152	192	153	160
87	331	186	207	151	60	231	119
87	334	262	72	82	170	184	99
87	335	180	137	123	70	137	130
87	336	123	159	100	100	245	138
87	356	60	95	75	40	140	50
87	357	75	135	80	75	140	95
87	358	135	142	92	36	111	68
87	359	112	124	113	87	109	85
87	360	94	113	129	97	146	99
87	361	145	145	100	53	93	98
87	362	159	107	85	66	168	95
87	363	135	63	60	61	116	85
87	364	69	105	88	62	121	81
88	3	94	117	89	22	172	108
88	4	89	154	94	78	120	118
88	5	119	74	74	51	112	106
88	6	240	120	96	112	118	112
88	7	211	192	131	102	130	130
88	8	100	130	96	82	121	96
88	9	61	17	39	14	71	90

APPENDIX B2. WINTER SOLAR RADIATION DATA (MJ/m^2)

YY	DAY	106	114	115	116	117	119
87	327	14.5	15.4	17.5	12.6	18.2	16.2
87	328	11.7	17.7	16.6	10.7	13.5	11.0
87	329	17.0	12.9	18.6	13.9	15.5	14.7
87	330	18.8	15.9	17.8	14.0	17.9	17.7
87	331	13.8	14.7	18.3	14.0	18.2	16.4
87	334	12.6	8.8	15.1	13.2	14.0	14.9
87	335	16.2	13.0	16.8	13.1	16.9	16.5
87	336	17.8	11.7	13.8	11.9	16.5	16.7
87	356	7.3	10.7	8.1	5.1	9.4	5.9
87	357	10.4	14.4	11.8	7.5	16.8	16.5
87	358	12.2	17.7	12.5	8.7	14.2	10.7
87	359	11.8	15.9	17.5	7.4	13.0	12.7
87	360	15.9	16.5	15.2	9.8	17.9	15.8
87	361	15.3	15.5	15.3	8.6	16.1	14.1
87	362	13.5	16.4	10.6	8.9	12.3	12.0
87	363	11.8	10.4	11.2	7.6	13.9	11.0
87	364	8.1	12.8	10.0	6.2	13.7	10.7
88	3	14.3	12.8	14.5	11.2	16.8	16.8
88	4	10.1	16.3	13.4	8.6	16.7	17.0
88	5	14.4	11.7	13.5	10.4	15.0	14.0
88	6	14.3	10.9	14.8	11.6	16.2	16.7
88	7	17.1	18.5	17.5	13.2	17.9	17.8
88	8	16.9	16.8	15.1	13.1	17.1	13.6
88	9	13.1	4.6	11.5	11.0	15.9	16.0

APPENDIX B3. WINTER TEMPERATURE DATA (°C)

YY	DAY	106	114	115	116	117	119
87	327	14.5	22.0	20.6	18.0	22.2	18.8
87	328	13.8	22.3	21.0	18.3	22.3	18.9
87	329	13.1	21.3	19.5	16.9	21.6	17.7
87	330	15.1	21.5	19.4	17.1	21.3	17.5
87	331	15.1	21.6	19.4	16.9	21.6	17.4
87	334	15.6	20.8	19.2	17.0	21.8	17.9
87	335	15.5	21.4	19.2	17.0	20.7	17.2
87	336	12.4	21.0	18.0	15.1	19.9	16.8
87	356	13.0	21.1	19.2	16.1	20.8	17.0
87	357	12.4	21.7	18.8	15.7	20.9	17.4
87	358	13.1	21.7	19.6	16.1	20.7	17.0
87	359	12.6	20.8	18.4	15.1	20.1	16.7
87	360	13.4	20.6	19.5	17.0	20.8	17.0
87	361	13.0	21.1	19.4	16.1	20.7	17.0
87	362	12.1	21.1	18.4	15.2	19.6	16.2
87	363	12.3	19.7	18.5	15.2	19.5	16.7
87	364	12.2	20.7	17.9	15.1	20.3	16.7
88	3	9.5	17.5	15.3	12.4	17.7	15.2
88	4	11.2	18.6	16.2	14.1	18.4	15.3
88	5	12.0	19.5	17.0	14.9	18.4	16.1
88	6	11.9	19.3	17.4	14.8	19.6	16.0
88	7	11.9	19.6	16.9	14.8	18.4	15.1
88	8	10.6	20.0	16.5	13.5	18.5	14.5
88	9	12.6	19.7	18.2	15.5	19.5	17.5

APPENDIX B4. WINTER VAPOR PRESSURE (mb)

YY	DAY	106	114	115	116	117	119
87	327	14.2	24.7	21.7	18.7	23.2	19.5
87	328	15.3	24.8	21.7	19.2	24.0	20.1
87	329	13.0	23.4	20.3	17.2	22.2	18.2
87	330	11.4	23.2	19.8	16.4	21.3	17.2
87	331	11.5	22.9	19.5	15.9	21.3	17.4
87	334	13.4	23.2	20.8	17.9	22.7	18.6
87	335	10.5	23.0	19.5	16.7	21.0	17.3
87	336	10.8	22.2	18.7	15.6	20.1	16.5
87	356	14.1	22.7	20.1	17.1	22.2	18.1
87	357	12.5	23.4	19.2	16.1	21.4	17.7
87	358	12.8	23.4	19.8	16.7	21.3	17.6
87	359	11.0	22.7	19.2	15.8	20.5	17.0
87	360	12.3	22.3	19.6	16.8	21.2	17.4
87	361	11.5	22.0	19.2	16.2	21.0	17.4
87	362	9.8	22.0	18.5	15.6	19.5	16.4
87	363	10.1	21.6	19.2	15.3	19.7	16.3
87	364	10.8	22.4	18.6	15.5	20.3	17.0
88	3	7.6	18.3	16.0	13.5	17.7	15.4
88	4	8.2	19.3	16.7	14.3	18.2	15.5
88	5	8.8	20.4	17.4	14.7	18.7	15.7
88	6	9.7	20.6	17.9	14.9	19.4	15.8
88	7	7.7	19.8	16.2	12.3	17.8	13.9
88	8	7.5	20.3	16.0	12.7	17.6	13.9
88	9	10.5	21.9	19.3	16.1	20.0	17.4

APPENDIX B5. WINTER WIND DATA (m/s)

YY	DAY	106	114	115	116	117	119
87	327	1.3	2.5	2.6	2.7	0.0	0.6
87	328	1.3	3.6	3.8	4.0	1.4	1.3
87	329	2.0	3.4	3.5	3.5	1.9	1.9
87	330	2.9	3.6	2.7	1.7	1.5	2.2
87	331	1.7	1.6	1.8	1.9	4.2	3.0
87	334	2.3	3.0	1.8	0.5	1.6	2.0
87	335	1.3	3.4	2.9	2.3	1.7	1.5
87	336	2.0	4.5	3.2	1.8	3.3	2.6
87	356	1.4	4.8	3.2	1.6	1.2	1.3
87	357	1.2	4.4	3.7	3.0	1.5	1.3
87	358	1.2	5.2	4.2	3.2	1.2	1.2
87	359	1.2	5.3	4.4	3.4	1.2	1.2
87	360	1.2	4.9	4.6	4.2	1.8	1.5
87	361	1.4	4.9	4.4	3.8	1.5	1.5
87	362	1.5	5.1	4.0	2.9	2.0	1.7
87	363	1.3	4.4	3.4	2.4	1.3	1.3
87	364	0.9	3.3	2.9	2.4	1.3	1.1
88	3	1.9	3.6	2.8	2.1	4.6	3.3
88	4	1.4	5.2	3.7	2.2	1.2	1.3
88	5	1.9	2.9	2.3	1.7	2.9	2.4
88	6	1.8	0.6	1.0	1.5	1.5	1.6
88	7	1.1	1.1	1.3	1.6	1.7	1.4
88	8	1.0	2.3	1.9	1.4	1.2	1.1
88	9	1.7	2.1	1.8	1.5	0.2	1.0

APPENDIX C1: SUMMER MEASUREMENTS AT KULA EXP. STATION

yymmdd	Evap mm	PE1 mm	PE2 mm	PE3 mm	PE4 mm	Q^* MJ/m^2	Td °C	vpd mb	vp mb	u m/s
880707	4.1	3.6	3.4	3.5	4.1	11.8	18.4	2.4	18.8	1.2
880708	3.9	3.7	3.5	3.6	4.3	12.3	18.5	2.4	18.8	1.2
880709	2.2	2.4	2.3	2.3	2.8	8.1	17.4	1.4	18.4	0.8
880710	2.2	2.4	2.2	2.3	2.8	8.0	17.4	1.7	18.1	1.0
880711	2.7	3.4	3.2	3.3	4.0	11.3	18.6	2.2	19.1	0.8
880712	2.2	3.0	2.8	2.9	3.5	9.9	18.5	1.9	19.4	0.7
880713	2.6	4.3	4.1	4.2	5.0	14.2	18.3	2.7	18.3	1.2
880714	3.5	3.1	2.9	3.0	3.5	9.9	18.5	2.5	18.8	0.9
880715	3.9	4.2	3.9	4.0	4.8	13.9	17.8	2.8	17.6	0.9
880716	3.8	4.5	4.2	4.4	5.2	15.0	18.0	3.0	17.6	1.0
880717	3.1	3.9	3.6	3.8	4.5	12.8	18.3	2.7	18.4	0.9
880718	3.4	4.3	4.1	4.2	5.0	14.2	18.6	3.1	18.4	0.8
880719	3.5	3.5	3.2	3.4	3.9	11.2	17.8	3.8	16.6	0.7
880720	3.6	4.1	3.8	4.0	4.7	13.5	17.8	3.4	16.9	0.9
880721	2.2	2.5	2.2	2.3	2.6	7.6	17.4	3.1	16.8	0.8
880722	2.2	4.0	3.7	3.9	4.5	12.8	18.1	3.7	17.1	1.0
880810	4.9	3.6	3.4	3.5	4.1	11.5	19.1	2.8	19.3	1.0
880811	1.4	1.4	1.4	1.4	1.7	4.7	19.3	0.9	21.5	0.6
880812	3.2	2.7	2.6	2.6	3.2	9.0	19.5	1.2	21.5	1.2
880813	4.5	3.2	3.0	3.1	3.7	10.5	18.7	2.2	19.3	1.2
880814	3.7	3.1	2.9	3.0	3.4	9.9	18.1	2.5	18.3	1.3
880815	5.8	4.6	4.3	4.5	5.3	15.0	18.5	3.2	18.1	1.2
880816	3.5	2.7	2.4	2.5	2.9	8.4	18.0	3.2	17.4	0.5
880817	3.9	3.4	3.1	3.3	3.8	10.8	18.7	3.3	18.2	0.6
880818	3.9	4.1	3.8	4.0	4.7	13.5	17.8	3.6	16.8	0.7
880819	2.6	2.5	2.3	2.4	2.8	8.2	17.6	2.5	17.6	0.6
880820	2.2	2.5	2.2	2.4	2.7	7.9	17.5	2.5	17.5	0.6
880902	5.1	3.6	3.4	3.5	4.2	12.0	18.9	3.0	18.8	0.0
880903	3.3	2.5	2.4	2.5	2.9	8.3	18.4	2.1	19.1	0.8

PE1: Penman
PE2: Penman-Van Bavel
PE3: Penman-Monteith
PE4: Priestley-Taylor

APPENDIX C2: SUMMER MEASUREMENTS AT PUU PAHU

yymmdd	Evap mm	PE1 mm	PE2 mm	PE3 mm	PE4 mm	Q^* MJ/m^2	Td ^oC	vpd mb	vp mb	u m/s
880617	1.6	2.1	1.8	1.9	2.0	6.3	12.7	2.6	12.1	1.8
880618	2.1	3.3	3.0	3.1	3.4	10.2	13.6	3.3	12.2	1.9
880715	4.9	3.8	3.3	3.5	3.7	10.8	14.9	4.9	12.1	2.1
880716	6.3	5.0	4.4	4.6	5.0	14.4	15.8	6.0	11.9	2.0
880717	4.8	3.7	3.1	3.4	3.4	9.9	16.2	6.1	12.3	1.8
880718	5.2	4.3	3.6	3.8	3.8	10.9	16.8	7.0	12.1	2.2
880719	4.1	2.7	2.2	2.4	2.1	6.2	14.5	5.6	10.9	2.2
880720	4.0	3.5	3.0	3.2	3.3	9.7	14.7	4.8	11.9	2.1
880721	2.2	1.8	1.4	1.5	1.3	4.0	13.6	4.1	11.5	1.8
880722	3.8	3.2	2.7	2.8	2.7	8.1	14.4	4.8	11.5	2.5
880723	4.5	4.1	3.6	3.8	3.9	11.6	14.4	4.9	11.4	2.3
880724	2.2	2.2	1.8	1.9	1.8	5.4	13.4	3.9	11.4	2.1
880725	1.7	2.0	1.6	1.8	1.7	4.9	16.3	4.0	14.5	1.7
880726	3.7	4.0	3.5	3.7	4.1	11.8	16.7	4.7	14.4	1.5
880727	4.0	4.4	4.0	4.2	4.6	13.2	16.3	4.9	13.7	1.8
880728	5.8	5.0	4.4	4.6	4.8	13.9	16.6	5.8	13.0	2.6
880729	4.1	3.6	3.1	3.3	3.3	9.7	16.2	5.5	12.9	2.1
880730	8.3	6.1	5.3	5.6	5.8	16.1	19.0	8.6	13.3	2.3
880731	5.9	5.3	4.7	5.0	5.3	15.4	16.2	6.4	12.0	2.0
880801	2.8	2.9	2.5	2.6	2.7	8.0	14.1	4.2	11.9	2.0
880802	3.2	3.4	3.0	3.1	3.3	9.6	15.7	4.7	13.1	1.8
880803	2.3	2.6	2.1	2.3	2.4	6.9	15.7	4.7	13.1	1.3
880804	4.9	4.3	3.7	4.0	4.2	11.9	17.1	5.9	13.6	1.8
880805	4.8	4.1	3.5	3.8	3.9	11.1	16.9	6.3	12.9	1.8
880806	2.8	2.7	2.2	2.4	2.4	6.9	16.6	5.1	13.8	1.5
880807	1.5	1.9	1.6	1.7	1.7	4.9	17.2	3.9	15.7	1.3
880808	1.3	2.1	1.7	1.9	1.9	5.3	19.0	5.1	16.8	0.9
880809	2.9	3.0	2.6	2.8	3.1	9.0	16.7	4.3	14.6	0.7
880810	3.2	2.8	2.5	2.6	2.8	8.1	15.9	3.9	14.2	1.6
880811	1.7	1.8	1.5	1.6	1.5	4.4	17.0	4.1	15.2	1.5
880812	2.1	2.6	2.2	2.4	2.5	7.1	17.8	4.3	16.1	1.5
880813	3.7	3.1	2.6	2.8	2.8	7.9	16.9	5.6	13.7	1.9
880814	2.1	2.0	1.6	1.8	1.7	4.9	16.0	4.0	14.2	1.5
880815	4.5	3.5	3.1	3.3	3.6	10.6	14.9	3.8	13.1	1.8
880816	2.1	1.7	1.4	1.5	1.4	4.2	14.1	3.5	12.5	1.6
880817	3.6	3.1	2.7	2.8	3.0	8.6	15.6	4.3	13.3	1.8
880818	5.4	3.6	3.2	3.4	3.5	10.6	14.5	4.8	11.7	1.8
880819	3.2	2.3	2.0	2.1	2.2	6.5	13.9	3.6	12.3	1.7
880820	3.6	2.7	2.4	2.5	2.6	7.8	14.0	3.7	12.2	2.0
880906	1.6	1.7	1.5	1.6	1.8	5.1	17.1	2.0	17.5	1.3

PE1: Penman
PE2: Penman-Van Bavel
PE3: Penman-Monteith
PE4: Priestley-Taylor

APPENDIX C3: SUMMER MEASUREMENTS AT HALEAKALA HEADQUARTERS

yymmdd	Evap mm	PE1 mm	PE2 mm	PE3 mm	PE4 mm	Q^* MJ/m^2	Td °C	vpd mb	vp mb	u m/s
880617	5.9	4.7	4.1	4.4	4.7	14.4	11.8	6.0	7.9	1.4
880618	7.6	5.3	4.7	5.0	5.3	15.9	13.0	6.0	9.0	2.0
880619	7.0	5.1	4.5	4.7	5.1	14.9	14.4	6.0	10.4	1.9
880707	6.6	6.1	5.6	5.6	5.7	17.6	12.2	3.5	10.7	6.7
880708	3.6	4.0	3.8	3.9	4.5	13.8	11.8	1.8	12.0	3.3
880709	4.1	3.7	3.3	3.4	3.6	11.4	10.7	2.6	10.3	4.2
880710	4.1	3.2	2.8	2.9	3.0	9.3	11.7	3.2	10.5	3.0
880711	8.4	6.5	5.7	5.8	5.5	16.4	14.0	7.3	8.7	4.3
880712	10.1	7.9	6.7	6.8	5.6	15.8	16.8	12.3	6.9	4.8
880713	5.7	4.6	3.9	4.2	4.4	13.3	12.2	6.1	8.2	1.8
880714	6.5	5.5	4.8	5.1	5.4	16.0	13.9	7.2	8.7	1.6
880715	5.4	4.8	4.2	4.4	4.8	14.5	12.2	5.7	8.5	1.6
880716	7.0	6.2	5.4	5.8	6.1	18.3	13.4	8.1	7.2	1.6
880717	7.0	5.5	4.7	5.1	5.5	16.2	14.4	8.3	8.1	1.0

PE1: Penman
PE2: Penman-Van Bavel
PE3: Penman-Monteith
PE4: Priestley-Taylor

APPENDIX D1. HALEAKALA NIGHT TEMPERATURE TRANSECT No1: 27Nov1987

TIME	PRESS mb	ELEV m	Td C	Tw C	RH %	E* mb	Ea mb	ppw mm	Ts C	Lout W/m2	Tcl C	Lin W/m2
2035	712.2	3055	7.9	-1.4	10	10.53	1.08	5.00	1.4	315.03	-54.5	126.65
2100	725.3	2862	10.6	1.0	15	12.64	1.89	0.22	0.0	308.65	-56.4	122.30
2114	750.0	2582	11.0	1.0	12	12.98	1.53	0.37	8.0	346.45	-56.0	123.21
2128	775.0	2267	11.3	1.3	11	13.24	1.51	0.37	8.5	348.92	-55.3	124.81
2140	800.0	2028	10.8	1.4	13	12.81	1.71	0.29	7.0	341.54	-53.5	128.99
2153	825.0	1761	11.2	4.6	36	13.15	4.77	0.66	4.3	328.56	-53.1	129.93
2202	850.0	1506	11.6	10.8	91	13.51	12.35	1.66	10.9	360.97	-42.8	156.04
2217	875.0	1256	14.2	12.6	84	16.02	13.49	2.45	12.0	366.60	-41.7	159.04
2227	900.0	1029	13.4	12.8	94	15.20	14.26	2.38	13.0	371.77	-36.9	172.66
2239	925.0	800	16.5	15.0	86	18.57	15.94	2.60	15.2	383.34	-13.0	253.92
2252	950.0	607	19.4	17.0	79	22.29	17.64	2.41	17.1	393.55	-27.2	202.83
2310	975.0	358	20.6	18.4	81	24.02	19.50	3.42	18.1	399.00	-23.7	214.63
2317	1000.0	144	22.2	20.5	86	26.49	22.72	3.32	20.1	410.08	-18.7	232.38
2328	1017.0	0	22.3	21.0	89	26.65	23.72	2.45	20.7	413.45	-16.4	240.90
								27.6				

APPENDIX D2. HALEAKALA NIGHT TEMPERATURE TRANSECT No2: 07JAN88

TIME	PRES mb	ELEV m	Td C	Tw C	RH %	E* mb	Ea mb	ppw mm	Ts C	Lout W/m2	Tcl C	Lin W/m2
2030	710	3055	5.8	-1.9	18	9.12	1.65	5.00	0.0	308.65	-55.3	124.81
2100	725	2888	8.2	-0.5	15	10.75	1.66	0.21	7.2	342.52	-53.2	129.69
2111	750	2618	10.1	0.8	15	12.22	1.79	0.36	9.0	351.40	-52.4	131.59
2128	775	2327	10.2	1.4	18	12.30	2.17	0.44	7.5	343.99	-51.5	133.75
2140	800	2047	9.1	1.5	24	11.43	2.71	0.52	5.5	334.28	-50.2	136.92
2200	825	1790	9.9	2.2	24	12.06	2.87	0.55	7.0	341.54	-50.2	136.92
2210	850	1546	11.9	3.8	24	13.78	3.36	0.58	7.4	343.50	-49.3	139.15
2230	875	1308	10.2	5.5	50	12.30	6.20	0.87	6.3	338.14	-46.0	147.54
2245	900	1077	9.8	6.8	67	11.98	7.87	1.24	7.3	343.01	-43.0	155.50
2300	925	856	9.5	8.4	87	11.74	10.22	1.53	7.2	342.52	-39.1	166.31
2315	950	593	13.0	11.4	83	14.81	12.31	2.26	9.6	354.40	-35.1	177.99
2330	975	376	13.0	12.2	91	14.81	13.53	2.12	12.3	368.14	-31.9	187.76
2335	1000	169	17.7	14.4	70	20.04	14.01	2.14	14.9	381.75	-29.5	195.35
2345	1017	0	20.5	17.2	72	23.87	17.16	1.95	17.2	394.09	-27.1	203.16
								19.8				

APPENDIX E1. MAIN PROGRAM FOR CLEAR DAY RADIATION CALCULATION

```
/*  find daily totals of solar radiation for SPCTRAL2 model */
/*                                        Dennis Nullet, 1987   */

#include <stdio.h>
#include <math.h>

double xi[20],w[20];
int ngauss = 8;

main()
{
int d,i,begin,end;
double integ();
float dayang,dec,sunris,orbit,rad,lat,sum;
float wl[123],Hol[123],awl[123],aol[123],aul[123],band[123];
float pi = 3.141593;
float units = 60.0*60.0*24.0/2.0/pi/1000000.0;
FILE *spectra,*gauss,*fopen();

gauss = fopen("gauss","r");
for(i=1;i<=(ngauss/2);i++)
  fscanf(gauss,"%lf %lf",&xi[i],&w[i]);
fclose(gauss);

printf(" Enter the from and to day: ");
scanf("%d %d",&begin,&end);
printf(" Enter the latitude: ");
scanf("%f",&lat);
lat *= pi/180.0;
spectra = fopen("spectral.data","r");
for (i=1;i<=122;i++)
  fscanf(spectra,"%f %f %f %f %f",&wl[i],&Hol[i],&awl[i],&aol[i],&aul[i]);
for (i=2;i<=121;i++)
  band[i]=0.5*(wl[i+1] - wl[i-1]);
band[1] = 0.005;
band[122] = 0.1;
fclose(spectra);
spectra = fopen("daily.dat","w");

for (d=begin;d<=end;d++)
  {
  sum = 0.0;
  dayang = (d-1)*2.0*pi/365.0;
  dec = 0.006918-0.399912*cos(dayang)+0.070257*sin(dayang)-
        0.006758*cos(2.0*dayang)+0.000907*sin(2.0*dayang)-
        0.002697*cos(3.0*dayang)+0.00148*sin(3.0*dayang);
  sunris = (tan(lat)*tan(dec) > 1.0) ? pi : acos(-tan(lat)*tan(dec)) ;
```

```
  orbit = 1.00011+0.034221*cos(dayang)+0.00128*sin(dayang)+
          0.000719*cos(2.0*dayang)+0.000077*sin(2.0*dayang);
  for (i=1;i<=122;i++)  {
    rad = integ(0.0,sunris,dec,lat,wl[i],Hol[i],awl[i],aol[i],aul[i],orbit);
    sum += 2.0*rad*band[i]*units;
    }
  printf("On day %d, radiation = %6.2f MJ/m sq. \n",d,sum);
  fprintf(spectra,"%d %6.2f\n",d,sum);
  }
fclose(spectra);
}
```

APPENDIX E2. SPCTRAL2 MODEL SUBROUTINE

```
/* Spectrl2 model from Bird & Riordan (JCAM, Jan, 1986)   */
/*                                    Dennis Nullet, 1987   */

#include <stdio.h>
#include <math.h>
double funct(x,dec,lat,wl,Hol,awl,aol,aul,D)
double x,dec,lat,wl,awl,aol,aul,Hol,D;
{
double coszen,y,optm,Trl,Tal,Twl,Tol,Tul,Idl,w04,wp,costh,wla,ALG,BFS;
double AFS,Fs,Fsp,Taal,Tasl,rsl,Irl,Ial,Igl,Isl,tal;
float pi = 3.141593;
float W = 3.0;          /*  Honolulu 3.0, MLO 0.5 */
float Bn = 0.05;        /*  Honolulu 0.05, MLO 0.015 */
float an = 1.3;
float rgl = 0.2;
float O3 = 0.26;
float Po = 1016.0;      /*  Honolulu 1016.0, MLO 675  */

coszen = sin(dec)*sin(lat)+cos(dec)*cos(lat)*cos(x);
optm = 1.0/(coszen + 0.15*pow((93.885-acos(coszen)*180./pi),-1.253));

/*  Direct beam calculations */

Trl = exp(-(optm*Po/1013.0)/(pow(wl,4.0)*(115.6406-1.335/pow(wl,2.0))));
tal = Bn*pow(wl,-an);
Tal = exp(-tal*optm);
Twl = exp(-0.2385*awl*W*optm/pow((1.0+20.07*awl*W*optm),0.45));
Tol = exp(-aol*O3*optm);
Tul = exp(-1.41*aul*optm*Po/1013.0/pow((1.0+118.3*aul*optm*Po/1013.0),0.45))
Idl = Hol*D*Trl*Tal*Twl*Tol*Tul*coszen;

/* Diffuse calculations */

w04 = 0.945;
wp = 0.095;
costh = 0.65;
wla = w04*exp(-wp*pow(log(wl/0.4),2.0));
ALG = log(1.0-costh);
BFS = ALG*(0.0783+ALG*(-0.3824-ALG*0.5874));
AFS = ALG*(1.459+ALG*(0.1595+ALG*0.4129));
Fs = 1.0 - 0.5*exp((AFS+BFS*coszen)*coszen);
Fsp = 1.0 - 0.5*exp((AFS+BFS/1.8)/1.8);
Tasl = exp(-wla*tal*optm);
Taal = exp(-(1.0-wla)*tal*optm);
rsl = Tol*Twl*Taal*(0.5*(1.0-Trl)+(1.0-Fsp)*Trl*(1.0-Tasl));
Irl = Hol*D*coszen*Tol*Tul*Twl*Taal*(1.0-pow(Trl,0.95))*0.5;
Ial = Hol*D*coszen*Tol*Tul*Twl*Taal*pow(Trl,1.5)*(1.0-Tasl)*Fs;
Igl = (Idl+Irl+Ial)*rsl*rgl/(1.0-rsl*rgl);
Isl = Irl+Ial+Igl;
if (wl <= 0.45)
  Isl *= pow((wl+0.55),1.8);
y=Idl+Isl;
return(y);
}
```

APPENDIX E3. NUMERICAL INTEGRATION SUBROUTINE

```
/*  Gauss quadrature numerical integration subroutine     */
/*                                   Dennis Nullet, 1987  */
/*                  adapted from Mike Nullet              */

#include <stdio.h>
double integ(a,b,dec,lat,wl,Hol,awl,aol,aul,D)
double a,b,dec,lat,wl,Hol,awl,aol,aul,D;
{
extern int ngauss;
extern double xi[20],w[20];
int i;
double sum,answer,ab,ba,y,funct();
double x[30],yy[30];

  sum=0;
  ba=b-a;
  ab=b+a;
  for (i=1;i<=ngauss;i++)
    if (i <= ngauss/2)
    {
      x[i] = (ab/2.0)+(ba/2.0*-xi[i]);
      y = funct(x[i],dec,lat,wl,Hol,awl,aol,aul,D);
      yy[i] = w[i]*y;
    }
    else
    {
      w[i] = w[ngauss-i+1];
      x[i] = (ab/2.0)+(ba/2.0)*(xi[ngauss-i+1]);
      y = funct(x[i],dec,lat,wl,Hol,awl,aol,aul,D);
      yy[i] = w[i]*y;
    }
  for (i=1;i<=ngauss;i++)
    sum += yy[i];
  answer = ba/2.0*sum;

return(answer);
}
```

APPENDIX E4. SPECTRAL INFORMATION

0.300	535.9	0.0	10.0	0.0
0.305	558.3	0.0	4.80	0.0
0.310	662.0	0.0	2.70	0.0
0.315	692.7	0.0	1.35	0.0
0.320	715.1	0.0	0.800	0.0
0.325	832.9	0.0	0.380	0.0
0.330	961.9	0.0	0.160	0.0
0.335	931.9	0.0	0.075	0.0
0.340	900.6	0.0	0.040	0.0
0.345	911.3	0.0	0.019	0.0
0.350	975.5	0.0	0.007	0.0
0.360	975.9	0.0	0.0	0.0
0.370	1119.9	0.0	0.0	0.0
0.380	1103.8	0.0	0.0	0.0
0.390	1033.8	0.0	0.0	0.0
0.400	1479.1	0.0	0.0	0.0
0.410	1701.3	0.0	0.0	0.0
0.420	1740.4	0.0	0.0	0.0
0.430	1587.2	0.0	0.0	0.0
0.440	1837.0	0.0	0.0	0.0
0.450	2005.0	0.0	0.003	0.0
0.460	2043.0	0.0	0.006	0.0
0.470	1987.0	0.0	0.009	0.0
0.480	2027.0	0.0	0.014	0.0
0.490	1896.0	0.0	0.021	0.0
0.500	1909.0	0.0	0.030	0.0
0.510	1927.0	0.0	0.040	0.0
0.520	1831.0	0.0	0.048	0.0
0.530	1891.0	0.0	0.063	0.0
0.540	1898.0	0.0	0.075	0.0
0.550	1892.0	0.0	0.085	0.0
0.570	1840.0	0.0	0.120	0.0
0.593	1768.0	0.075	0.190	0.0
0.610	1728.0	0.0	0.120	0.0
0.630	1658.0	0.0	0.090	0.0
0.656	1524.0	0.0	0.065	0.0
0.6676	1531.0	0.0	0.051	0.0
0.690	1420.0	0.0	0.028	0.15
0.710	1388.0	0.0125	0.018	0.0
0.718	1374.0	1.8	0.015	0.0
0.7244	1373.0	2.5	0.012	0.0
0.740	1298.0	0.061	0.010	0.0
0.7525	1269.0	0.0008	0.008	0.0
0.7575	1245.0	0.0001	0.007	0.0
0.7625	1223.0	0.00001	0.006	4.0
0.7675	1205.0	0.00001	0.005	0.35
0.780	1183.0	0.0006	0.0	0.0
0.800	1148.0	0.036	0.0	0.0

0.816	1091.0	1.60	0.0	0.0
0.8237	1062.0	2.5	0.0	0.0
0.8315	1038.0	0.500	0.0	0.0
0.840	1022.0	0.155	0.0	0.0
0.860	998.7	0.00001	0.0	0.0
0.880	947.2	0.0026	0.0	0.0
0.905	893.2	7.0	0.0	0.0
0.915	868.2	5.0	0.0	0.0
0.925	829.7	5.0	0.0	0.0
0.930	830.3	27.0	0.0	0.0
0.937	814.0	55.0	0.0	0.0
0.948	786.9	45.0	0.0	0.0
0.965	768.3	4.0	0.0	0.0
0.980	767.0	1.48	0.0	0.0
0.9935	757.6	0.1	0.0	0.0
1.04	688.1	0.00001	0.0	0.0
1.07	640.7	0.001	0.0	0.0
1.10	606.2	3.2	0.0	0.0
1.12	585.9	115.0	0.0	0.0
1.13	570.2	70.0	0.0	0.0
1.145	564.1	75.0	0.0	0.0
1.161	544.2	10.0	0.0	0.0
1.17	533.4	5.0	0.0	0.0
1.20	501.6	2.0	0.0	0.0
1.24	477.5	0.002	0.0	0.05
1.27	442.7	0.002	0.0	0.30
1.29	440.0	0.1	0.0	0.02
1.32	416.8	4.0	0.0	0.0002
1.35	391.4	200.0	0.0	0.00011
1.395	358.9	1000.0	0.0	0.00001
1.4425	327.5	185.0	0.0	0.05
1.4625	317.5	80.0	0.0	0.011
1.477	307.3	80.0	0.0	0.005
1.497	300.4	12.0	0.0	0.0006
1.520	292.8	0.16	0.0	0.0
1.539	275.5	0.002	0.0	0.005
1.558	272.1	0.0005	0.0	0.13
1.578	259.3	0.0001	0.0	0.04
1.592	246.9	0.00001	0.0	0.06
1.610	244.0	0.0001	0.0	0.13
1.630	243.5	0.001	0.0	0.001
1.646	234.8	0.01	0.0	0.0014
1.678	220.5	0.036	0.0	0.0001
1.740	190.8	1.1	0.0	0.00001
1.800	171.1	130.0	0.0	0.00001
1.860	144.5	1000.0	0.0	0.0001
1.920	135.7	500.0	0.0	0.001
1.960	123.0	100.0	0.0	4.3
1.985	123.8	4.0	0.0	0.20
2.005	113.0	2.9	0.0	21.0
2.035	108.5	1.0	0.0	0.13

2.065	97.5	0.4	0.0	1.0
2.100	92.4	0.22	0.0	0.08
2.148	82.4	0.25	0.0	0.001
2.198	74.6	0.33	0.0	0.00038
2.270	68.3	0.50	0.0	0.001
2.360	63.8	4.0	0.0	0.0005
2.450	49.5	80.0	0.0	0.00015
2.5	48.5	310.0	0.0	0.00014
2.6	38.6	15000.0	0.0	0.00066
2.7	36.6	22000.0	0.0	100.0
2.8	32.0	8000.0	0.0	150.0
2.9	28.1	650.0	0.0	0.13
3.0	24.8	240.0	0.0	0.0095
3.1	22.1	230.0	0.0	0.001
3.2	19.6	100.0	0.0	0.8
3.3	17.5	120.0	0.0	1.9
3.4	15.7	19.5	0.0	1.3
3.5	14.1	3.6	0.0	0.075
3.6	12.7	3.1	0.0	0.01
3.7	11.5	2.5	0.0	0.00195
3.8	10.4	1.4	0.0	0.004
3.9	9.5	0.17	0.0	0.29
4.0	8.6	0.0045	0.0	0.025

APPENDIX E5. GAUSS MULTIPLIERS

0.1834346425	0.3626837834
0.5255324099	0.3137066459
0.7966664774	0.2223810345
0.9602898565	0.1012285363

APPENDIX F. PAN EVAPORATION STATIONS AND RANK

(State Key Number given to identify stations)

Rank	Station	Rank	Station
1	89.5	26	934.0
2	1104.2	27	986.1
3	213.0	28	707.0
4	213.1	29	944.0
5	1016.0	30	940.0
6	1092.0	31	738.4
7	825.3	32	847.0
8	1062.1	33	14.0
9	1114.0	34	982.0
10	1020.4	35	737.0
11	90.1	36	416.0
12	215.3	37	740.4
13	1101.0	38	908.0
14	841.0	39	221.3
15	761.1	40	741.0
16	861.0	41	727.0
17	1013.2	42	752.5
18	1064.3	43	966.0
19	930.0	44	485.0
20	1101.1	45	413.0
21	168.0	46	485.1
22	13.0	47	313.0
23	11.0	48	401.0
24	1061.3	49	396.0
25	892.0		

APPENDIX G. FALL EVAPORATION MEASUREMENTS

(26 September thru 24 October, 1989)

Station	106 mean	151 mean
Penman	2.5	3.4
Van Bavel	2.2	2.7
Penman-Monteith	2.3	2.8
Priestley-Taylor	2.5	3.1
Evap. (mm)	3.3	2.4
Net Rad. (MJ/m^2)	7.1	9.4
Temp. (^oC)	15.9	11.9
(e_s-e_a) (mb)	2.5	4.3
Wind (m/s)	2.0	2.3

Night Evaporation (midnight to 6am)

Station	106 hrly mean	151 hrly mean
Evap. (mm)	0.084	0.048
Net Rad (MJ/m^2)	-0.640	-0.702
Temp. (^oC)	13.2	9.5
(e_s-e_a) (mb)	2.7	3.8
Wind (m/s)	2.4	2.6

APPENDIX H. CALIBRATION OF GEM AIMOMETERS ON HALEAKALA

	Time	EE	GEM	Per	Click	Click /mm	Notes
151	890104 1600	Fill	0				
151	890105 700	10	1	N	1007	101	mist
151	890106 715	89	411	24	3854	43	rain
151	890107 720	28	0	24	2398	86	rain/wind
151	890107 1800	57	38	D	2424	43	WIND
151	890108 715	0	0	N	304	—	rain/wind
151	890108 1810	64	51	D	3176	50	WIND
151	890109 715	0	0	N	190	—	rain/wind
151	890109 1800	9	0	D	442	49	mist/wind
		257			13795	54	Q*=9.8 E=1.5
106	890104 1630	Fill	21				
106	890105 725	40	109	N	1615	40	
106	890106 735	103	41	24	4746	46	
106	890107 700	79	13	24	3509	44	
106	890108 730	110	91	24	5261	48	mist
106	890109 730	253	166	24	10153	40	drizzle
106	890109 1730	60	124	D	3323	55	
106	890110 700	30	4	N	1016	34	
		675			29623	44	Q*=6.7 E=3.8
119	890104 1700	Fill					
119	890105 750	41	62	N	1001	24	
119	890106 800	112	4	24	3894	35	1pm=0
119	890107 800	65	1	24	2375	37	3pm=1
119	890108 810	65	18	24	2243	35	1-4pm=0
119	890109 800	140	4	24	4327	31	12-3pm=0
119	890109 1635	55	254	D	2194	40	
119	890110 740	17	14	N	905	53	
		495			16939	34	Q*=7.2 E=2.7

LITERATURE CITED

Alty, T., 1935. The maximum rate of evaporation of water. Phil. Mag. J. Sci., 15,83-102.

Armesto, J.J. and J.A. Martinez, 1978. Relations between vegetation structure and slope aspect in the Mediterranean region of Chile. J. Ecol., 66,881-889.

Barry, R.G., 1981. Mountain Weather and Climate. Methuen, New York, 313 pp.

Bennett, O.L., E.L. Mathias, and G.A. Jung, 1976. Responses of perennial grasses and legumes to slope and microclimate. in . Hillands and J. Luchok (eds.), Proc. Int. Sympos., Morgantown, West Virginia, Oct 3-9, pp 476-491.

Bird, R.E. and C. Riordan, 1986. Simple solar spectral model for direct andn diffuse irradiance on horizontal and tilted planes at the Earth's surface for cloudless atmospheres. J. Climate Appl. Meteorol., 25,87-97.

Blaney, H.F., 1958. Evaporation from free water surfaces at high altitudes. Trans., Am. Soc. Civ. Eng., 123,385-404.

Bodhaine, B.A. and R.F. Pueschel. 1974. Source of seasonal variations in solar radiation at Mauna Loa. J. Appl. Meteor., 31,840-845.

Bowen, I.S., 1926. The ratio of heat losses by conduction and by evaporation from any water surface. Phys. Rev., 27,779-787.

Brown, L.H. and J. Cocheme, 1973. A study of the agroclimatology of the highlands of Eastern Africa. WMO Tech. Note 173, Geneva, Switzerland.

Brutsaert, W. 1975. A theory for local evaporation (or heat transfer) from rough an smooth surfaces at ground level. Water Resour. Res., 11,543-550.

Brutsaert, W. 1982. Evaporation into the Atmosphere. D. Reidel Pub. Co., 299 pp.

Brutsaert, W. 1986. Catchment-scale evaporation and the atmospheric boundary layer. Wat. Resour. Res., 23(9),39S-45S.

Brutsaert, W. and H. Stricker. 1979. An advection-aridity approach to estimate actual regional evapotranspiration. Water Resour. Res., 15,443-450.

Chamberlain, A.C., 1968. Transport of gases to and from grass and grass-like surfaces, Proc. Roy. Soc. London, A290,236-265.

Chang, Jen-hu, 1985. Evaporation in tropical highlands. IGU Working Group on Tropical Climate and Human Settlements, Proceedings.

Chang, Jen-hu, 1968. Climate and Agriculture, Aldine Publishing Co., Chicago.

Charnell, R.L., 1963. Longwave radiation near the Hawaiian Islands, J. Geophys. Res., 72(2),489-495.

Collie, C.H., 1982. Kinetic Theory and Entropy. Longman Group Ltd., Essex, UK.

Cottle, H.J., 1932. Vegetation on north and south slopes of mountains in southwestern Texas. Ecology, 12,105-155.

Dalton, J., 1802. Experimental essays on the consititution of mixed gases; on the force of steam or vapor from water and other liquids in different temperatures, both in a Torricellian vacuum and in air; on evaporation and on the expansion of gases by heat. Mem. Manchester Lit. Phil. Soc., 5,535-602.

de Bruin, H.A.R., 1983a. Evapotranspiration in humid tropical regions. in Hydrology of Humid Tropical Regions with Particular Refererce to the Hydrological Effects of Agriculture and Forestry Practice. Proc. Hamburg Sympos., August 1983, IAHS Publ. 140., pp. 299-311.

de Bruin, H.A.R., 1983b. A model for the Priestley-Taylor parameter a_g, J. Climate Appl. Meteor., 22,572-578.

Delaney, L.J., R.W. Houston and L.C. Eagleston, 1964. The rate of vaporization of water and ice. Chem. Eng. Sci, 19,105-114.

Doorenbos, J. and W.O. Pruitt, 1977. Crop Water Requirements, FAO Irr. Drain. Paper 24., Rome, 144 pp.

Ekern, P.C., 1965. The fraction of sunlight retained as net radiation in Hawaii. J. Geophys. Res., 70(4),785-793.

Ekern, P.C., 1982a. Variation in sunlight induced by topography under the trade wind regime on Oahu, Hawaii. Conference on Climate and Energy: Climatological Aspects and Industrial Operations, May 8-12, 1978, Asheville, NC,

Ekern, P.C., 1982b. Measured evaporation in high rainfall areas, leeward Koolau Range, Oahu, Hawaii. In Proc., Int. Sympos. on Hydrometeorology, ed. A.I. Johnson and R.A. Clark, Tech. Pub. Ser. TPS-82-1, Am. Water Resour. Assoc., Denver, Colorado, 85-89.

Ekern, P.C. 1983. Measured evaporation in high rainfall areas, leeward Koolau range, Oahu, Hawaii, U. Hawaii Wat. Resour. Res. Center Tech. Rpt. 156, Honolulu, Hawaii.

Ekern, P.C. and Jen-hu Chang. 1985. Pan evaporation: State of Hawaii, 1894-1983. State of Hawaii Dept. Land. Nat. Resour. Rep. R74., Honolulu, Hawaii, 172 pp.

Fick, A., 1855. Ueber Diffusion, Ann Phys. u. Chemie, 94(170),59-86.

Giambelluca, T.W., 1983. Water balance of the Pearl Harbor-Honolulu basin, 1946-1975. PhD disseration, Geography, U. Hawaii, Honolulu, Hawaii, 308 pp.

Giambelluca, T.W., M.A. Nullet, T.A. Schroeder, 1986. Rainfall Atlas of Hawaii, Dept. Land Natural Resour. Report R76., Honolulu, Hawaii. 267 pp.

Golding, D.L., 1978. Calculated snowpack evaporation during chinooks along the eastern slopes of the Rocky Mountains. J. Appl. Meteor., 17,1647-1651.

Grody, N.C., A.Gruber, and W.C. Shen, 1980. Atmospheric water content over the tropical Pacific derived from the Nimbus-6 scanning microwavespectrometer. J. Appl. Meteor., 19,986-996.

Han-Shun-Cheong, 1972. The measurement of global total radiation by wig-way integrators. Proceedings of the International Tropical Meteorology Meeting, Nairobi, Kenya, Vol. 1,259-266.

Horton, R.E., 1934. Water losses in high latitudes and at high elevations. Trans. Am. Geophys. Union, 15(2),351-379.

How, K.T.S., 1978. Solar radiation in Hawaii, 1932-1975. Dept. Land and Natural Resources Report R57, State of Hawaii, Honolulu, Hawaii.

Hoyt, D.V. and C. Frolich, 1983. Atmospheric transmission at Davos, Switzerland 1909-1979. Climatic Change, 5,61-71.

Iqbal, M., 1983. An Introduction to Solar Radiation. Academic Press. 390 pp.

Jones, C.A., 1980. A review of evapotranspiration studies in irrigated sugarcane in Hawaii. Hawaii. Plant. Rec., 59(9),195-214.

Kader, B.A. and A.M. Yaglom, 1972. Heat and mass transfer laws for fully turbulent wall flows. Int. J. Heat Mass Transfer, 15,2329-2351.

Keig, G., P.M. Fleming, and J.R. McAlpine, 1979. Evaporation in Papua New Guinea. J. Trop. Geog., 48,19-30.

Kondo, J., 1975. Air-sea bulk transfer coefficients in diabatic conditions, Boundary-Layer Meteor., 9,91-112.

Kustas, W.P. and W. Brutsaert, 1987. Budgets of water vapor in the unstable boundary layer over rugged terrain. J. Climate Appl. Meteor., 26,607-620.

Lavoie, R.L., 1972. A numerical model of trade wind weather on Oahu. Mon. Weather Rev., 102,630-637.

LeDrew, E.F., 1975. The energy balance of a mid-latitude alpine site during the growing season, 1973. Arct. Alp. Res., 7(4),301-314.

Legowo, E., 1986. Estimation of water extractability and hydraulic conductivity in tropical mollisols, ultisols, and andisols. PhD Dissertation, Agronomy and Soil Science, University of Hawaii, Honolulu, Hawaii.

Leopold, L., 1949. The interaction of trade wind and sea breeze, Hawaii. J. Meteorol., 6,312-320.

List, R.J., 1966. Smithsonian Meteorological Tables. Smithsonian Institution Press, Washington D.C., 527 pp.

Livingston, G.J., 1909. An annotated bibliography on evaporation, Mon. Weather Rev., 36,181-186.; 301-306; 375-381.

Longacre, L.L. and H.F. Blaney, 1962. Evaporation at high elevations in California. Am. Soc. Civ. Eng., J. Irrig. Drain. Div., 3172,33-54.

Lyons, S., 1979. Summer weather on Haleakala, Maui. U. Hawaii Meteor. Dept. Tech. Rpt. 79-09, Honolulu, Hawaii.

Martin, M. and P. Berdahl, 1984. Summary of results from the spectral and angular sky radiation measurement program. Solar Energy, 33,241-252.

Mendonca, B.G., K.J. Hanson, and J.J. DeLuise, 1978. Volcanically related secular trends in atmospheric transmission at Mauna Loa Observatory, Hawaii. Science, 202,513-515.

Mendonca, B.G. and W.T. Iwaoka, 1969. The trade wind inversion at the slopes of Mauna Loa, Hawaii, J. Appl. Meteorol., 8,213-219.

Merlivat, L., 1978. The dependence of bulk evaporation coefficients on air-water interfacial conditions as determined by the isotopic method. J. Geophys. Res., (Oceans & Atmos.) 83(C6),2977-2980.

Moller, F., 1951. Long-wave radiation. in: Compendium of Meteorology, American Meteoroligcal Society, Waverly Press, Inc., Baltimore, Maryland, pp 34-49.

Monin, A.S. and A.M. Obukhov, 1954. Basic laws of turbulent mixing in the ground layer of the atmosphere. Tr Geofiz. Instit. Akad. Nauk, USSR, 24(151),163-187 (German translation (1958), Sammelband zur Statistischen Theorie der Turbulenz, H. Goering (ed), Akademie Verlag, Berlin,) 228 pp.

Monteith, J.L., 1965. Evaporation and environment. in G.E. Fogg (ed.) The State and Movement of Water in Living Organisms, Sympos. Soc. Exper. Biol., Academic Press, 19,205-234.

Monteith, J.L., 1981. Evaporation and surface temperature. Quart. J. Royal Meteor. Soc., 107(451),1-27.

Monteith, J.L., 1985. Evaporation from land surfaces: Progress in analysis and prediction since 1948. Advances in Evapotranspiration, Am Soc. Agric. Eng. Pub. 14-85, pp. 4-12.

Morton, F.I., 1975. Estimating evaporation and transpiration from climatological observations. J. Appl. Meteorol., 14,488-497.

Noguchi, Y., 1979. Deformation of trees in Hawaii and its relation to wind. J. Ecology, 67,611-628.

Nullet, D., 1987. Sources of energy for evaporation on tropical islands. Phys. Geog., 8(1),36-45.

Nullet, D., 1988. A comparison of two methods of estimating insolation over the tropical Pacific ocean using cloudiness from satellite observations. Solar Energy, 39,197-201.

Nullet, D. and P.C. Ekern, 1988a. Modeling clear day insolation in the Hawaii. Solar Energy, 40,187-189.

Nullet, D. and P.C. Ekern, 1988b. Temperature and insolation trends in Hawaii. Theor. Appl. Climatol., 39,90-92.

Oke, T.R., 1978. Boundary Layer Climates. Methuen & Co. Ltd., London, Great Britain,372 pp.

Paltridge, G.W. and C.M.R. Platt, 1976. Radiative Processes in Meteorology and Climatology. Elsevier Scientific Publishing Company, Amsterday, Netherlands, 318 pp.

Panofsky, H.A. and J.A. Dutton, 1984. Atmospheric Turbulence. John Wiley and Sons, 397 pp.

Paulson, C.A., 1970. The mathematical representation of wind speed and temperature profiles in the unstable atmospheric surface layer. J. Appl. Meteor., 9,857-861.

Peck, E.L. and D.J. Pfankuch, 1963. Evaporation rates in mountainous terrain. Intl. Ass. Sci. Hydrol., Gentbrugge, Belgium, Publ. #62, pp. 267-278.

Penman, H.L., 1948. Natural evaporation from open water, bare soil, and grass. Proc. Roy. Soc. London, A193,120-146.

Penman, H.L. and R.K. Schofield, 1951. Some physical aspects of assimilation and transpiration. Sympos. Soc. Exper. Biol., 5,115-129.

Perry, A.E. and P.N. Joubert, 1963. Rough-wall boundary layers in adverse pressure gradients, J. Fluid Mech., 17,193-211.

Plate, E.J., 1971. Aerodynamic characteristics of atmospheric boundary layers. AEC Critical Review Series, US Atomic Energy Comm., Div. Tech. Info., 190 pp.

Priestley, C.H.B. and R.J. Taylor, 1972. On the assessment of surface heat flux and evaporation using large-scale parameters. Mon. Weather Rev., 100,81-92.

Prohaska, F., 1970. Distinctive bioclimatic parameters of the subtropical-tropical Andes. Int. J. Biomet., 14,1-12.

Pueschel, R.F., L. Machta, G.F. Cotton, E.C. Flowers, and J.T., 1972. Peterson. Normal incidence radiation trends on Mauna Loa, Hawaii. Nature, 240,545-547.

Ripley, E.A., 1976. Comments on "Gamma--the phychrometer non-constant." J. Appl. Meteor., 15,1027-1028.

Rohwer, C., 1931. Evaporation from free water surfaces. US Dept. of Agriculture Tech. Bull. 271., Washington D.C.

Rouse, W.R., 1970. Relations between radiant energy supply and evapotranspiration from sloping terrain: An example. Can. Geog., 14(1),27-37.

Rouse, W.R. and R.G. Wilson. 1969. Time and space variations in the radiant energy fluxes over sloping forested terrain and their influence on seasonal heat and water balances at a middle latitude site. Geografiska Annaler, 51A(3),160-175.

Scarf, F., 1976. Evaporation in Peninsular Malaysia, Bahagian Parit dan Taliair Kementerian Pertanian, Wat. Resour. Pub. 5, 14 pp.

Schetz, J.A., 1984. Foundations of Boundary Layer Theory for Momentum, Heat, and Mass Transfer. Prentice-Hall, Inc., Englewood Cliffs, New Jersey.

Schroeder, T.A., 1980. Project Ahupua'a: Solar meteorological field measurements on the island of Hawaii, summer 1978--3. Trade wind interactions with local winds in south Kohala. University of Hawaii Department of Meteorology Report UHMET 79-05, Honolulu, Hawaii.

Schulze, R.E., 1975. Mapping potential evapotranspiration in hilly terrain. S. Afr. Geog. J., 57(1),26-35.

Segal, M., Y. Mahrer, R.A. Pielke, and Y. Ookouchi, 1985. Modeling transpiration patterns of vegetation along south and north facing slopes during the subtropical dry season. Agric. and Forest Meteor., 36(1),19-28.

Singh, B. and R. Taillefer, 1986. The effect of synoptic-scale advection on the performance of the Priestley-Taylor evaporation formula. Bound. Layer Meteorol., 36,267-282.

Slatyer, R.O. and I.C. McIlroy, 1967. Practical Microclimatology, CSIRO, Melbourne, Australia, 310 pp.

Storr, D. and G. den Hartog, 1975. Gamma--the psychrometer non-constant. J. Appl. Meteor., 14,1397-1398.

Sutton, O.G., 1955. Atmospheric Turbulence, Methuen & Co., 111 pp.

Symons, G.J., 1867. Evaporators and evaporation, British Rainfall. (from Monteith, 1981).

Szymber, R.J. and W.D. Sellers, 1985. Atmospheric turbidity at Tucson, Arizona, 1956-83: Variations and their causes. J. Appl. Meteorol., 24,725-734.

Thom, A.S., 1972. Momentum, mass and heat exchange of vegetation. Quart. J. Roy. Meteorol. Soc., 98,124-134.

Thom, A.S. and H.R. Oliver, 1977. On Penman's equation for estimating regional evaporation. Quart. J. Roy. Meteor. Soc., 103,345-357.

Van Bavel, C.H.M., 1966. Potential evaporation: the combination concept and its experimental verification, Water Resour. Res., 2,455-467.

Yoshihara, T. and P.C. Ekern, 1978. Assessment of the potential of solar energy in Hawaii. HNEI, University of Hawaii, 49 pp and 5 Appendicies.